ELECTRICAL MEASUREMENTS OF CAPACITIVELY COUPLED PULSED POWER PLASMAS

by

Alex F. Press

APPROVED BY SUPERVISORY COMMITTEE:

Lawrence J. Overzet, Co-Chair

Matthew J. Goeckner, Co-Chair

Roderick A. Heelis

Rashaunda M. Henderson

Randall E. Lehmann

To Kristin; my fiancée, the love of my life, best friend, greatest cheerleader, steadfast companion, and daily inspiration. I am very fortunate and grateful to have found you.

ELECTRICAL MEASUREMENTS OF CAPACITIVELY COUPLED PULSED POWER PLASMAS

by

ALEX F. PRESS, BS, MSEE

DISSERTATION
Presented to the Faculty of
The University of Texas at Dallas
in Partial Fulfillment
of the Requirements
for the Degree of

DOCTOR OF PHILOSOPHY IN
ELECTRICAL ENGINEERING

THE UNIVERSITY OF TEXAS AT DALLAS
May 2020

ACKNOWLEDGMENTS

It takes a village to raise a child. It takes the same amount of people to finish a dissertation. I would like to thank some of the people who have supported me on this journey. Thank you to my advisors Dr. Lawrence J. Overzet and Dr. Mathew J. Goeckner for their mentorship. Thank you to my dissertation committee members Dr. Roderick A. Heelis, Dr. Rashaunda M. Henderson and Dr. Randall E. Lehmann for their time and advice. Thank you to my undergraduate research professor Dr. David N. Ruzic who encouraged me to pursue graduate school. Thank you to my lab mates, especially Keith Hernandez who I have worked closely with, and has been through the crucible with me. Thank you to my friends who have provided fun and necessary distractions. Thank you to my family who has given me an endless supply of encouragement. Finally thank you to my fiancée Kristin whose daily support formed the shoulder I needed to stand on.

December 2019

ELECTRICAL MEASUREMENTS OF CAPACITIVELY COUPLED PULSED POWER PLASMAS

Alex F. Press, PhD
The University of Texas at Dallas, 2020

Supervising Professors: Lawrence J. Overzet, Co-Chair
Matthew J. Goeckner, Co-Chair

Pulsing the power to radio frequency (rf) driven plasmas creates transition periods which exhibit plasma conditions not reachable in continuous wave plasmas. One advantageous effect, is etch feature charge neutralization in integrated circuit manufacturing. Charge neutralization is usually attributed to low energy positive and negative ions interacting with the etch surface during the pulse afterglow; however, the sheath electric fields can be momentarily reversed under some pulsed conditions and accelerate electrons to the surface rather than repel them. This can allow electrons to perform at least some of the positive charge neutralization needed at the surface. Electrons engaging in surface charge neutralization can negate the need for relatively long power off times which allow negative ions to neutralize the surface. Although pulsed power plasmas have processing benefits, there are still engineering challenges which need to be addressed. A major challenge is ultra-fast impedance matching as the plasma impedance varies over a pulse cycle. One method to reduce the unmatched period is to quickly adjust the rf driving (fundamental) frequency; however, a similar reduction in the mismatch period can be achieved more simply by increasing the rf amplifier output power at the beginning of the pulse. This allows the electric fields interacting with the plasma, and therefore the plasma impedance, to reach their steady state values more quickly. Thus, the unmatched period can be reduced through a change in power magnitude rather than frequency. Electrical measurements of the plasma can be used to show evidence for both sheath reversal and decreased unmatched period. This requires high time resolution, which is obtained though performing an FFT on a short sampling period of measured electrode rf current and voltage (RFIV). Further, detailed corrections to the RFIV measurements must be made to account for parasitic impedances and propagation delay in the chamber-electrode circuits which include propagation direction of the fundamental frequency and its harmonics. Lastly, Langmuir probes are an often used plasma diagnostic tool as they can measure both the plasma density as well as the electron temperature or energy distribution function. Unfortunately, the fast fluctuations in the plasma potential which occur at plasma re-ignition can induce significant errors in calculated plasma parameters and even produce IV curves which are unphysical. Diagnosing plasmas with quickly varying plasma potentials requires an understanding of these Langmuir probe-plasma interactions. This dissertation provides four contributions to plasma science; a method to accurately measure time resolved plasma RFIVs, a novel method for impedance mismatch reduction in a pulse cycle, evidence for sheath reversal which allows an anisotropic electron distribution to interact with surfaces, and demonstration of measurement issues when using Langmuir probes in pulsed power plasmas.

TABLE OF CONTENTS

CURRICULUM VITAE

LIST OF FIGURES

LIST OF TABLES

CHAPTER 1

INTRODUCTION TO PULSED PLASMAS

The study of pulsed plasmas focuses on the transient behavior of plasma, as power deposition is changed. This is in contrast to the vast majority of plasma knowledge which has focused on steady state behavior. Although it is less studied, pulsed plasma has found interest and application in a wide variety of places. A major area of interest is integrated circuit (IC) fabrication. In IC fabrication etch processes (material removal), pulsed plasmas processing has advantages such as reduced plasma induced damage, improved uniformity and improved material selectivity (Banna et al., 2012; Lee et al., 2014; Economou, 2014). Outside of IC fabrication, there are many other pulsed plasma applications which range from medical applications (Kumar et al., 2016) and waste remediation (Jiang et al., 2014), to plasma thrusters (Polzin, 2011) and fusion experiments (Li et al., 2013). With such a wide variety of plasmas being referred to as pulsed, it is important to define what pulsed plasma means in the context of this dissertation.

In radio frequency (rf) plasmas, the driving electrical signal is a sine wave with a frequency on the order of 1 to 100 MHz. Depending on the plasma being examined, it is common to consider either the applied voltage or applied current to be the parameter critical to maintaining the plasma. In any case, for an rf plasma, setting the voltage or current will set the other and the power. Pulsed plasma is then achieved by modulating the amplitude of these parameters. The most straight forward way of doing this is to modulate the current (or voltage or power) amplitude with a square wave, giving a current on time and off time. This is shown in Figure 1.1 for 10 kHz, 100 kHz and 1 MHz pulse frequency.

When varying the pulsed plasma amplitude modulation (AM) frequency in rf plasmas, there are three discrete regimes. In the first, the AM frequency is on the order of the driving frequency. In this case, the AM frequency is so high, that the modulated waveform looks more like a change to the driving waveform, and less like a pulse. The second regime is when

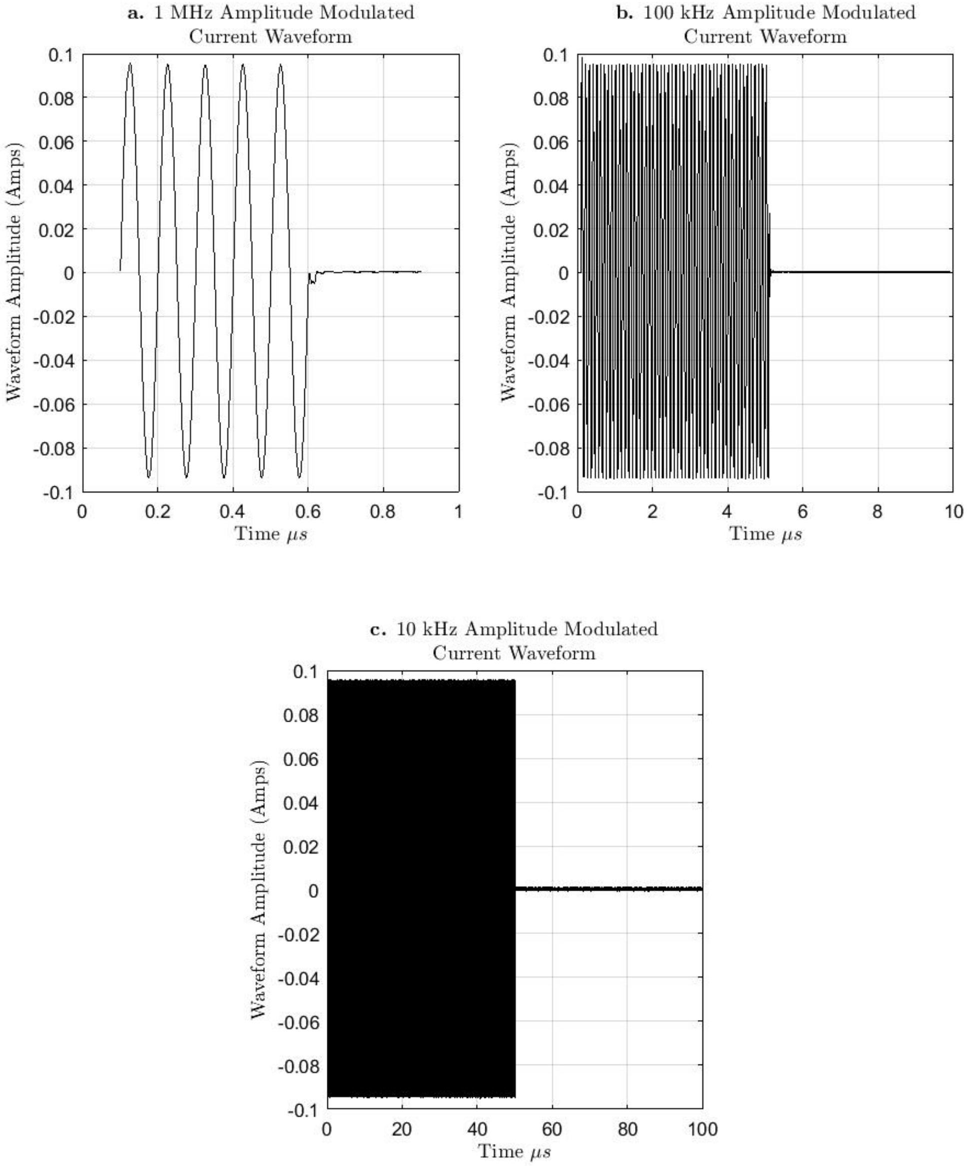

Figure 1.1. Part a. Very high frequency AM pulse, only a few rf cycles per pulse period. Part b. High frequency AM pulse, 10's of rf cycles per pulse. Part c. Average (often used in literature) frequency AM pulse, 100's of rf cycles per pulse.

the AM frequency is very low, and the plasma parameters decay in the pulse off time to their values found in a standard gas. This is more consistent with turning the plasma off and on, rather than pulsing. A plasma that is ignited in a reactor for a few minutes one day and then reignited the next day is not called a pulsed plasma. However, one which is allowed to decay fully but reignited quickly on a human time scale (human eye time resolution is between 15 and 60 Hz) is sometimes called pulsed operation. From the plasma perspective, turning the plasma on after a 24 hour off time, is the same as turning it on after a 10 millisecond off time if all of the species, including radicals, created in the plasma decay in that time. Finally the frequencies in-between the first and second regimes, where the AM frequency is lower than the driving frequency, but high enough that the plasma parameters are not decaying to their gas values, is clearly plasma pulsing and is the focus of this dissertation. In the next section, plasma parameter dynamics over a pulse cycle are described.

1.1 Pulsed Plasma Parameters

In previous research on pulsed plasmas, generally a square wave with 100% depth (full on and off pulsing) was used. The pulse parameters that were varied were the pulse frequency, and duty cycle. Since this is the norm, the effects of this sort of pulsing have been reported on, and will be overviewed in this section. Which of the plasma parameters are important depends greatly on the application. Those presented here are often important for applications or plasma understanding. They are; electron temperature (T_e), plasma density (n), negative ion density (n_{i^-}), DC bias voltage, and plasma potential (V_p). The following subsections demonstrate some of the effects pulsing has on these parameters.

1.1.1 Electron Temperature

In their 1995 article (Ashida et al., 1995), Ashida and Lieberman gave the results of a 0 dimensional (0D), or global model of a pulsed argon plasma. The model showed that in some cases when the power was applied, T_e overshot its steady state value before returning to it. In other cases, it rose steadily to its steady state value. This has been measured experimentally in many investigations (Mishra et al., 2012; Boffard et al., 2015; Xue et al., 2017). The difference between T_e overshooting or not, was the length of the power off time. If the off time was long enough, n_e drops very low and when the power is applied, there aren't enough electrons to screen the electric fields from the gas bulk. Therefore, all of the free electrons are accelerated by the maximum electric field, which gets converted into temperature through collisions. If the off time is short, when the power is reapplied there are enough electrons to screen the electric field, and the power couples in a similar manner as it does in the steady state. However T_e spikes have been reported in plasmas where the density did not have time to decrease drastically during the off period. Chapter 4 will demonstrate how Langmuir probe measurements can falsely show T_e spikes in power transition regions.

1.1.2 Plasma Density - Electropositive System

The plasma bulk is approximately neutral, therefore in electropositive systems, electron density, and ion density are approximately equal to each other and can be represented by a single value (n). n increases when the power turns on and decreases when the power turns off. The increase is governed by the electron temperature and electron-neutral collision frequency. The decrease is governed by gas phase and surface recombination, which depends on pressure and diffusion. For surface recombination, the characteristic chamber length (typically the smallest lengths between chamber features, i.e. electrode gap) set the distance a particle must diffuse to reach a surface and recombine. The assumption that electron and ion density are approximately equal is not always valid. For example, in regions with large time averaged electric fields such as the sheath, the time average electron density is far smaller than the ion density. Because of the large electric fields, it is generally these regions where power is absorbed by the plasma.

1.1.3 Plasma Density - Electronegative System

Plasma densities operate a bit differently in electronegative discharges, where some plasmas can have large populations of negative ions. Like positive ions, the negative ion density is determined by a balance between the generation and loss rates. Generally negative ions are kept in the center of the plasma by the presheath electric field and cannot neutralize at the wall. However when the power is turned off, the sheath collapses, allowing the electrons to escape quickly. If the off time is long enough an ion-ion plasma can form, and the negative ions are able to reach surfaces (possibly aided with bias voltages) (Kanakasabapathy et al., 2001).

1.1.4 Radical Density

The neutral radical density (n_{rad}), like ion density, depends on the generation rate equation. However the loss rate mechanisms can be fundamentally different than for ions. Like ions, recombination in the bulk depends on densities and temperatures, however contacting a surface does not guarantee recombination. As well, loss can come from surfaces which adsorb the radical, or from combination or dissociation into different particles. Generally the radical density takes longer to decay than the other plasma parameters, and so do not change dramatically in pulse cycles that are short relative to the decay time. However, n_{rad} generation is a function of electron temperature and density and therefore is a function of the average power over a period.

1.1.5 Plasma Sheaths and DC Bias

When plasmas interact with a surface, a potential difference between the surface and V_p forms. The resulting electric field is referred to as the sheath. This sheath forms due to the mass difference between negative charge carriers (electrons) and positive charge carriers (positive ions). An argon ion is ≈73,000 times more massive than an electron. The result is that electrons have a higher mobility, and flow out of the plasma to surfaces in much greater number causing a negative charge build up at the surface, and a positively charged plasma bulk. The nature of the sheath will depend on the surface conditions; DC or rf powered, grounded or floating.

To understand each sheath type, the negative (electron) flux and positive (ion) flux to a surface must be understood. For a planar surface in contact with a plasma, the ion flux and electron flux are governed by four equations, ion flux to an attracting or repelling surface, and electron flux to an attracting or repelling surface. In this chapter all surfaces will be assumed to be planar, therefore changing sheath width does not affect the flux to a surface. This allows zero potential and attracting surfaces to be treated the same. For non-planer surfaces, expanding and contracting sheaths will cause the area of the plasma bulk-sheath interface to increase or decrease, causing the flux to a surface to vary. To simplify the equations, a Maxwell-Boltzmann energy distribution is assumed for both ions and electrons in the plasma bulk, allowing their temperatures (T_i and T_e) to be defined in the usual way. This distribution will also hold for each charge type when the sheath electric field repels them from a surface. However, when the sheath attracts them to a surface, their distribution will become directional, with their velocities normal to the surface increasing. For example, when the surface potential is negative with respect to V_p, electrons will be repelled and maintain a Maxwell-Boltzmann energy distribution in the sheath, while ions will be attracted, and reach the surface with an anisotropic velocity distribution. First, the ion flux to an attracting surface or ion saturation flux Γ_{is} is given by

$$\Gamma_i = \Gamma_{is} \approx n_{ib} u_b \qquad (V_{surface} \leq V_p), \tag{1.1}$$

where n_{ib} is the ion density at the sheath edge, u_b is the average ion velocity at, and normal to, the plasma bulk (or presheath)-sheath interface, and is known as the Bohm velocity. The Bohm velocity is given by

$$u_b = \sqrt{\frac{k_B T_e}{M_i}}, \tag{1.2}$$

where k_B is the Boltzmann constant, and M_i is the ion mass. Second, when the surface potential repels positive ions, only ions with enough thermal energy to overcome the potential barrier reach the surface. The ion flux is then given by

$$\Gamma_i = \frac{1}{4} n_{ib} v_i e^{\left(\frac{V_{surface}-V_p}{k_B T_i}\right)} \qquad (V_{surface} > V_p), \tag{1.3}$$

where v_i is the mean ion speed for a Maxwell-Boltzmann distribution, given by

$$v_i = \sqrt{\frac{8 k_B T_i}{\pi m_i}}, \tag{1.4}$$

where T_i and m_i are the ion temperature and mass. This equation is valid only when $T_i \approx T_e$ which is not the case in the plasmas presented in this dissertation. In non-equilibrium plasmas, Γ_i will have a dependence on T_e as shown by Bohm et al. (Bohm et al., 1949). However, in these plasmas T_i is small ≈0.026 eV, and $\Gamma_i \approx 0$ for repelling surfaces. Third, the electron flux to an attracting surface or electron saturation flux is given by

$$\Gamma_e = \Gamma_{es} = \frac{1}{4} n_{eb} v_e \qquad (V_{surface} \geq V_p), \tag{1.5}$$

where n_{eb} is the electron density at the sheath edge, and v_e is the mean electron speed for a Maxwell-Boltzmann distribution, given by

$$v_e = \sqrt{\frac{8 k_B T_e}{\pi m_e}}, \tag{1.6}$$

where m_e is the electron mass. Finally, the electron flux to repelling surfaces, is given by

$$\Gamma_e = \Gamma_{es} e^{\left(\frac{V_{surface}-V_p}{k_B T_e}\right)} \qquad (V_{surface} < V_p). \tag{1.7}$$

The total charge flux is then given by

$$\Gamma_q = q\Gamma_i - q\Gamma_e, \tag{1.8}$$

where q is the elementary charge. The current to a surface is given by

$$I = \Gamma_q A, \tag{1.9}$$

where A is the surface area. In an Argon plasma the ratio of Γ_{es} to Γ_{is} is $\approx$215. Therefore, to a surface with potential equal to V_p, total charge flux, and therefore current, will be electron dominated. At the start of a pulse period the electrons reach surfaces in greater numbers than positive ions. If the surface is not DC grounded (the powered electrode has a blocking capacitor in the match network terminating the DC current path), than a DC bias voltage will build up. This voltage repels electrons reducing electron flux to the surface. The DC bias voltage will build up until $\Gamma_i = \Gamma_e$ denoting that steady state has been reached. In rf discharges, the DC bias voltage does not rise as high as the rf voltage amplitude, however the difference is made up by V_p, which results in sheath voltages which always repel (during every part of the rf cycle) electrons from a surface, allowing $\Gamma_i = \Gamma_e$.

In the preceding discussion, only one surface interacting with the plasma has been treated. To do this, the plasma has been assumed to be infinitely large, and thus able to supply any current without changing V_p. In real laboratory systems, the DC bias build up will depend on the ratio of powered to grounded surface area. When the two are equal, the voltage across each sheath will be equal and 180° out of phase. In this case the electron flux is the same to both surfaces, and no DC bias is built up. As one surface becomes smaller than the other (generally the powered surface is smaller), the sheath voltage magnitude at the smaller surface becomes larger. This reduces the minimum electron repelling sheath voltage compared to that of the other surface, or allows an electron attracting sheath to form for part of an rf cycle. In either case, the electron flux to the smaller surface becomes larger. The blocking capacitance blocks the current and charge builds up until the resulting voltage is large enough to repel enough electrons from the smaller surface, to bring $\Gamma_e = \Gamma_i$. The magnitude of the DC bias is then dependent not only on the rf voltage magnitude, but also the ratio of powered and grounded surface areas (Köhler et al., 1985).

1.1.6 Plasma Potential

When the plasma is first turned on, net electron flux to surfaces causes V_p to become positive. V_p then acts as an electron repelling voltage to all surfaces. In some conditions the DC bias does not build up as quickly as the rf voltage at the beginning of a power pulse. In these cases, the increased electron current can cause V_p to overshoot its steady state value until the DC bias grows large enough that $\Gamma_i > \Gamma_e$, causing V_p to fall to its steady state. If the dynamics of the DC bias and plasma potential are known, then the sheath voltage can be found as $V_{sheath} = V_{DC} + V_p$. The sheath voltage is often important in plasma processing as it is a major factor determining the energy at which ions bombard the surface, affecting both etching and deposition.

1.2 Dissertation Organization

This dissertation is organized into three parts. In Chapter 2, a method to measure the current through the plasma and voltage across the plasma is presented. Chapter 3 will use the current and voltage measurements to understand how to control their build up at the start of a pulse cycle. Some of the possible advantages gained from controlling their build up will be discussed. Finally, Chapter 4 will present Langmuir Probe measurement errors induced in transient plasmas due to changing V_p.

CHAPTER 2

TIME RESOLVED RADIO FREQUENCY CURRENT AND VOLTAGE (RFIV) MEASUREMENT SYSTEM FOR USE IN TRANSIENT PLASMAS[1]

2.1 RFIV Abstract

Transient plasmas (such as pulsed power plasmas) can be of interest to both industry, where they allow for new processing windows, and basic science where their dynamics are of interest. However, their study requires time resolved diagnostic techniques. One powerful diagnostic is current and voltage (IV) measurements, which along with the power and impedance calculated from them, can be used to characterize a plasma. This is especially true as it is an outside the chamber, non-invasive technique, and can be used in systems where a probe, or fiber optic bundle/window will affect processing results or fail due to deposition. To obtain accurate IV values, frequency dependent probe calibrations must be performed, frequency dependent parasitic impedances in the system and propagation delay between the forward traveling fundamental frequency and backwards traveling harmonic frequencies must be taken into account. To separate the fundamental and harmonic frequencies, a Fast Fourier Transform (FFT) is traditionally performed in continuous wave plasmas. In transient plasmas, a time resolved FFT is necessary. This chapter presents a method to perform each of these steps while demonstrating their importance, and giving some measurements of a pulsed power, 75 mTorr, capacitively coupled argon plasma.

---

[1] The contents of this chapter were previously published (Press et al., 2019), with the exception of Subsection 2.4.2 which is included in this dissertation only. The work presented is my own. Reproduced from Press, Alex F., Matthew J. Goeckner, and Lawrence J. Overzet. "Sub-rf period electrical characterization of a pulsed capacitively coupled argon plasma." Journal of Vacuum Science & Technology B, Nanotechnology and Microelectronics: Materials, Processing, Measurement, and Phenomena 37, no. 6 (2019): 062926., with the permission of AIP Publishing.

2.2 Introduction

Radio frequency current and voltage (RFIV) measurements are often used to characterize continuous wave plasma systems. In rf driven plasmas, the phase as well as the magnitude of a waveform is measured. These measurements can then be used to find the active and reactive power in the system, as well as the impedance of the plasma. To confirm that power measured in this way is accurate, Godyak and Piejak compared several methods and found them to be in agreement (Godyak and Piejak, 1990). These power measurements, when converted to power flux or density, or when used in similar tools, can be used to compare plasma processing conditions. Impedance measurements of the plasma can be used as a diagnostic for plasma parameters and sheath conditions through the use of equivalent circuit models (Koenig and Maissel, 1970; Keller and Pennebaker, 1979; Bletzinger and Flemming, 1987; Butterbaugh et al., 1990; Beneking, 1990; Godyak et al., 1991; Overzet and Leong-Rousey, 1995; Miranda and Spanos, 1996; Overzet et al., 2010). These methods generally focus on the fundamental frequency, however harmonic frequencies can be included to resolve the waveform shape. The voltage waveforms are an important parameter when calculating ion energy distribution functions (Panagopoulos and Economou, 1999; Donkó et al., 2012; Schuengel et al., 2013), studying heating modes (Schulze et al., 2009; Donkó et al., 2012; Bruneau et al., 2015; Brandt et al., 2016), or separating measured sheath current into conduction and displacement components (Sobolewski, 1995).

While these techniques are used in continuous wave (cw) plasmas, there is a desire to make use of them in time modulated, transient discharges. In power modulated plasmas, diagnostics with sub microsecond time resolution are required (see (Banna et al., 2012), for an overview of inductively coupled pulsed power plasmas). This can be achieved for current and voltage (IV) measurements using an FFT method with time resolution of one rf period described by Overzet and Leong-Rousey (Overzet and Leong-Rousey, 1995), and Poulose et al. (Poulose et al., 2017). However for accurate results, the IV probes must be calibrated, chamber parasitic impedances must be taken into account, and frequency dependent signal propagation direction and delay must be taken into account.

In this chapter, the ability of the time resolved FFT to represent the measured data is demonstrated (Section 2.4). Next, the probe calibration procedure is given, followed by an outline of a method to find chamber parasitic impedance values, which are used to correct for the effects of the impedances (Section 2.4.1). Subsection 2.4.3 shows the effects of taking signal propagation delay into account on waveform magnitude and shape. The corrected waveforms can then be separated into sheath voltages, as well as sheath conduction and displacement currents (Sections 2.5, and 2.6). Section 2.7 will discuss the overall results of this method performed on a power pulsed Argon plasma, as well as some of the features shown in the measured waveforms.

2.3 Experimental Setup

Figure 2.1 is a sketch of the plasma chamber, including the location of the powered electrode IV probes, the grounded electrode current probe, and the DC bias measurement circuit connection point. A transmission line connects the grounded electrode to the grounded electrode current probe. The signal path is shorted to the grounded chamber wall immediately after passing through the grounded electrode probe. The voltage probe is capacitively coupled to the powered electrode line, which is fed into the 50 Ω input of a Tektronix DPO 7254 oscilloscope. The current probes (Pearson Electronics 2877) are fed into 1 MΩ-13.5 pF inputs of the same oscilloscope. All probes are placed as close to the electrodes as is physically possible to reduce the amount of parasitic impedance. A DC bias measurement circuit is placed just after the matching network, before the rf probes. This allows the DC bias to be measured, while its placement before the rf measurement point means the circuit is not included in parasitic impedance calculations. The DC bias measurement circuit consists of a grounded 65 pF capacitor, in series with an Ohmite Z7 84 μH choke. The voltage is measured by a

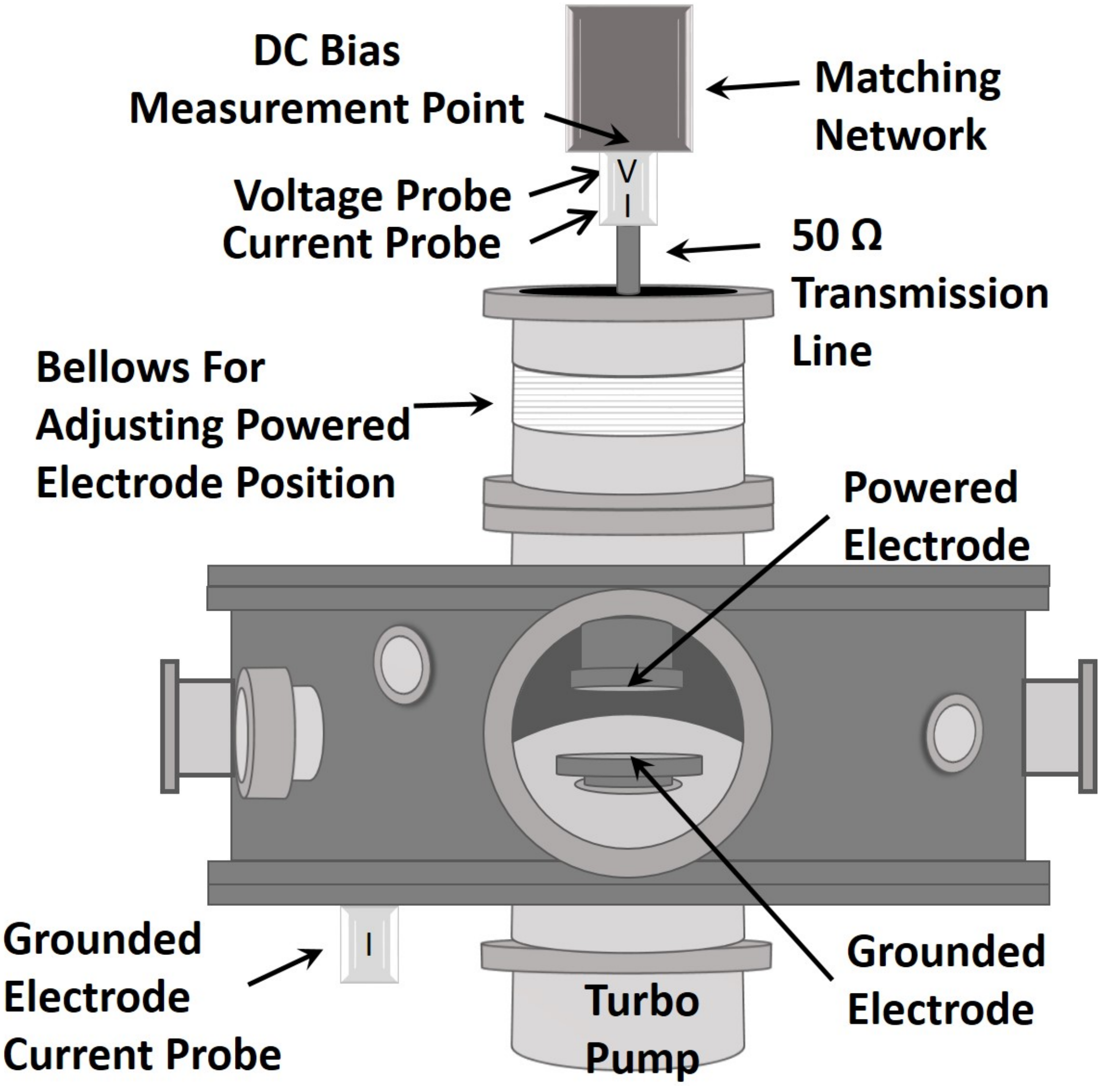

Figure 2.1. mGEC physical chamber setup showing RFIV measurement probes, and electrode positions (not to scale).

Hantek T3100 probe connected to a 1 MΩ-13.5 pF input of the oscilloscope. The DC bias voltage is measured across the capacitor.

The chamber is the modified Gaseous Electronics Conference chamber described by Goeckner et al. (Goeckner et al., 2004). The powered electrode consists of an aluminum electrode face (11.4 cm diameter) in contact with the plasma, with a copper water cooled heat sink on the back. A low impedance 61 cm RG-8 50 Ω transmission line connects the powered electrode to the IV probe box. The probe box is connected to the matching network power output. The powered electrode's vertical location is adjustable, allowing the gap between it and the grounded electrode to be set anywhere between 2 cm and 12.5 cm. For the measurements reported, the gap was set to 6.35 cm. The grounded electrode has a 15 cm diameter. Both electrodes are surrounded by grounded electrode shields. The gap between electrode and ground shield is empty (no dielectric), and ≈2.5 mm thick. The transmission lines and electrode-ground shield configuration make up the chamber electrical circuit, and will set the values of the parasitic impedances. For pulsed power plasma operation, the gas pressure was set to 75 mTorr, the gas flow was 50 SCCM of argon, and the power was pulsed on and off with a 50% duty cycle at 10 kHz. The rf driving frequency was set to 13.33 MHz, resulting in a ≈75 ns rf period.

2.4 Signal Processing and Calibration

The probe calibration and plasma impedance corrections are frequency dependent, therefore an FFT is performed on the collected IV data. To achieve one rf period time resolution, the waveform is chopped into one rf period sections (≈375 sample points at the driving frequency 13.33 MHz with 5 GS per second oscilloscope resolution) before the FFT is performed (Overzet and Leong-Rousey, 1995; Poulose et al., 2017). For the FFT to function well, the points per an rf cycle should be a power of two. Therefore linear interpolation is performed on the chopped waveform sections so that the points per section equal the first

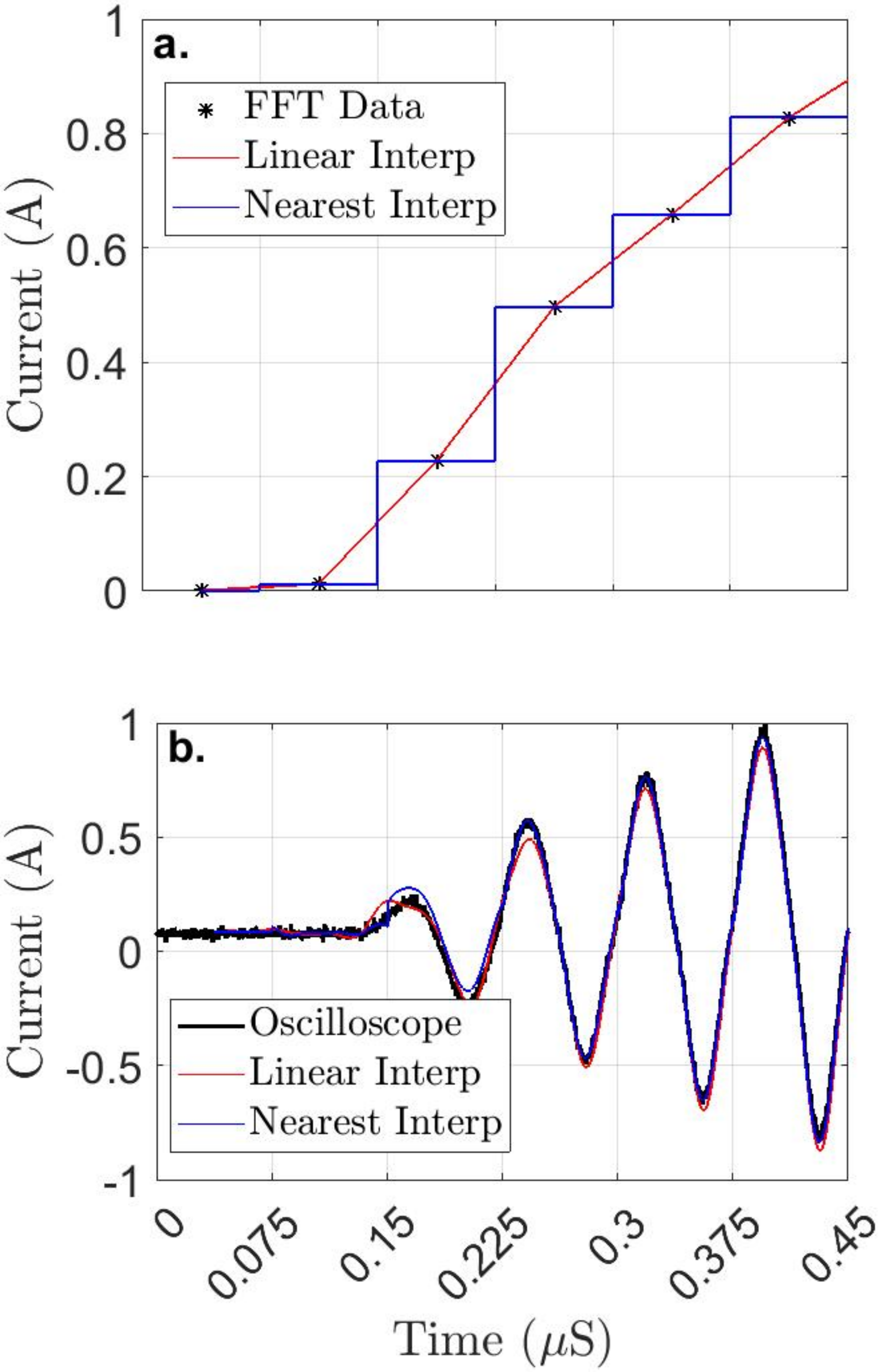

Figure 2.2. FFT calculated current magnitude and rebuilt waveforms during the rf power turn on, with linear and nearest interpolation methods. The interpolation is set to return values at the sampling frequency set on the oscilloscope.

power of two greater than the number of input points (512). The FFT is then performed, giving one magnitude and phase value for each chopped section at the fundamental and harmonic frequencies. It was found that the majority of the IV waveforms are captured by the fundamental, second, and third harmonic, and so the DC (first FFT bin) and higher than third harmonic (5th and higher FFT bins) data was not used. This is not the case for at least some systems where other harmonics can be non-negligible. Often the effect of systems which generate non-negligible higher harmonics are demonstrated in plasma series resonance articles, see for example Lieberman et al. (Lieberman et al., 2008).

To check that the time resolved FFT functions correctly, the FFT data is used to rebuild the IV signals and compared to the original data captured by the oscilloscope. The equation,

$$\Psi = \sum_{n=1,2,3} A_n(t) * cos(\omega * n * t - \phi_n(t)) \tag{2.1}$$

is used to rebuild the waveform from the FFT data, where Ψ is the full waveform, n the harmonic, $A_n(t)$ and $\phi_n(t)$ are the time resolved magnitude and phase for the given harmonic, and ω is the fundamental frequency. Since the FFT provides only one magnitude and phase data point for each rf period, an interpolation method is used to give these values ($A_n(t)$ and $\phi_n(t)$) within an rf period. Two interpolation methods are demonstrated for $A_1(t)$ (fundamental frequency magnitude) in Part **a** of Figure 2.2, where each time grid element represents a 75 ns rf period. As can be seen, the linear interpolation gives values on a straight line between two time resolved FFT data points, while the nearest interpolation gives values corresponding to the nearest in time (x axis) FFT data point. Similar results are found at the harmonics, and for $\phi_n(t)$. The results of rebuilding the full waveform (Equation 2.1) using these two interpolation methods are compared to the original oscilloscope measured data in Part **b** of the figure. There was a low frequency offset in the measured signal and so 0.085 was added to the rebuilt signals, allowing the rf frequency portion of the signals to be compared. The first rf cycle is generally a partial cycle, and both methods have some trouble reproducing it, however for every cycle after, the error is less than 5%. At steady state there is little difference in the methods and both have an error of less than 2%. With the exception of the first rf cycle, the rf period time resolved FFT represents the data well, and can be used with confidence.

With the time resolved FFT satisfactorily representing the measured data, frequency dependent probe calibration factors and chamber impedance effects can be applied to the measurements. The magnitude and phase responses of the IV probes vary with signal frequency. Therefore both a phase and magnitude calibration factor must be found for each probe at all frequencies of interest. These can be found using the 50 Ω input of an oscilloscope and then applied to the measured signals as described by Poulose et al. (Poulose et al., 2017). The calibration is performed by connecting the probe box power feedthrough to a 50 Ω oscilloscope input. The IV probes are connected to other channels in the oscilloscope in the usual manner. In this way, the voltage waveform of the signal being measured can be read on the oscilloscope and compared to the resulting signals from the IV probes. Since the oscilloscope input is 50 Ω, the magnitude of the driving signal current can be found using Ohm's Law, and the voltage and current are in phase. The probe measured signals are compared directly to the driving signal being measured, therefore this method takes into account both the parasitic impedance of the probes, and signal propagation delay of the probe leads. After the calibration factors are applied, the IV magnitude and phase are measured correctly at the probe measurement point, some distance away from the electrode. To find these values at the electrode-plasma interface, chamber parasitic impedances and signal propagation delay must be taken into account.

2.4.1 Chamber Parasitic Impedances

Parasitic impedances between the measurement point and electrode must be accurately determined and accounted for to calculate the waveforms at the plasma-electrode interface.

The parasitic impedances are distributed elements, but can be reasonably modeled as lump circuit elements at the frequencies reported in this chapter. The lump circuit model used here is similar to those used to model GEC reactors by Verdeyen and Sobolewski (Verdeyen, 1992; Sobolewski, 1992, 1995), and is shown in Figure 2.3 with pertinent chamber components. To assist the reader, measurement points which are either the point at which the RFIV probes are connected, or the plasma-electrode interfaces are shown using bold letters. These points are also where the vector network analyzer (VNA) is attached to measure the parasitic impedances. Points **A** and **A'** denote the powered pin and ground shield of the type N connector between the powered electrode RFIV probes, and the electrode assembly circuit. **D** and **D'** are the same for the grounded electrode. This is where the short is applied to ground the grounded electrode. **B** and **B'** are the electrode and its ground shield for the powered electrode, while **C** and **C'** are the same for the grounded electrode. L_C and C_C, are the inductance and shunt capacitance of the transmission line and connector. L_E, and R_E are inductance and resistance of the copper heat sink and aluminum electrode, while C_E is the shunt capacitance. L_{Eg}, R_{Eg}, and C_{Eg} are the grounded electrode inductance, resistance, and shunt capacitance. I_m, V_m, and I_{mg} are the IV measured by the powered and grounded electrode probes. I_p, V_p, I_{pg}, and V_{pg} are the currents through the plasma-electrode sheaths, and electrode voltages. I_w is the current to the electrode ground shields and chamber walls. To calculate these IV, the parasitic impedance values must be found.

Circuit element values for the circuit model are found so that they match the physical circuit's measured frequency dependent input impedance. This is measured using an Agilent Technologies E5061B VNA. The VNA was connected to a measurement point using a 50 Ω type N cable. To calibrate for the impedance of the cable, an HP 85032B calibration kit was used. Four measurements were performed for each electrode assembly. The input impedance measurements were made at the type N connector (**A**-**A'** or **D**-**D'**) with the electrode face (**B**-**B'** or **C**-**C'**) open or shorted to its ground shield. Next the input impedance measurements

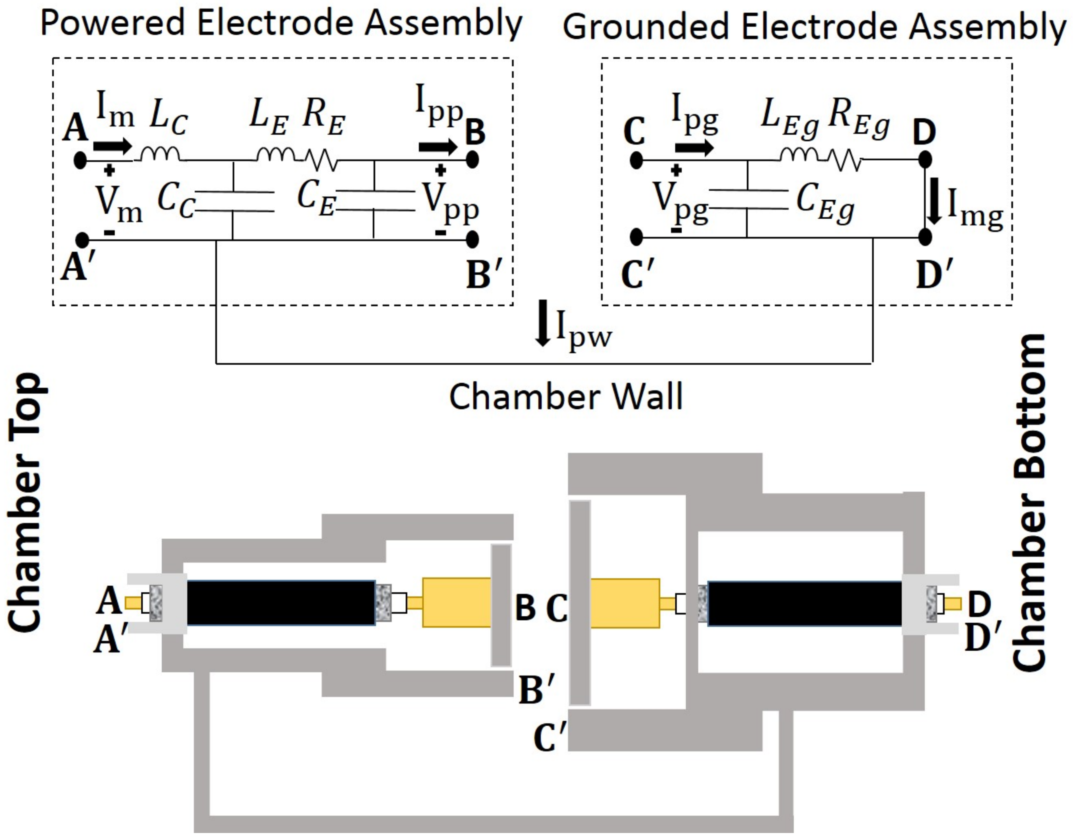

Figure 2.3. mGEC chamber lump element equivalent circuit model and components (rotated 90° counterclockwise and not to scale).

were made at the electrode face (**B-B'** or **C-C'**) with the type N connector open or shorted. To make the second set of measurements, an adapter was used to connect the type N cable attached to the VNA, to the electrode face.

The adapter consisted of a type N to solder cup wall mount adapter (Amphenol RF Division 82-97), and two silver coated, copper ribbons 1.6 cm wide by 6.35 cm long. One copper ribbon connected the electrode assembly ground shield (**B'** or **C'**) to the adapter body, while the other was pressed to the electrode face (**B** or **C**) using a dielectric squeezed between the two electrode faces, and soldered to the adapter cup. The adapter adds some series inductance (L_A) and shunt capacitance (increases C_E or C_{Eg}) to the system which must be accounted for in the equivalent circuit. L_A is directly measured, while the value

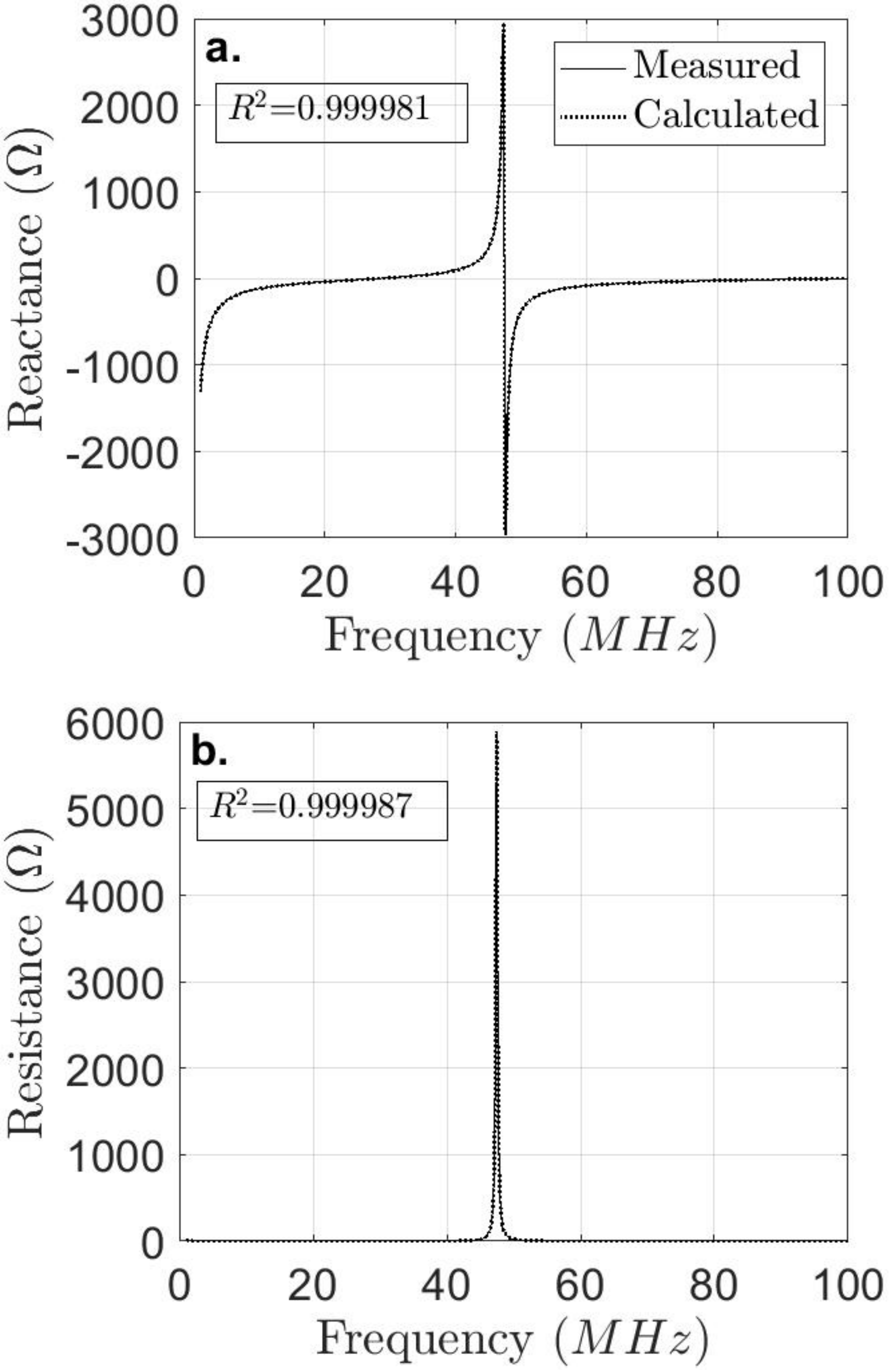

Figure 2.4. Measured powered electrode circuit input impedance at Point **A** - **A'** (**B** - **B'** open), with equivalent circuit calculated reactance and resistance after iterative optimization.

for C_E or C_{Eg} measured from **A**-**A'** or **D**-**D'** with **B**-**B'** or **C**-**C'** in the open configuration is used eliminating the added capacitance of the adapter. The VNA measured each circuit configuration input impedance for frequencies 1-100 MHz. An in-house iterative program is then used to match the measured input impedance with the calculated input impedance of the equivalent circuit for given circuit values. The program allowed the user to visually match the impedances while changing lump element circuit values. After a reasonable match was found, the program iterates through circuit element test values to bring the coefficient of determination (R^2) between the measured and calculated impedances close to one. Each measurement was matched with $R^2 > 0.999$. An example of the matched values measured at **A** and **A'** with **B** and **B'** in the open configuration is shown in Figure 2.4. The resulting parasitic impedance values are shown in Table 2.1. The values given are the averages found from the various circuit configurations, while the error is the maximum deviation from the average. With the parasitic impedance values known, the IV measured at the probes, can be converted to those at the electrode-plasma interface through the use of an abcd parameter matrix, or by solving for the IV at each circuit node.

The reader must note that the powered electrode assembly probe measurement of the fundamental frequency IV (sourced by the power amplifier) is "upstream" from the electrode-plasma interface, whereas the probe measurement for the harmonic frequencies in the powered electrode and at all frequencies in the grounded electrode (sourced by the plasma) are "downstream" from the plasma-electrode interface and the abcd matrix or IV node calculations (shown in the following subsection) should be carried out accordingly. Finally, this solution only treats the effects of the parasitic impedances, for a higher degree of accuracy, the signal propagation time through the chamber circuitry must also be taken into account.

Table 2.1. Calculated lump circuit element values for the powered and grounded electrode assemblies.

Powered Electrode		Grounded Electrode	
L_C	$50.6 \pm 1.7\ nH$		
C_C	$51.7 \pm 1.4\ pF$	C_{Cg}	$30.0 \pm 1.3\ pF$
L_E	$377 \pm 5\ nH$	L_{Eg}	$140.2 \pm 4.4\ nH$
C_E	$70.8 \pm 0.4\ pF$	C_{Eg}	$163.4 \pm 3.5\ pF$
R_E	$0.7 \pm 0.1\ \Omega$	R_{Eg}	$1.1 \pm 0.2\ \Omega$
L_A	$18.2 \pm 0.2\ nH$	L_A	$26.1 \pm 0.7\ nH$

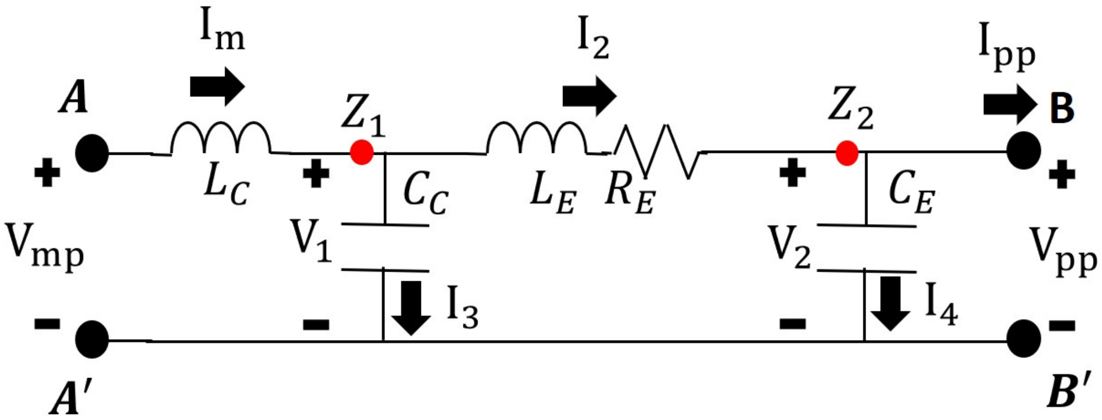

Figure 2.5. Powered electrode components including current, voltage and node labels used to find the IV at the electrode from the IV measured.

2.4.2 IV Parasitic Impedance Correction Calculations

In this subsection the calculations to find the IV at the electrode face given the IV at the probe measurement point are shown. First the input impedance measured at the probe is found for the fundamental frequency.

$$Z_{probe\ fund} = \frac{V_{prob\ fund}}{I_{prob\ fund}} \tag{2.2}$$

where $V_{probe\ fund}$ and $I_{prob\ fund}$ are the fundamental frequency complex values of the probe measured current and voltage. The equation for lump element circuit impedance for $Z_{probe\ fund}$ is given by

$$Z_{probe\ fund} = Z_{L_C} + \frac{1}{\frac{1}{Z_{C_C}} + \frac{1}{Z_{L_E}+Z_{R_E}+\frac{1}{\frac{1}{Z_{C_E}}+\frac{1}{Z_{plasma}}}}}. \tag{2.3}$$

The fundamental frequency plasma input impedance can then be found by;

$$\frac{1}{Z_{probe\ fund} - Z_{L_C}} = \frac{1}{Z_{C_C}} + \frac{1}{Z_{L_E} + Z_{R_E} + \frac{1}{\frac{1}{Z_{C_E}} + \frac{1}{Z_{plasma\ fund}}}} \tag{2.4}$$

$$\frac{1}{\frac{1}{Z_{probe\ fund}-Z_{L_C}} - \frac{1}{Z_{C_C}}} = Z_{L_E} + Z_{R_E} + \frac{1}{\frac{1}{Z_{C_E}} + \frac{1}{Z_{plasma\ fund}}} \tag{2.5}$$

$$\frac{1}{\frac{1}{\frac{1}{Z_{probe\ fund}-Z_{L_C}} - \frac{1}{Z_{C_C}}} - Z_{L_E} - Z_{R_E}} = \frac{1}{Z_{C_E}} + \frac{1}{Z_{plasma\ fund}} \tag{2.6}$$

$$\frac{1}{\frac{1}{\frac{1}{\frac{1}{Z_{probe\ fund}-Z_{L_C}} - \frac{1}{Z_{C_C}}} - Z_{L_E} - Z_{R_E}} - \frac{1}{Z_{C_E}}} = Z_{plasma\ fund}. \tag{2.7}$$

Next, two equivalent methods are used to solve for the electrode current and voltage. The methods are redundant but allow the implementation of the equations to be checked for errors. Starting with $I_m = I_2 + I_3$, then using Ohm's Law

$$\frac{V_{mp}}{Z_{probe\ fund}} = \frac{V_1}{Z_1}, \tag{2.8}$$

and so

$$V_1 = \frac{V_{mp} Z_1}{Z_{probe\ fund}}, \tag{2.9}$$

This is where this method will differ from the following method. Using the found voltage (V_1), I_2 can be found using

$$I_2 = \frac{V_1}{Z_{L_E} + Z_{R_E} + Z_2}. \tag{2.10}$$

The voltage at the electrode (V_{pp}) is then given by

$$V_{pp} = I_2 Z_2. \tag{2.11}$$

The second method is then used to solve for the current through the plasma. We again start with $I_m = I_2 + I_3$, and using Ohm's Law

$$\frac{V_{mp}}{Z_{probe\ fund}} = \frac{V_1}{Z_1}, \tag{2.12}$$

and so

$$V_1 = \frac{V_{mp} Z_1}{Z_{probe\ fund}}. \tag{2.13}$$

Here is where this method will differ from the first method. I_2 is found through subtraction rather than equal ratios using

$$I_2 = I_m - I_3 = I_m - \frac{V_1}{Z_{C_C}}, \tag{2.14}$$

Then

$$V_2 = I_2 Z_2, \tag{2.15}$$

and

$$I_{pp} = I_2 - I_4 = I_2 - \frac{V_2}{Z_{C_E}}. \tag{2.16}$$

The equations are implemented properly if the equation

$$Z_{plasma} = \frac{V_{plasma}}{I_{plasma}} \tag{2.17}$$

holds true, where Z_{plasma} was calculated from the circuit impedances and the impedance measured at the probe, V_{plasma} was calculated using the first method, and I_{plasma} was calculated using the second.

With the plasma input impedance, current and voltage known at the fundamental frequency, the matching network input impedance, and plasma voltage and current are found at the 2nd and 3rd harmonic frequencies. Because the harmonic waveforms are traveling in the opposite direction "downstream" is from right to left at the harmonic frequencies switching the direction of components to be counted in Z_1 or Z_2. First the input impedance measured at the probe ($Z_{match\ har}$) is found at each harmonic frequency.

$$Z_{match\ har} = \frac{V_{prob\ har}}{I_{prob\ har}}. \tag{2.18}$$

The input impedance of the electrode from the plasma is then given by

$$Z_{plasma\ har} = \frac{1}{\frac{1}{ZC_E} + \frac{1}{ZL_E + ZR_E + \frac{1}{\frac{1}{ZC_C} + \frac{1}{ZL_C + Z_{match}}}}}. \tag{2.19}$$

The first method to solve for the harmonic frequency electrode IV starts by finding V_1 using

$$I_M = \frac{V_1}{Z_1} \tag{2.20}$$

$$V_1 = I_M * Z_1 \tag{2.21}$$

I_2 is found using

$$I_2 = \frac{V_1}{Z_1} + \frac{V_1}{Z_{C_C}}. \tag{2.22}$$

Then V_{pp} is found using

$$I_2 = \frac{V_{pp}}{Z_2} \tag{2.23}$$

$$V_{pp} = I_2 Z_2. \tag{2.24}$$

I_{pp} is found using

$$I_{pp} = I_2 + \frac{V_{pp}}{Z_{C_E}}. \tag{2.25}$$

These steps are followed for both the second and third harmonic, and a similar process is followed for the grounded electrode.

2.4.3 Signal Propagation Delay

The IV measured at the probe takes some time to reach the electrode or vice versa for signals originating at the electrode. This "electrical length" of the system will cause some phase shift which can become important depending on the distance between the measurement point and electrode face. The electrical length was measured by the VNA from **A** and **A'** with **B** and **B'** shorted for the powered electrode assembly. This gives the results shown in Figure 2.6, and represents the time for the signal to propagate down and back. The electrical length is then half the found values, with the same method repeated for the grounded electrode assembly. The phase shift of the fundamental frequency IV on the powered electrode is given by $\Delta\phi_1 = 2\pi f_1 E_L(f_1)$ where $E_L(f_1)$ is the electrical length at the fundamental frequency, and f_1 is the fundamental frequency. The second and third harmonics IV phases are shifted by $\Delta\phi_{2,3} = -2\pi f_{2,3} E_L(f_{2,3})$, where the shift is negative because they are propagating in the opposite direction. All of the signals are propagating from the plasma to the probe in the grounded electrode and so they are shifted by $\Delta\phi_{1,2,3} = -2\pi f_{1,2,3} E_L(f_{1,2,3})$. The results of this shift shown in Figure 2.7, demonstrate that the voltage envelop magnitude

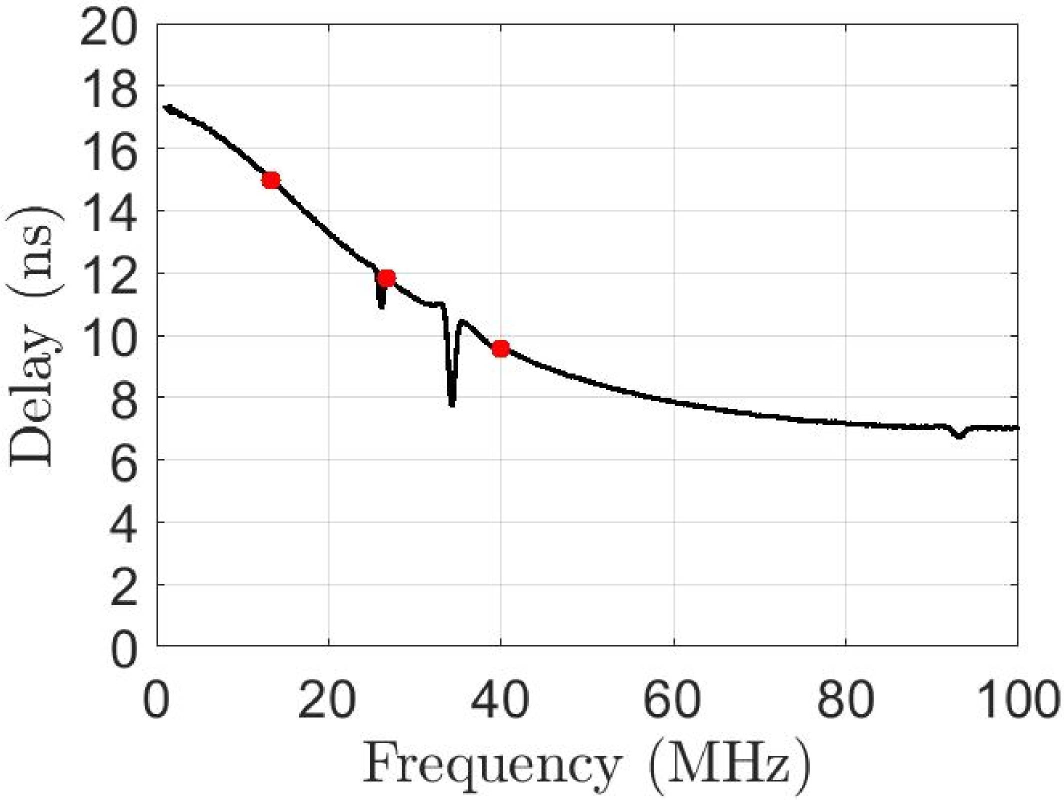

Figure 2.6. Measured signal propagation delay (from **A-A'** to a short at **B-B'** and back) as a function of frequency.

becomes larger and more symmetric (Part a). This is due to an increase in the constructive interference of the fundamental and harmonic waveforms (Part b). In the system presented here, the voltage maximum shift is $\approx 15\%$ and should not be ignored. With the voltage at each electrode, and the current through each sheath found, the next step is to separate the total voltage across the plasma into sheath-bulk-sheath voltages, and each sheath current into conduction and displacement currents.

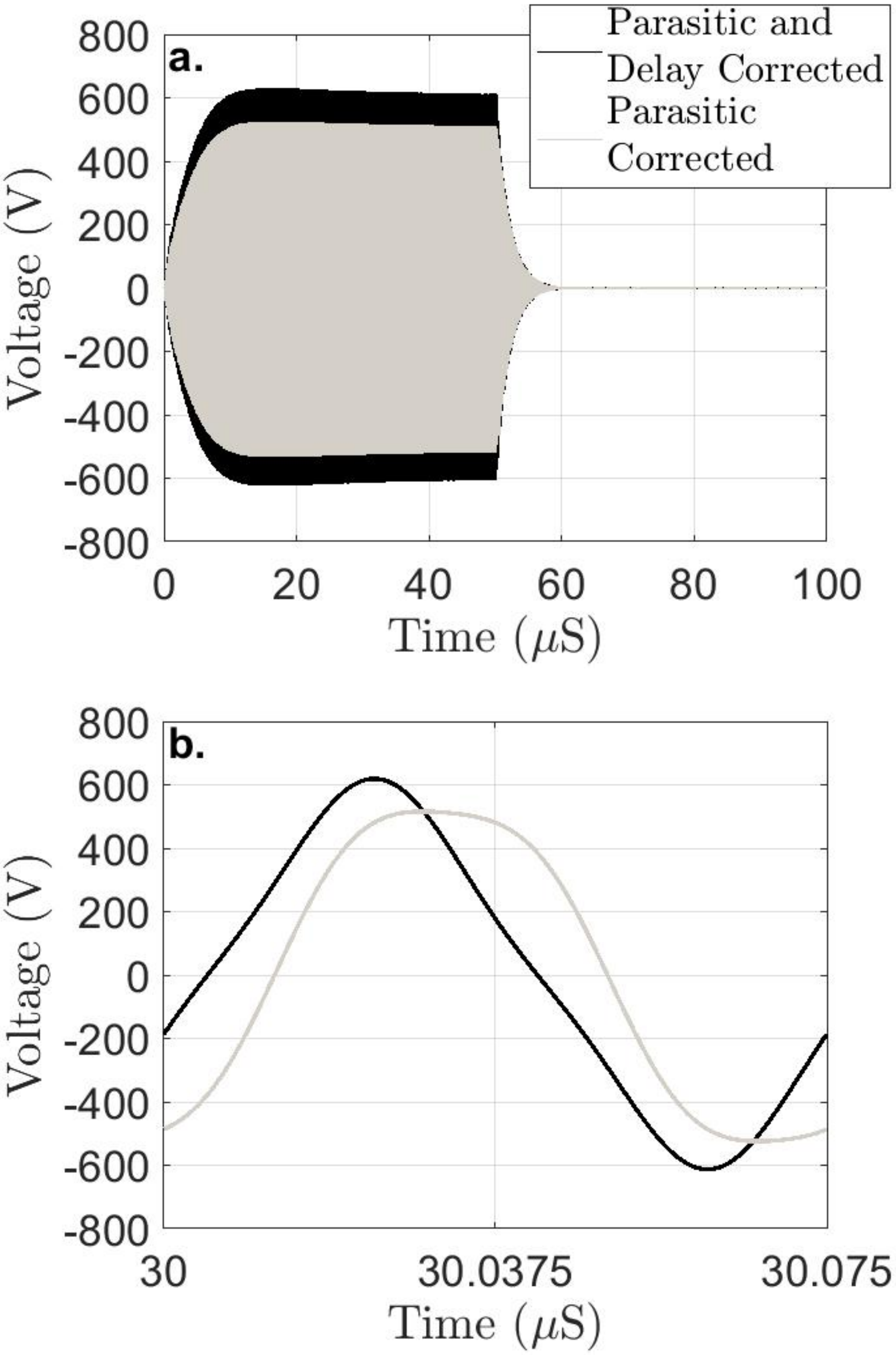

Figure 2.7. Affects of signal propagation delay on full pulse rf waveform envelope (Part **a**), and within an rf period (Part **b**). 75 mTorr, Ar, 10 kHz 50% duty cycle square wave pulsed plasma.

2.5 Separation of Total Voltage into Sheath and Bulk voltage

Heil et al. found an analytical method (Heil et al., 2008) (with more detail given by Czarnetzki et al. (Czarnetzki et al., 2011)) to separate the voltage across an rf driven continuous wave capacitively coupled plasma, into its powered and grounded sheath, and bulk components. In the cited articles, the model inputs were the rf voltage waveforms and a known symmetry value corresponding to the ratio of powered and grounded electrode area which could be used to separate the rf and DC voltages. In the system presented here the symmetry parameter is not known, however the DC voltage is measured separately from the rf, allowing for the calculation of the symmetry parameter. Otherwise their method is followed using the simplification of neglecting the floating sheath as it is much smaller than the input voltage. The results of the voltage separation are shown in Figure 2.8. Part **a** gives the instantaneous voltage from the powered electrode to ground (V_{pp}), across the powered sheath (V_{pps}), across the chamber wall sheath (V_{pgs}), and the plasma bulk (V_b). Part **b** is the instantaneous voltage to ground at the boundaries of the powered electrode (V_{pp}), powered electrode sheath-plasma bulk (V_{pps-b}), grounded electrode sheath-plasma bulk (V_{pws-b}), and grounded electrode V_{pg}. With time dependent values for sheath voltages found, the sheath current can be separated into conduction and displacement components.

2.6 Separation of Sheath Current into Conduction and Displacement Current

An approximation for the displacement and conduction current can be found by separating the measured current into even (conduction) and odd (displacement) symmetry components (Sobolewski, 1995). The axis of symmetry is where the sheath voltage magnitude is closest to zero. This procedure is performed for each sheath with the results shown in Figure 2.9. With this final step, each sheath is electrically characterized.

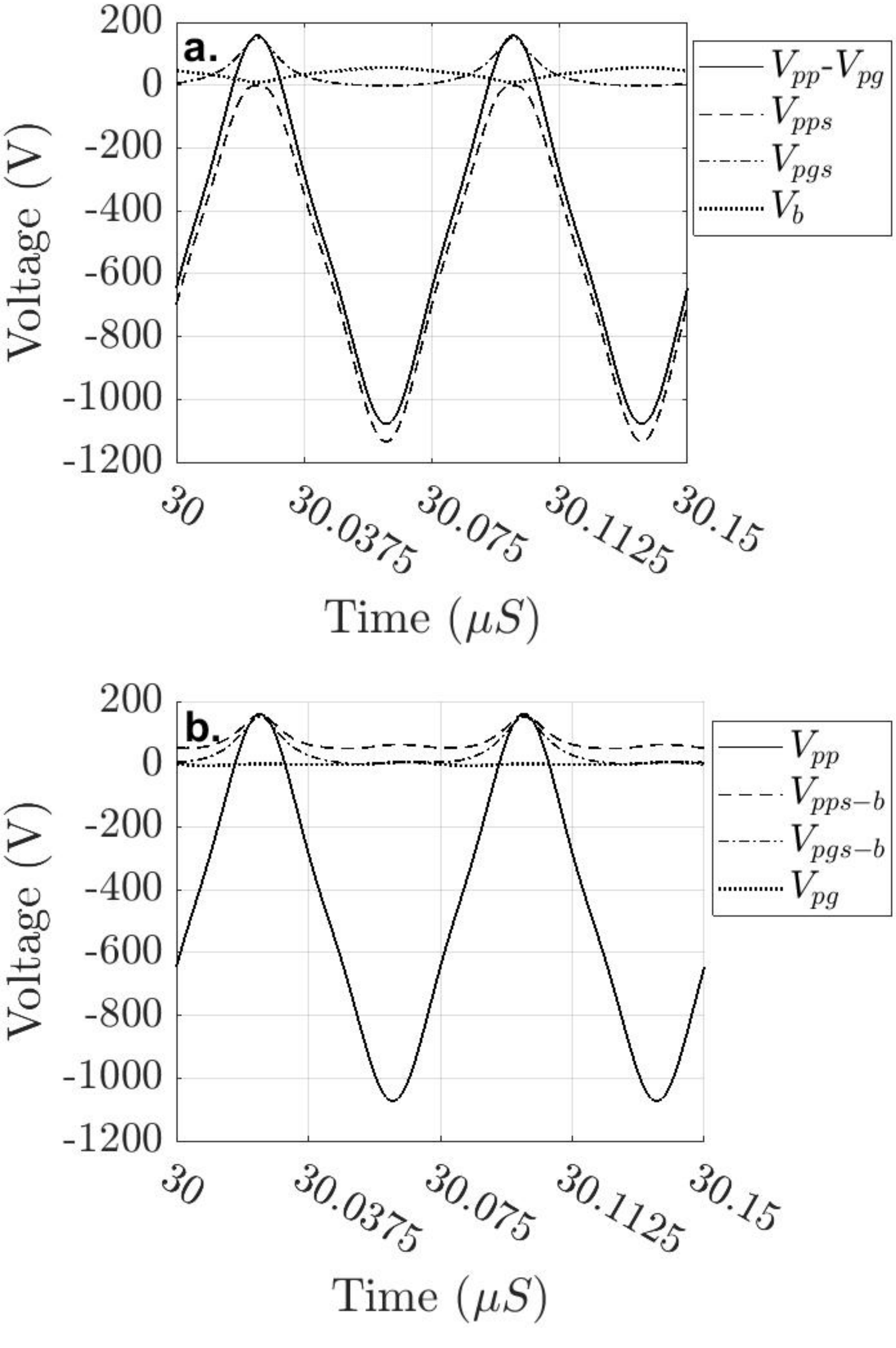

Figure 2.8. Part **a**, voltage to ground at the powered electrode (V_{pp}), across the powered sheath (V_{pps}), chamber wall sheath (V_{pgs}), and plasma bulk (V_b). Part **b**, voltage to ground at the powered electrode, powered sheath-plasma bulk boundary (V_{pps-b}), grounded electrode sheath-plasma bulk boundary (V_{pgs-b}), and grounded electrode (V_{pg}). 75 mTorr, Ar, 10 kHz 50% duty cycle square wave pulsed plasma.

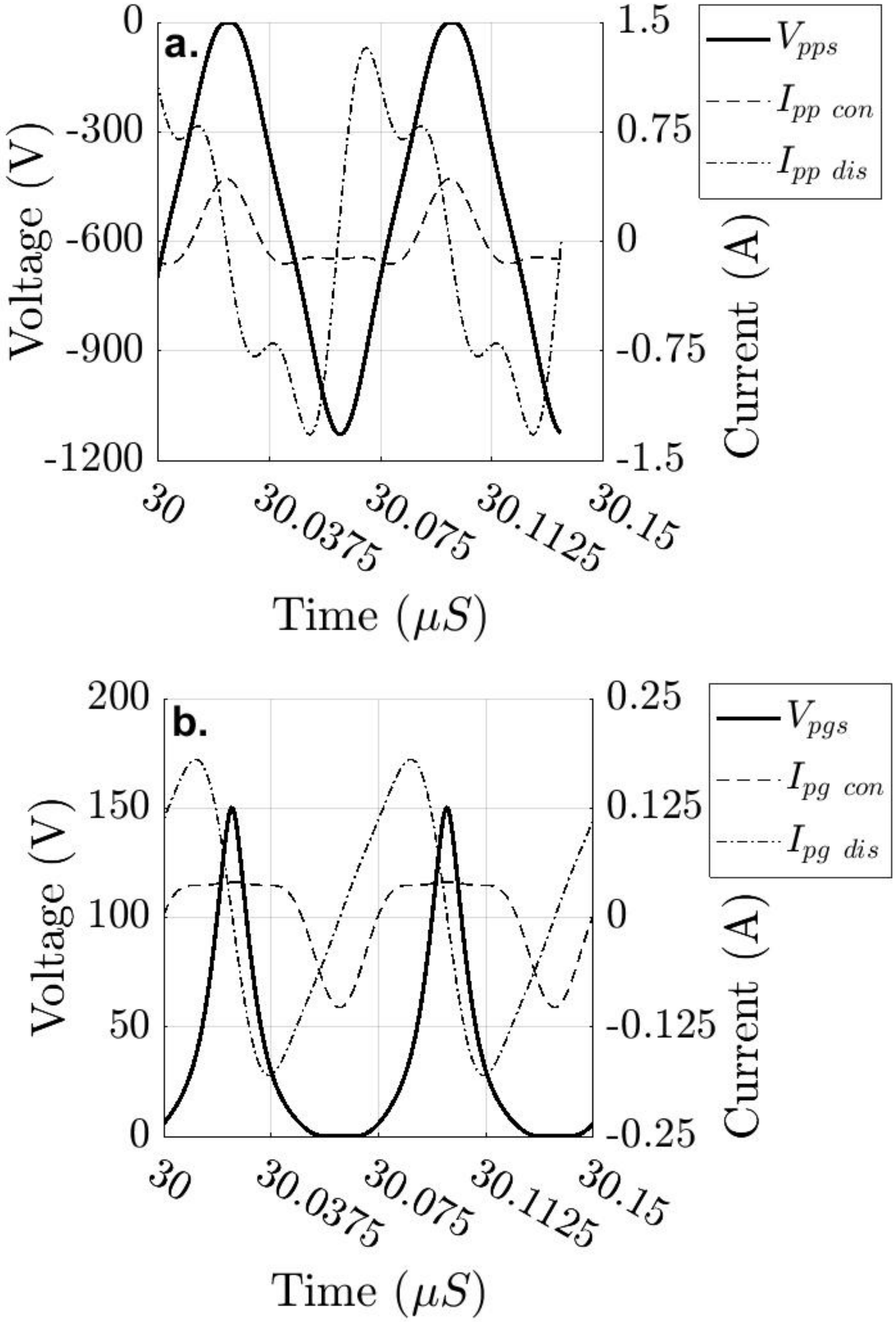

Figure 2.9. Sheath voltage (V_{pps} and V_{pgs} are the same as in Figure 2.8), conduction and displacement current through the powered (Part **a**), and grounded electrode (Part **b**). Positive current in the powered electrode sheath (Part **a**), denotes sheath contraction and electron collection by the surface, while the opposite is true for the grounded electrode (Part **b**). 75 mTorr, Ar, 10 kHz 50% duty cycle square wave pulsed plasma.

2.7 Discussion

Figure 2.10 shows the input power and impedance at the fundamental frequency at the IV probe measurement point (not taking chamber parasitics into account), and the plasma-electrode interface (parasitics taken into account). Part **a** shows the active input power measurement at the probe, and the powered electrode-plasma interface. Less power is going into the plasma than measured at the probe as some is absorbed by the parasitic impedances. Not accounting for parasitic impedances causes an $\approx 18\%$ overestimation in input power at steady state. The calculated series reactance (Part **b**) is ≈ 8 times smaller in magnitude at steady state when not taking parasitic impedances into account. Similarly the calculated uncorrected series resistance (Part **c**) is ≈ 26 times smaller at steady state. It is therefore important to understand the parasitic impedances of a system when accurate IV measurements are required.

Using these corrected measurements, several observations can be made. As power is applied to the plasma, the DC sheath builds, increasing the capacitive impedance of the plasma. The resistance is also seen to increase in magnitude, corresponding to increased power absorption in forms such as ion acceleration, ionization, excitation, and thermalization. When the power is turned off at 50 μs, the reactance magnitude increases, indicating that removing rf power increases the effective sheath width, while resistance decreases indicating less power absorption in the plasma.

Unlike the parameters derived from a single frequency, when multiple frequencies interact propagation delay correction becomes important. The IV across the powered and grounded electrode sheaths are shown with propagation delay correction (Figure 2.9), and without (Figure 2.11). From Figure 2.9 it can be seen that the sheath voltage waveforms are sharper at large magnitudes and change more gradually when they approach zero. This is due to the model used to separate sheath and bulk voltages' assumption that the sheath charge-voltage relationship is quadratic as demonstrated by Schulze et al. (Schulze et al., 2008). The

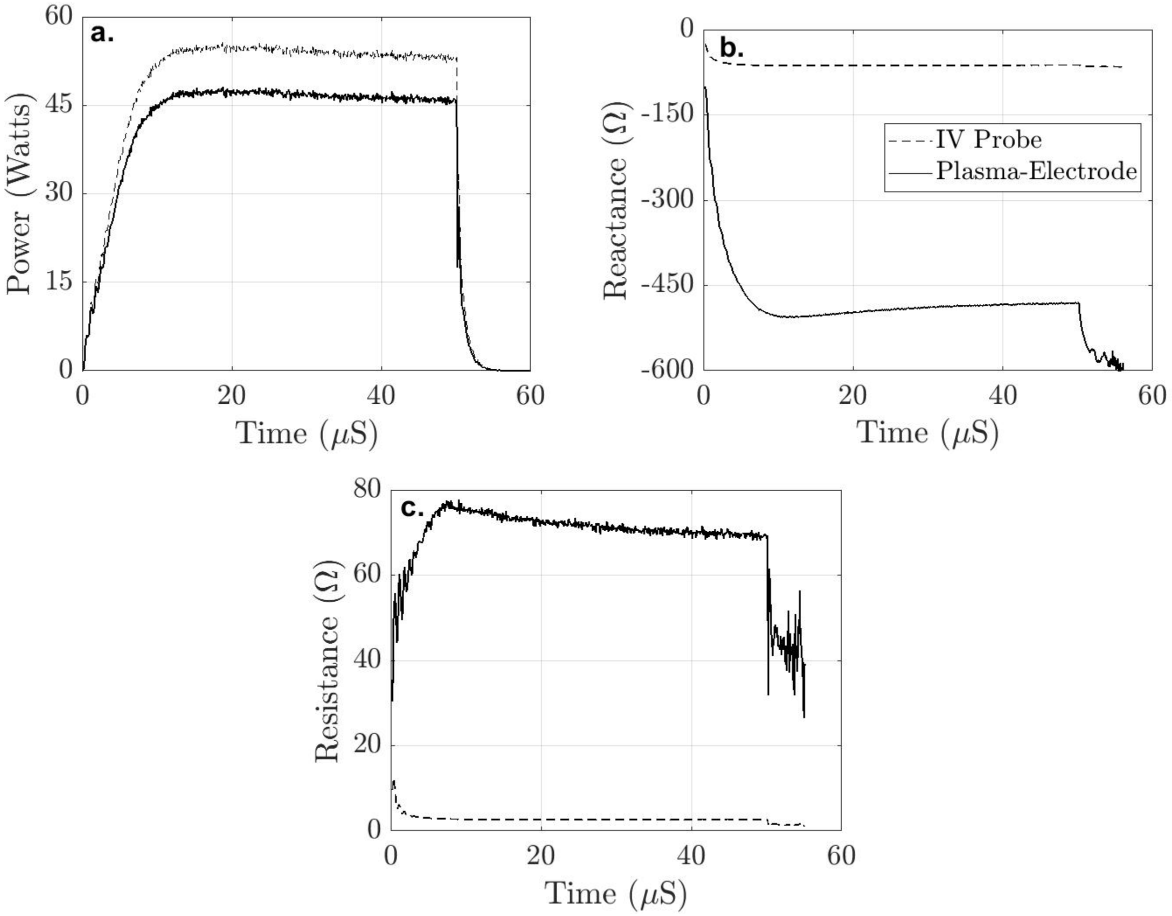

Figure 2.10. Measured power and impedance with (plasma-electrode) and without (IV probe) parasitic impedance correction. Parts **a**, **b**, and **c**; power, series reactance and resistance. Data after ≈ 55 μs has been removed as the current and voltage magnitudes are ≈ 0 causing the resulting calculations to be dominated by noise. 75 mTorr, Ar, 10 kHz 50% duty cycle square wave pulsed plasma.

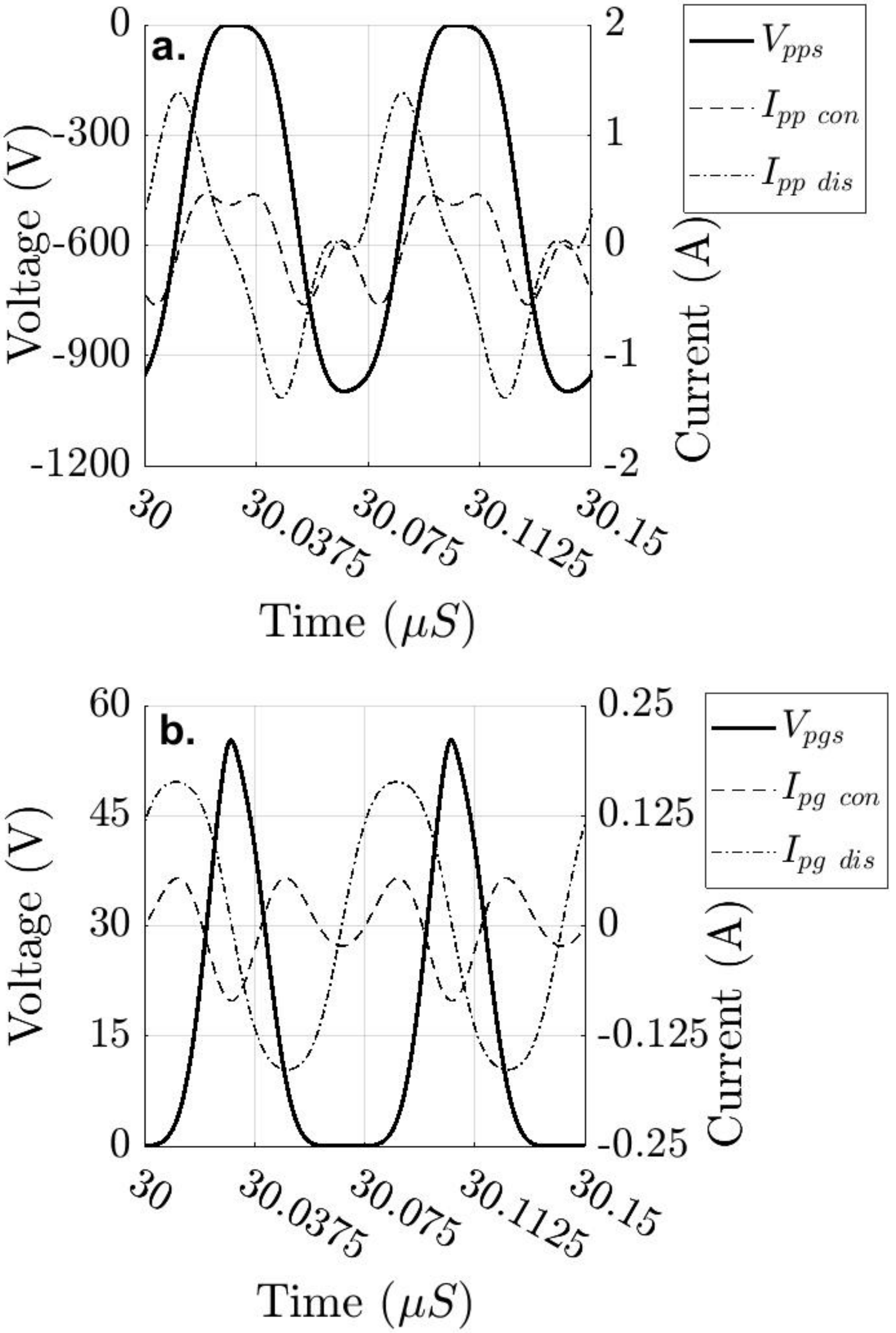

Figure 2.11. Repeat of Figure 2.9 without accounting for propagation delay. 75 mTorr, Ar, 10 kHz 50% duty cycle square wave pulsed plasma.

conduction current through the powered ($I_{pp\ con}$) and grounded electrode ($I_{pg\ con}$) show an electron spike at sheath voltage magnitude minimum and constant background ion current consistent with earlier experimental results (Sobolewski, 1995). Note current is defined as moving from the powered electrode into the plasma and then through the grounded electrode or chamber wall as shown in Figure 2.3, and so positive conduction current through the powered electrode represents electrons moving from the plasma to the electrode, while the opposite is true for the grounded electrode. The displacement current in each sheath is skewed from a sinusoid. This was also found by Sobolewski (Sobolewski, 1995) and Klick (Klick, 1996). To explain this, the displacement current was given as

$$I_{dis} \propto \frac{1}{s(t)} \frac{dV}{dt} \tag{2.26}$$

where $s(t)$ is the sheath width, and V is the sheath voltage. Then when $s(t)$ is small (minimum sheath voltage magnitude) I_{dis} is larger for a given dV/dt. Therefore I_{dis} maximums and minimums are expected to occur close to when $s(t)$ is small if V is a sinusoid. However both the $I_{pw\ con}$ and $I_{pg\ con}$ are skewed in the opposite manner. As mentioned at the beginning of this section, the sheath voltages are not sinusoidal and the magnitude of dV/dt is smallest around $s(t)$ minimums. For the results presented here this effect dominates the dependence on $s(t)$, and the relationship of minimum $s(t)$ at minimum V and maximum $s(t)$ at maximum V is maintained. With this understanding, the calculated waveforms when propagation delay is not taken into account can be considered.

Figure 2.11 shows sheath voltage and current when propagation delay is not considered and several inconsistencies can be noticed. The most obvious is the conduction current does not show reasonably constant ion current over the full period, and narrow electron current around the minimum sheath voltage magnitude. In fact, in the grounded electrode sheath, the maximum electron current to the electrode is shown to occur when the sheath is at its maximum. It is harder to find definitive fault with the displacement current as the instantaneous sheath impedance is not known and separating the current into symmetric and antisymmetric portions puts displacement current zero crossings at sheath voltage maxima and minima. However, it can be noticed that for a short period in the powered electrode sheath, just before 30.075 and 30.15 μs, $I_{pp\ dis}$ is slightly negative while V_{pps} is becoming more positive, indicating an inductive current-voltage relationship. During this period the sheath width is close to its maximum causing the capacitive reactance to be maximized, while the current is small causing the inductive reactance to be minimized. Therefore the calculated inductive current-voltage relationship is evidence of error caused by ignoring propagation delay.

2.8 Conclusion

An rf period time resolved FFT method can reasonably reproduce time varying rf plasmas IV waveforms. The frequency separation of the IV allows for calibration of frequency dependent probes and parasitic impedances. That in conjunction with taking into account the direction of travel and propagation delay of the fundamental and harmonic components of the IV, results in the electrode voltages and sheath currents. Using the method of Heil et al. (Heil et al., 2008) during the pulse steady state, the voltage across the plasma can be separated to find the sheath and bulk voltages. Finally, using even and odd symmetry, the sheath currents can be separated into conduction and displacement currents (Sobolewski, 1995), giving time resolved fully characterized plasma-surface electrical measurements.

CHAPTER 3

PULSED POWER PLASMA TURN ON

3.1 Introduction

Using results from the system described in Chapter 2, the pulsed power build up region can be studied. In CW plasmas, the details of the DC bias, and resonant match network-chamber-plasma circuit at the fundamental frequency aren't overly important so long as they produce the same IV at the plasma. It is worth noting that circuits which are identical at the fundamental frequency may not be at higher frequencies, and their details can become important (Rauf and Kushner, 1998). In power pulsed plasma the details of the components greatly change the IV build up and therefore the electric and magnetic fields experienced by the plasma during the power start up. When properly matched, the combination of the match network, chamber, and plasma impedances form a nearly resonant circuit at the driving frequency. This allows the magnitude of the current and voltage across the plasma to be much larger than that sourced by the rf power amplifier. When studying CW plasmas, this can be taken for granted as the build up of the fields inside the circuit match network is relatively unimportant. As well, CW matching is relatively simple when compared to pulsed power matching as the impedance does not change in time. Methods to deal with changing impedance such as controlling the rf frequency have been studied to decrease the unmatched period (Chen et al., 2002; Banner et al., 2012; Bishara and Banna, 2014). In this chapter, a method in which the rf power is built up faster than usual will be shown to decrease the unmatched period without changing the driving frequency.

As a starting point, the details of the IV build up will be introduced after the experimental setup. First, the build up of the fundamental frequency in a resonant circuit will be described (Section 3.3). This is followed by the DC bias voltage build up (Subsection 3.3.1), and harmonic frequency build up (Subsection 3.3.2). This will fully describe the build up of the

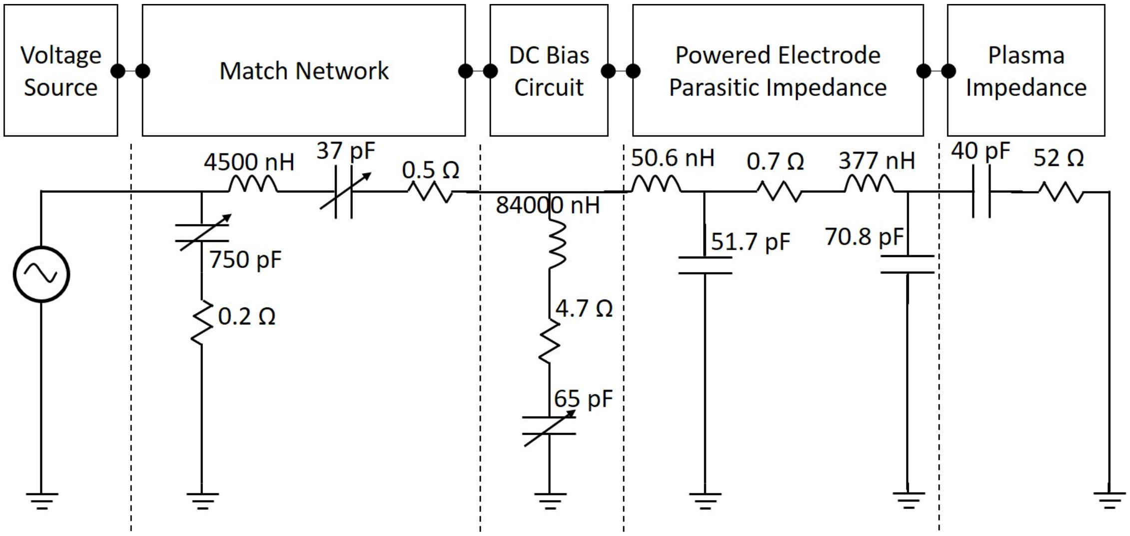

Figure 3.1. Power delivery system block diagram and associated circuit elements. Given values are those used in the Simulink model.

fields interacting with the plasma. Section 3.4 shows how the plasma input impedance varies in time. It is then shown that the impedance can reach its steady state value more quickly through control of the DC bias and rf voltage build up. Finally with an understanding of the build up mechanisms, data which explains etch feature charge neutralization in rapidly pulsed plasmas is explained in Section 3.6.

3.2 Experimental Setup

The plasma chamber, and current and voltage measurement system are described in Chapter 2. The physical power delivery system components, and equivalent Simulink model circuit are shown in Figure 3.1. The voltage source is an ENI A-300 controlled by a Keysight 33622A arbitrary waveform generator. This setup allows for square wave, as well as user defined amplitude modulation shape, power pulsing. This is modeled in Simulink by an ideal voltage source which can be controlled by user created functions. The matching network is an L-type design (modified Advanced Energy AM-5), and is modeled by a variable shunt (load) capacitor in series with a small resistance, and a series variable (tune) capacitor in series with an inductor and a small resistance. The value of the inductor was estimated to be 4500 nH, while the load capacitor was variable from 480-880 pF (set to750 pF), and the tune capacitor was variable from 5-500 pF (set to 37 pF). The DC bias measurement circuit consists of a shunt series Ohmite Z7 choke (84000 nH, 4.7 Ω) and a variable capacitor. The DC bias voltage was measured across the capacitor. The capacitor values used in this study were either 65, 880, 2000, or 5000 pF. A DC power supply could also be attached across the DC bias capacitor and used to provide the DC bias. The Simulink model used only a 65 pF capacitor. The powered and grounded electrode circuits are modeled in the simulation using the lump circuit model element values described in Chapter 2. The plasma and grounded electrode are simulated by a series resistor and capacitor giving a resistance of 52 Ω and a reactance of -298 Ω, which was the measured input impedance of a steady state argon plasma. This configuration is a very basic plasma model and will not produce harmonics or DC bias. However, it can be used to track power delivery at the fundamental frequency with a plasma load impedance. The Simulink model uses the Simscape power systems library and is solved using the MATLAB ODE45 library. The simulation timestep is variable, however the power source timestep was set at 200 pS.

3.3 Pulsed power in a resonant circuit

When a modulated rf signal is applied to the match network-chamber-plasma resonant circuit, the amplitude of the IV at the applied (fundamental) frequency will have a characteristic build up time when power is increased, and decay time when power is decreased. This behavior can be explained as the input power (P_{in}) going into both driving the resistive and reactive portion of the load. The resistive portion of the load results in power lost (P_{out}), and consists of resistance in the match network and chamber components, as well as plasma processes such as build up of the IV at harmonic frequencies and DC bias, and deposited into charged and neutral particles. The reactive portion can be expressed as the change in time of the potential energy (U) stored in the electric and magnetic fields of the reactive elements. The power balance for the fundamental frequency can then be given as

$$P_{in} - P_{out} = \frac{dU}{dt}. \tag{3.1}$$

U can be expressed as the stored energy in circuit components and circuit equivalent plasma components. U is then given by

$$U = \frac{1}{2}C_{eq}V^2 + \frac{1}{2}L_{eq}I^2, \tag{3.2}$$

where C_{eq} is the equivalent capacitance, V is the voltage across C_{eq}, L_{eq} is the equivalent inductance, and I is the current through L_{eq}. The build up time is then dictated by the time necessary for the IV to become large enough that $P_{out} = P_{in}$ and steady state is reached. The decay time is set by equation 3.2 when $P_{in} = 0$. The build up of the simulated and measured voltage waveform can be seen in Figure 3.2. In Part **a**, the simulated applied voltage coming from the rf amplifier is shown, while the corresponding simulated voltage across the plasma is shown in Part **b**. Also shown is the measured build up of the fundamental and harmonic frequency and DC bias voltage magnitudes. As can be seen, the simulated and measured results agree reasonably well, with the exception that the measured fundamental frequency voltage builds up slower than in the simulation. This is because, in addition to the power going into the fundamental frequency build up, power is flowing into building up the harmonic frequencies and DC bias which are discussed in the next subsections.

3.3.1 DC bias build up

A DC bias voltage forms in physically (Köhler et al., 1985; Lieberman and Lichtenberg, 2005) or electrically asymmetric (Schulze et al., 2009; Czarnetzki et al., 2011) discharges. This is the voltage necessary to balance negative and positive current to a surface over the rf period

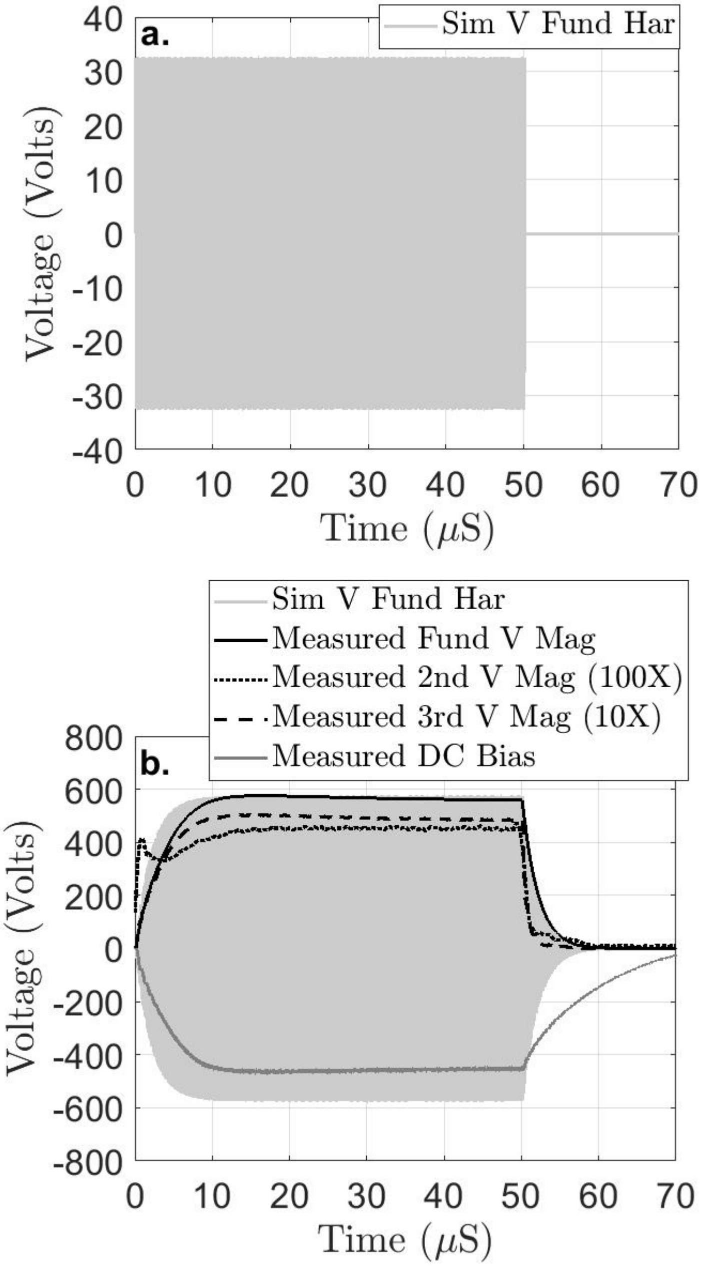

Figure 3.2. Simulation and measurement of voltage build up. Part a. Simulation rf input voltage set to a 13.33 MHz sine wave with 26 volt magnitude, modulated by a 10 kHz square wave. Part b. Powered electrode simulation voltage and measured voltage magnitude at the fundamental, second and third harmonic, and dc bias voltage. 75 mTorr, Ar, 10 kHz 50% duty cycle square wave pulsed plasma.

(discussed in Chapter 1). The time and power necessary to build up the DC bias depends strongly on the total capacitance (C_{DC}) to ground of the portion of the circuit before the match network blocking capacitor. In the system presented here, this includes the chamber parasitics, the DC bias capacitor and match network blocking (tune) capacitor. To reach a given bias voltage, a higher capacitance will require both a larger amount of power (Equation 3.2), and current, given by

$$V_b = \frac{Q}{C_{DC}} \tag{3.3}$$

where V_b is the bias voltage, and Q the charge on the capacitor given by

$$Q = \int_{t(V_b=0)}^{t} I(t) \tag{3.4}$$

where I is the charged particle current to the electrode surface. The result is that changing C_{DC}, will change the sheath voltages when rf power is applied and removed. This can be seen in Figure 3.3 for five experimental C_{DC} configurations. The variable capacitor in the DC bias circuit is adjusted so that $C_{DC} \approx 230\ pF$ (Part **a**), $C_{DC} \approx 1040\ pF$ (Part **b**), and $C_{DC} \approx 5160\ pF$ (Part **c**). In Part **d**, a DC power supply was attached in place of the variable capacitor but not turned on. The output capacitance of the supply was large enough that the DC bias voltage does not measurably change during a power pulse cycle. In Part **e**, the power supply was turned on so that the DC bias voltage magnitude was slightly larger than in Part **d**, allowing for much of the power necessary to maintain the DC bias to be supplied by the power supply, while not greatly disturbing the plasma in Part **d** otherwise.

In Part **a**, C_{DC} is small enough that the DC bias voltage builds up at almost the same rate as the fundamental frequency. This is in contrast to Part **b**, where the DC bias grows more slowly than the fundamental frequency. Because of this Part **b**, exhibits the "birds head" noticed by Booth et. al., (Booth et al., 1997), where the rf rises more rapidly than the DC bias allowing the positive voltage maximums to overshoot their steady state value. Build up of the DC bias corresponds with rf period averaged $\Gamma_e > \Gamma_i$ to chamber surfaces, causing the plasma potential to rise, often overshooting its steady state value before returning. The steady state value is larger than the off time value, however this change is primarily due to the increased electron temperature while the power is on. The change in plasma potential at the beginning of an rf pulse allows the sheath to remain electron repelling in periods where the DC bias is not large enough to offset the rf build up. However, for given electron density and temperature, increased electron collection is due to a smaller minimum sheath voltage than is attainable in CW. In Part **c**, C_{DC} is large enough that the positive ion current during the off time does not significantly reduce the DC bias, causing it to fluctuate from $-365\ V$ at 3.1 μs when the rf voltage positive maximums become large enough for electrons to reach the electrode surface, to $-400\ V$ at 50 μs when the rf voltage starts to decay. In Parts **d** and **e** the DC bias voltage does not measurably change with values of 408 and 466 V respectively.

In Parts **c**-**e** the DC bias starts relatively close to or above its steady state value. Because power is not going into the DC bias build up, the fundamental frequency voltage builds up quickly ($\approx$4 μs instead of $\approx$10 μs or 15 μs). This is approximately the same as the simulation in Figure 3.2 Part **b** which did not take into account DC bias build up. The lower value of C_{DC} in Part **a** allows the bias voltage and therefore the fundamental frequency voltage to rise faster than in Part **b**. In all cases the DC bias configuration has little effect on the decay of the fundamental frequency voltage, which decays like that in the simulation. The power required to build up the DC bias can be found using

$$P_{DCbuildup} = I_{DC} V_{DC}, \tag{3.5}$$

where the DC bias current was found using

$$I_{DC} = C_{DC} \frac{dV_{DC}}{dt}. \tag{3.6}$$

Figure 3.4 shows the DC bias build up power for $C_{DC} = 230\ pF$, $1040\ pF$, and $5160\ pF$ while it is ≈zero for the other two DC bias configurations. Note; there is additional power required to maintain the DC bias, and Figure 3.4 only shows the power needed to build it up. However, this is the “extra” power which is diverted from building up the rf amplitudes, causing them to build more slowly.

3.3.2 Harmonic build up

The plasma sheaths are generally considered the main source of harmonic IV. The conduction current through the sheath can often be approximated as a constant ion current with an electron spike around the sheath voltage minimum as was shown in Chapter 2. The ion current is approximately constant in plasmas where the rf frequency (ω) fulfills the inequality $\omega_i << \omega << \omega_e$, where

$$\omega_i = \sqrt{\frac{q^2 n_o}{\epsilon_o M_i}} \tag{3.7}$$

is the plasma ion frequency, and

$$\omega_e = \sqrt{\frac{q^2 n_o}{\epsilon_o M_e}} \tag{3.8}$$

is the plasma electron frequency. In this situation the ions do not react substantially to the rf electric fields, and are accelerated in the sheath by the rf averaged field. This allows the ion current to a surface to be approximated as constant. The electrons respond to the instantaneous electric field, however under normal condition the sheath is always repelling electrons from the surface due to the DC bias and floating potential. The electrons are at relatively high temperature, (a few eV) and when the voltage is small, high energy electrons can escape to the surface. Therefore the electron current can be approximated as a spike centered around the minimum sheath voltage. The displacement current is proportional to the sheath width and sheath voltage slope as shown in Equation 2.26 and redisplayed here;

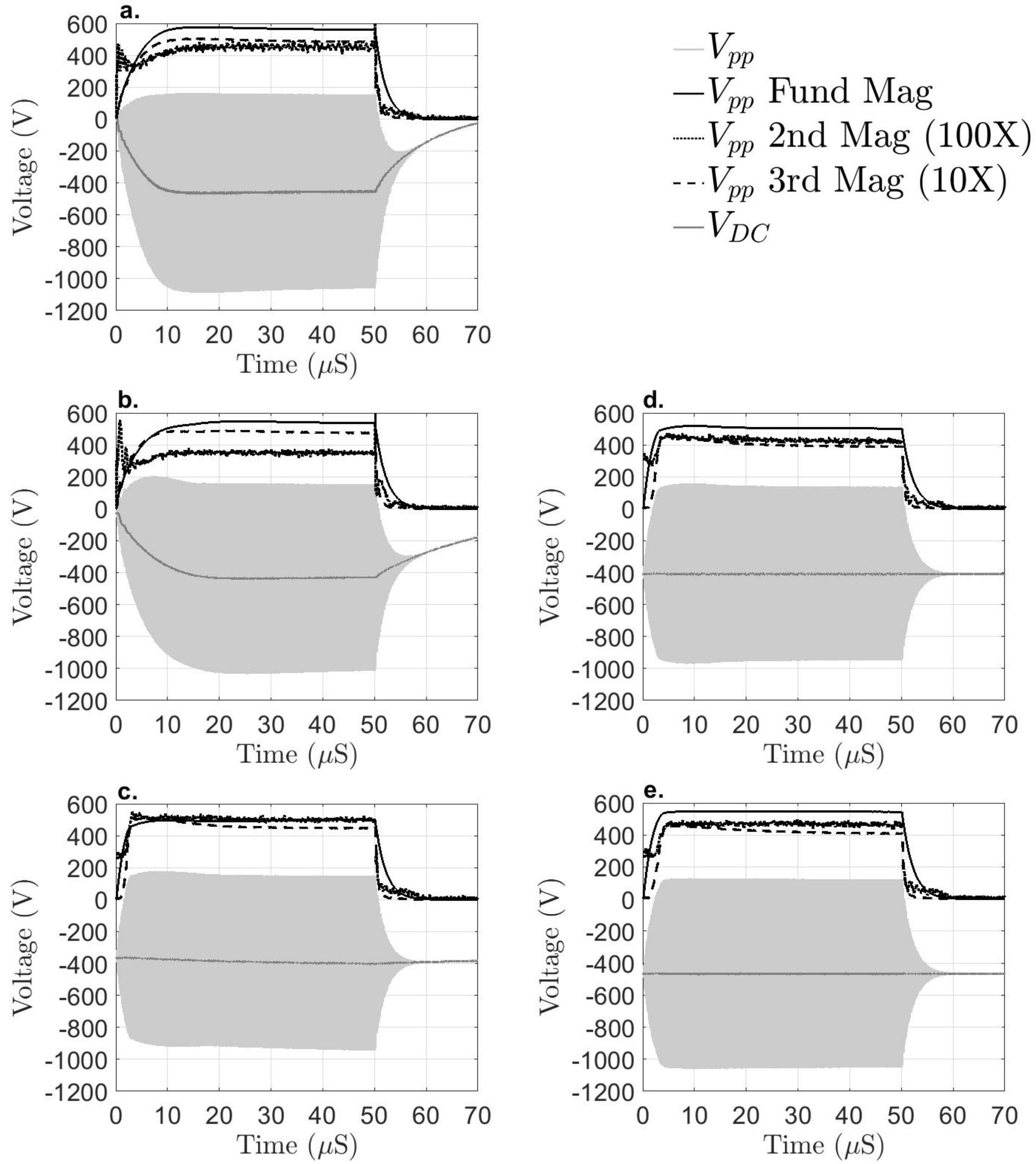

Figure 3.3. Measured total, fundamental, 2nd, 3rd harmonic frequency magnitude, and DC bias voltage in Various DC bias configurations. Part **a** Ar-C_{DC} = 230 pF-Square Wave. Part **b** Ar-C_{DC} = 1040 pF-Square Wave. Part **c** Ar-C_{DC} = 5160 pF-Square Wave. Part **d** Ar-C_{DC} =DC PWR Cap-Square Wave. Part **e** Ar-DC PWR On-Square Wave. 75 mTorr, Ar, 10 kHz 50% duty cycle square wave pulsed plasma.

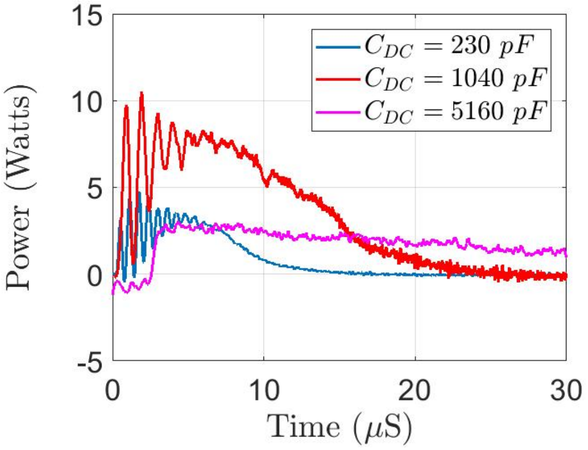

Figure 3.4. Measured power going into building up the DC Bias for differing C_{DC} configurations. 75 mTorr, Ar, 10 kHz 50% duty cycle square wave pulsed plasma.

$$I_{dis} \propto \frac{1}{s(t)}\frac{dV}{dt}. \tag{3.9}$$

The combination of varying sheath width and non-sinusoidal shape of the sheath voltage result in harmonic IV. Since the harmonics depend on the sheath, their build up in pulsed power plasmas depend on the rf and DC magnitudes, as can be seen in Figure 3.3.

The second harmonic voltage builds up to an intermediate value quickly in all DC bias configurations. However the second harmonic voltage is a small signal that is magnified 100X so that it can be viewed in the figures. The quick build up when power is applied might be an artifact of the FFT. However this issue is avoided when looking at the current magnitudes (Figure 3.5). There is a chamber-plasma series resonance near the second harmonic frequency for both the powered (shown in Figure 2.4) and grounded electrode circuits, causing relatively large current and small voltage at that frequency. It can be seen in Figure 3.5 that the second harmonic current, like the third, builds up once a ratio of maximum rf to DC voltage is reached. This is not surprising as once the rf voltage maximum is large enough compared with the DC voltage both causes of harmonic formation start. Higher than normal

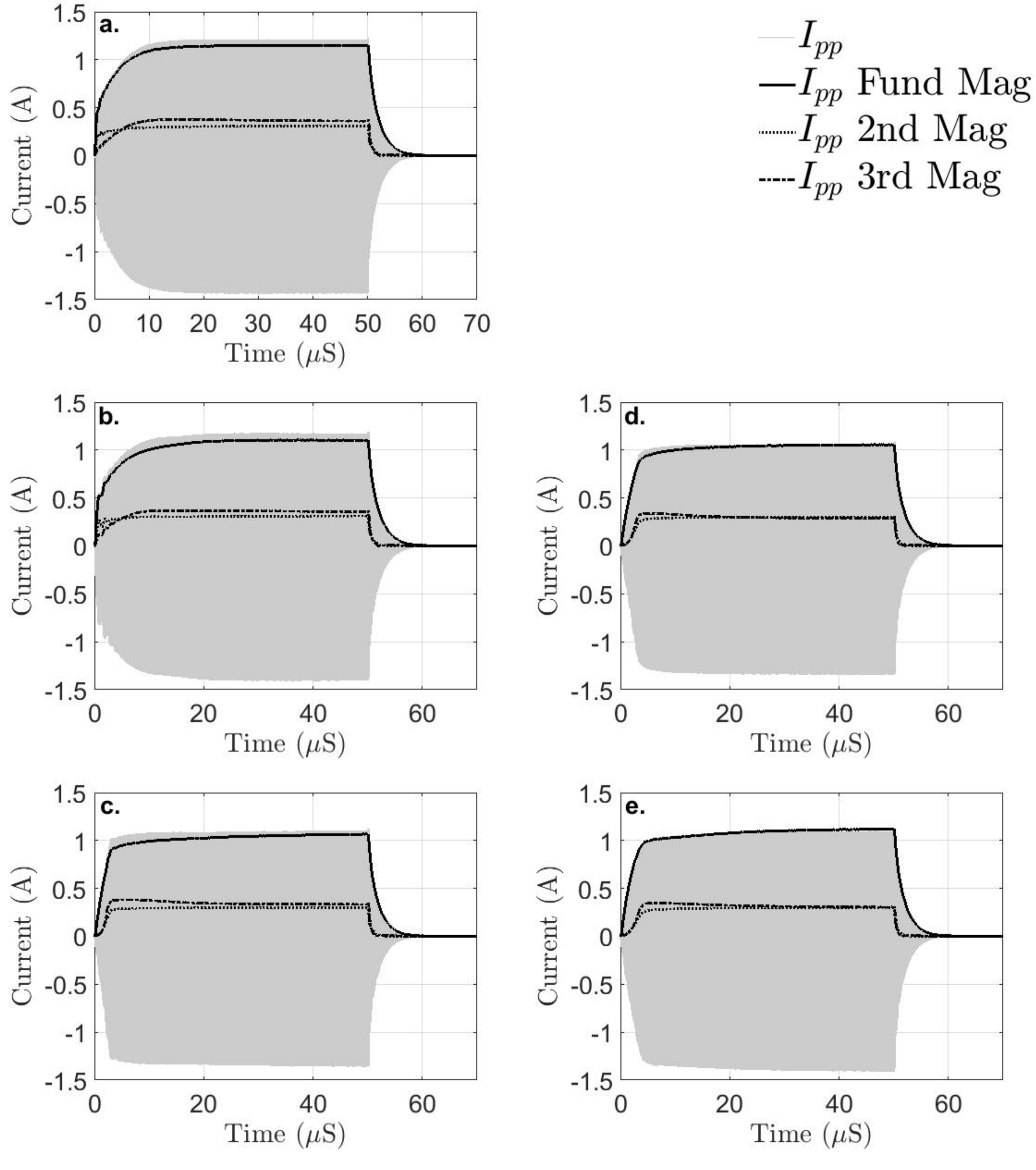

Figure 3.5. Measured total, fundamental, 2nd, 3rd harmonic frequency magnitude current in Various DC bias configurations. Part **a** Ar-C_{DC} = 230 pF-Square Wave. Part **a** Ar-C_{DC} = 1040 pF-Square Wave. Part **a** Ar-C_{DC} = 5160 pF-Square Wave. Part **a** Ar-C_{DC} =DC PWR Cap-Square Wave. Part **a** Ar-DC PWR On-Square Wave. 75 mTorr, Ar, 10 kHz 50% duty cycle square wave pulsed plasma.

harmonic inducing electron current is flowing through the sheath, building up the DC bias. In conjunction, as the rf builds, so do the sheath oscillations, increasing the non-sinusoidal sheath voltage and resulting current. Therefore, it is only when the rf voltage becomes large enough in comparison to the DC bias ($\frac{DC}{rf} \approx 0.8$) that the harmonics build up.

Finally, during the first few μs of Figure 3.3 Parts **a** and **b**, it can be seen that the harmonics do not build up smoothly. Figure 3.6 shows the first 5 μs of power start up with $C_{DC} \approx 1040\, pF$ (Figures 3.3 and 3.5 Part **b**) of the DC bias (Part **a**), plasma reactance (Part **b**), Plasma resistance (Part **c**), rf voltage magnitudes (Part **d**), and rf current magnitudes (Part **e**). As can be seen the DC bias does not build up smoothly. This is due to the circuit response to an abrupt change in current, causing oscillations. The oscillations cause the sheath to thicken and thin, affecting other measured parameters. The oscillations observed in the resistance and reactance can be understood using a plasma impedance model. A basic plasma impedance model is a series capacitor and resistance, where reactance corresponds to the sheath capacitance, and the resistance corresponds to power absorbing processes such as thermalization, excitation, ionization, and collisions between charged particles and chamber surfaces. Then the minimum reactance magnitude (closest to zero) occurs when the sheath is thinnest. During these periods, the sheath voltage will be minimized allowing for a greater number of electrons to reach the surface, which can be seen as the more rapid increase in DC bias voltage. The resistance also increases during this period, due to an increase in electron collisions, due to collisions with the electrode surface. The IV harmonic frequency magnitudes also increase in these periods as their creation mechanisms increase. The fundamental frequency voltage magnitudes show the opposite effect. This is because fundamental frequency power is flowing into the more rapid rise of both the DC bias and harmonic frequencies. With an understanding of the rf, DC bias, and impedance build up, two plasma processing issues can be addressed. First, through an increase in rf amplifier output power leads to a reduction in the unmatched portion of the pulse cycle (Section 3.4). Second, a process window to reduce etch feature charging is introduced (Section 3.6).

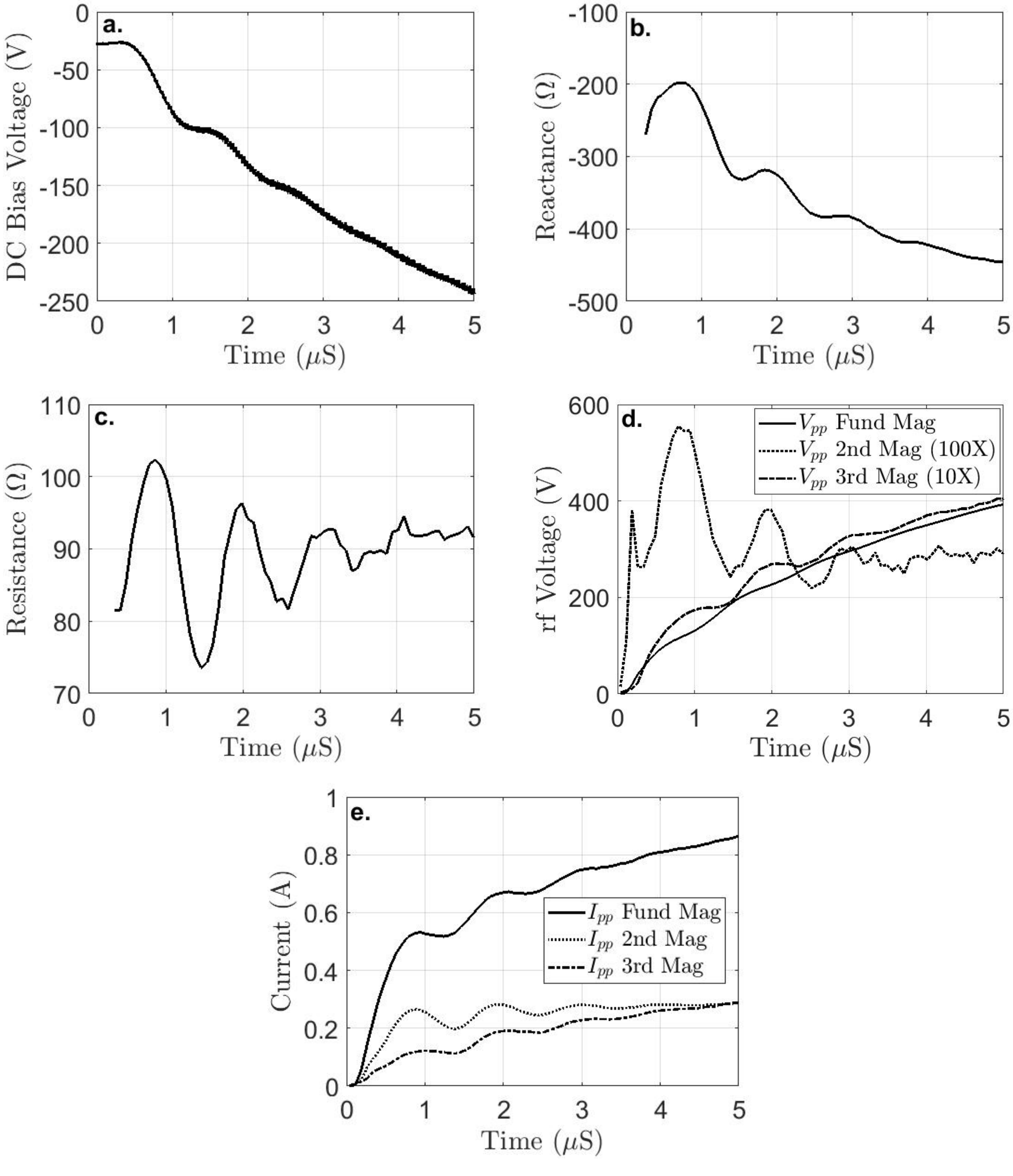

Figure 3.6. Measurements of the first $5 \mu s$ of an Ar-$C_{DC} = 1040\ pF$-Square Wave plasma (Part **b** of Figures 3.3 and 3.5). Part **a** DC bias voltage, Part **b** plasma series input reactance, Part **c** plasma series input resistance, Part **d** Total, fundamental, 2nd, 3rd harmonic frequency magnitude voltage, and Part **e** Total, fundamental, 2nd, 3rd harmonic frequency magnitude current. 75 mTorr, Ar, 10 kHz 50% duty cycle square wave pulsed plasma.

3.4 Impedance and Matching

One of the technical challenges of pulsed plasma processing is impedance matching. The match network is set so that the match-chamber parasitic-plasma impedance is equal to that of the power supply. This minimizes reflected power due to an impedance mismatch, which is associated with process defects (Banna et al., 2012). However, as can be seen in Figure 3.7 the reactance and resistance can change dramatically over a pulse cycle. When $C_{DC} = 230$ or 1040 pF the reactance magnitude starts small and increases with the DC Bias. In the other cases, the DC bias starts close to or at its final value and the reactance magnitude starts large. In all cases, when the power is turned off, the reactance magnitude is seen to increase. As the rf voltage decreases, electrons are no longer brought back into the sheath, and the time average sheath width increases. In the 230 or 1040 pF DC capacitance configurations the resistance starts close to its steady state value. However in configurations where the DC bias is large the resistance starts very high and rapidly falls. This behavior is not yet understood.

Comparing the reactance and impedance to the DC bias and rf voltage, it is clear that the impedance steady state is reached when the voltages are fully built up. A method to reduce the unmatched period in a power pulse cycle, is to quickly build up the voltage. This can be achieved by changing the input power pulse envelope shape. Figures 3.8 and 3.9 show the experimentally measured voltage build up for several C_{DC} configurations using both square wave, and shaped wave amplitude modulation envelopes (shown in blue). The shaped waves are made to build up the fundamental rf frequency magnitude to its steady state as quickly as possible within the limits of the power amplifier. As can be seen, by adding extra power at the start of the pulse cycle, the voltage can be built up relatively quickly (1-2 μs vs 4-10 μs). By building up the rf voltage faster, the DC bias voltage also increases more quickly. Figure 3.10 shows the resistance and reactance for square and shaped inputs. As can be seen, the time to reach the impedance steady state can be reduced using

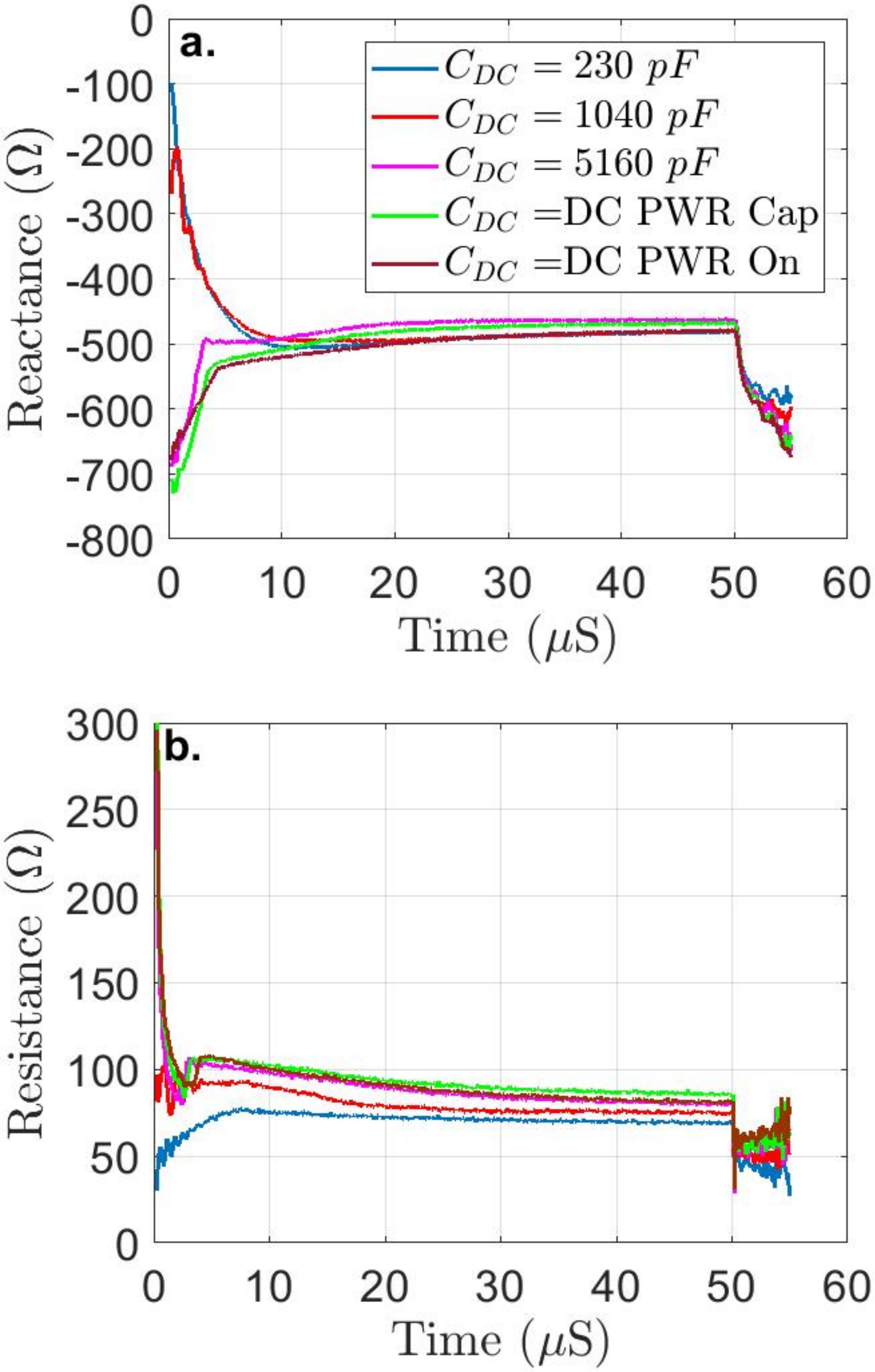

Figure 3.7. Measured plasma input reactance (Part **a**) and resistance (Part **b**) with various DC bias circuits. 75 mTorr, Ar, 10 kHz 50% duty cycle square wave pulsed plasma.

the shaped waves. The exception to this is oscillations in the shaped wave resistance and reactance when $C_{DC} = 230\,pF$ continue past the period when steady state is reached for the square wave. These oscillations are due to the DC bias measurement circuit elements and can be avoided through circuit design. The reduction in the unmatched period was limited in these experiments by the maximum power of the rf amplifier, and relatively simple DC bias build up control. More powerful rf amplifiers can bring the rf voltage to its steady state value faster, while more precise active control of the DC bias would allow it to be ramped up to its steady state value using an external source. Additionally, externally sourcing the power for the DC bias would further allow the rf voltage to ramp up faster.

3.5 Electronegative Plasma

The Previous discussion has been on electropositive plasmas. In electronegative gases both electrons and negative ions are negative charge carriers. The negative ions, like the positive ions, are far more massive and are at much lower temperature than the electrons. This reduces their mobility far below that of the electrons. In regions with large negative ion populations, lower mobility has been shown to induce electric fields which accelerate electrons in the direction of surfaces. This has been seen as a heating mode referred to as "Drift Ambipolar Diffusion" or DA (Bruneau et al., 2015). In CW plasmas, the ion's low mobility causes them to congregate in the plasma center, with an electron dominated electropositive region between them and the plasma sheaths. Therefore the DA electric fields are separate from the sheaths and the sheaths retain their electron repelling characteristic.

3.6 Etch Feature Neutralization

One advantage of using pulsed plasmas in etch processing, is feature charge neutralization. Due to the sheath electric fields, the positive ions velocity is predominantly normal to the surface. This is very important to plasma etching as it allows the ions to strike the bottom

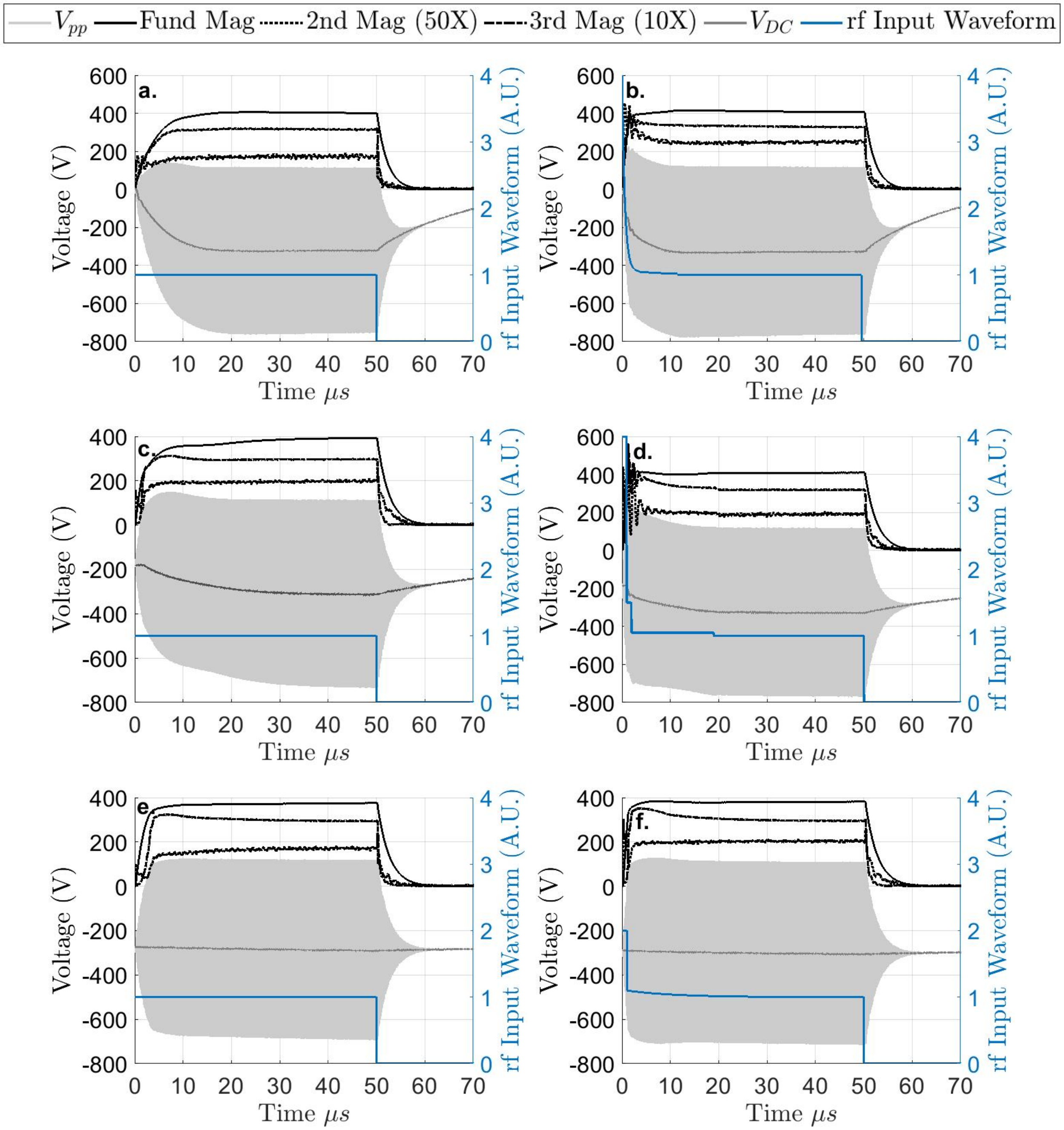

Figure 3.8. Measured total, fundamental, 2nd, 3rd harmonic frequency magnitude, and DC bias voltage in Various DC bias configurations and amplitude modulation envelope shapes. Part **a** Ar-C_{DC} = 230 pF-Square Wave. Part **b** Ar-C_{DC} = 230 pF-Shaped Wave. Part **c** Ar-C_{DC} = 2160 pF-Square Wave. Part **d** Ar-C_{DC} = 2160 pF-Shaped Wave. Part **e** Ar-C_{DC} = 5160 pF-Square Wave. Part **f** Ar-C_{DC} = 5160 pF-Shaped Wave. 75 mTorr, Ar, 10 kHz 50% duty cycle square wave pulsed plasma.

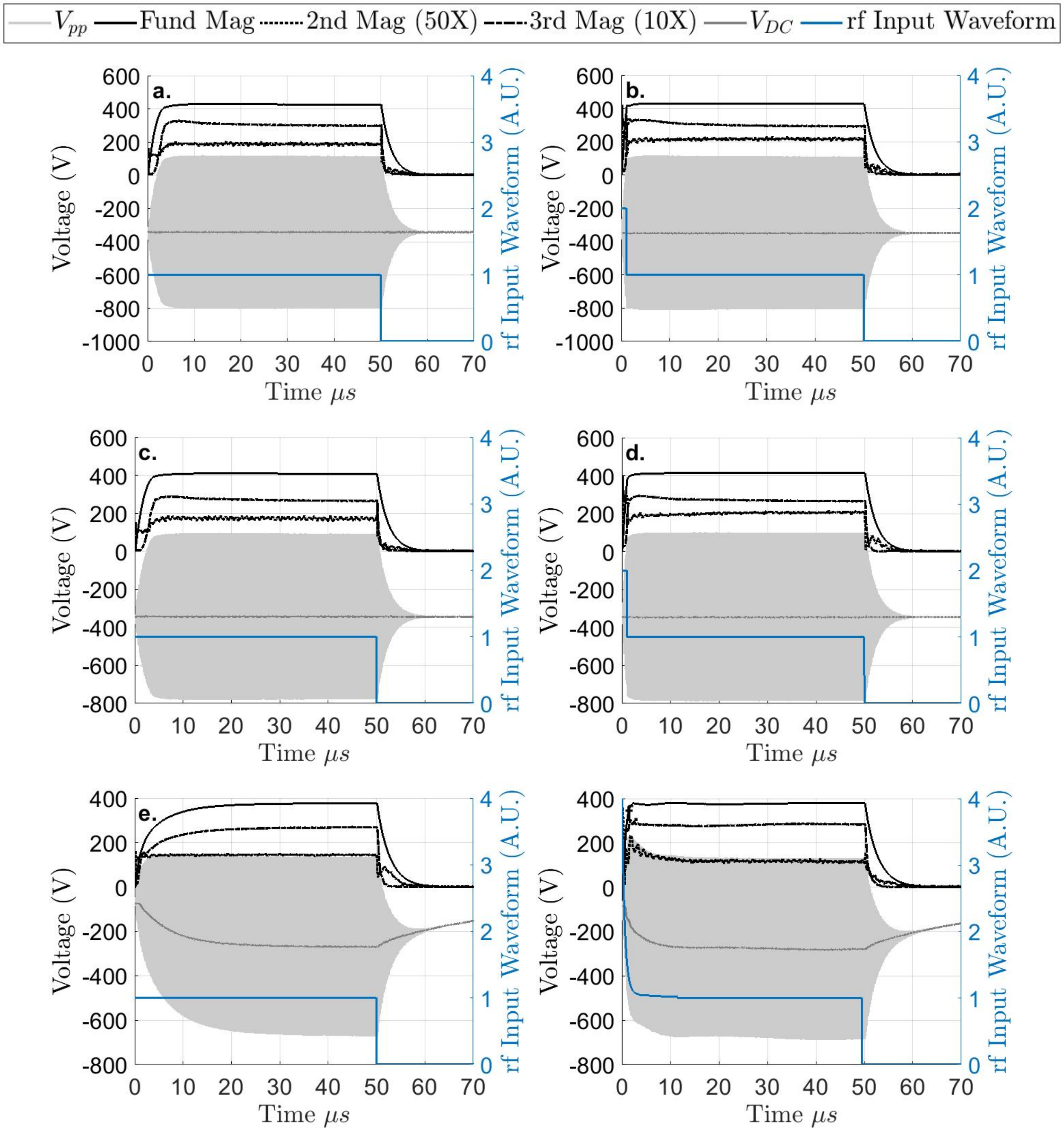

Figure 3.9. Measured total, fundamental, 2nd, 3rd harmonic frequency magnitude, and DC bias voltage in Various DC bias configurations and amplitude modulation envelope shapes. Part **a** Ar-C_{DC} =DC PWR Cap-Square Wave. Part **b** Ar-C_{DC} =DC PWR Cap-Shaped Wave. Part **c** Ar-DC PWR On-Square Wave. Part **d** Ar-DC PWR On-Shaped Wave. Part **e** Ar CF4-C_{DC} = 230 pF-Square Wave. Part **f** Ar CF4-C_{DC} = 230 pF-Shaped Wave. 75 mTorr, Ar (50/50 Ar CF4 in Parts **e** and **f**), 10 kHz 50% duty cycle square wave pulsed plasma.

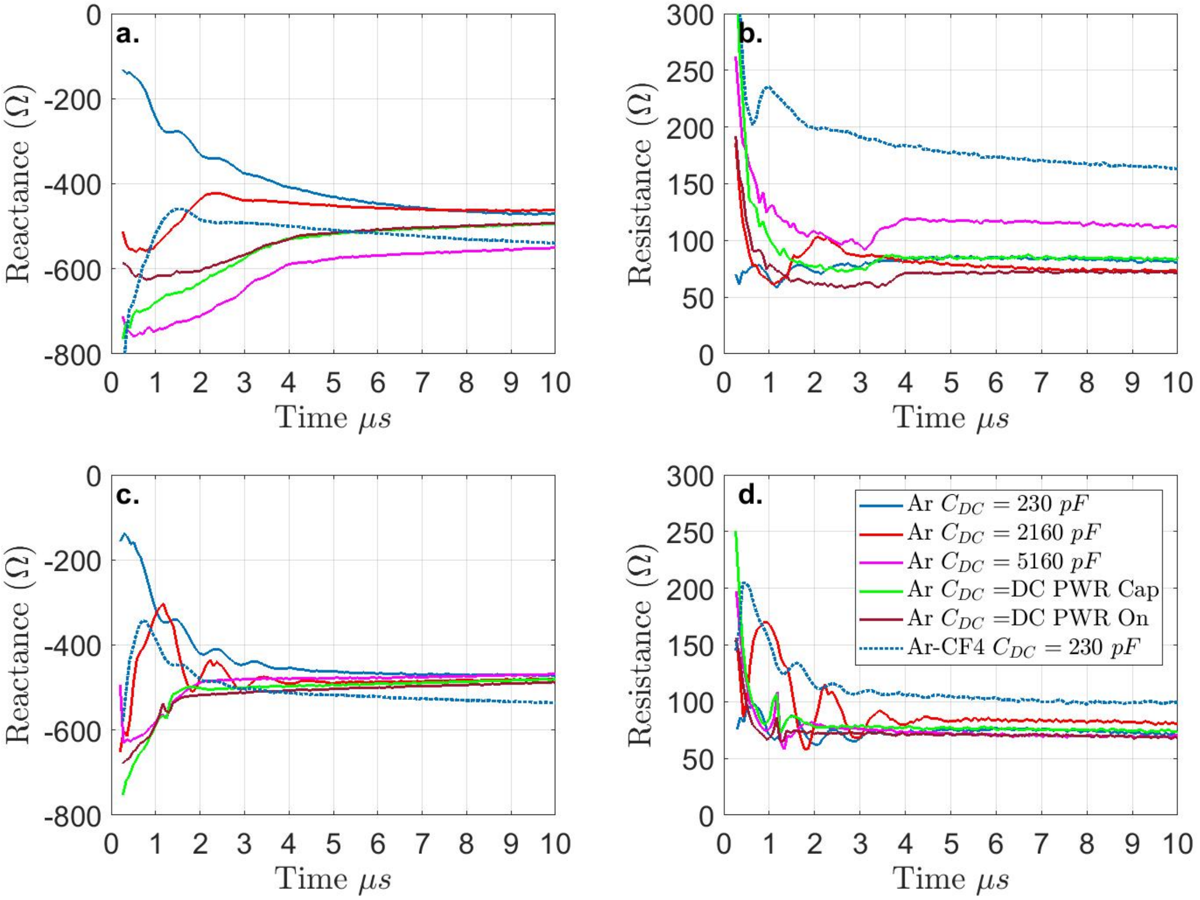

Figure 3.10. Measured square wave modulated Plasma input reactance (Part **a**) and resistance (Part **b**) vs shaped wave modulated reactance (Part **c**) and resistance (Part **d**) with various DC bias circuits and gases. 75 mTorr, Ar or 50/50 Ar CF4, 10 kHz 50% duty cycle square wave pulsed plasma.

of etch features, dramatically increasing the etch rate there. Because the sheath is electron repelling, the isotropic electron angular distribution is maintained throughout the sheath. These are shown in the top portion of Figure 3.11. However this can allow charge build up in insulated etch feature surfaces, which deflect incoming ions causing undesired etch shapes. This is shown in the bottom of Figure 3.11, where ions which have reached the dielectric etch stop charge the feature bottom, while electrons charge the top layer photoresist or dielectric

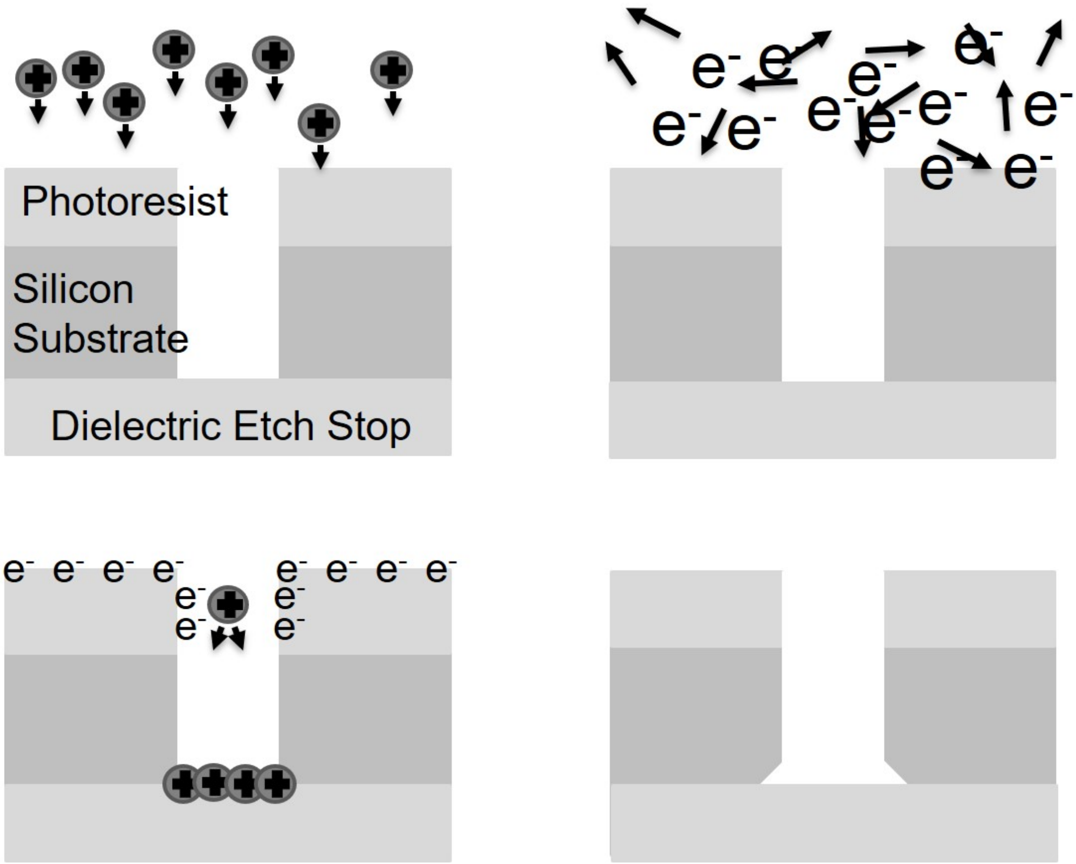

Figure 3.11. Simple trench diagram including anisotropic ion and isotropic electron velocity distribution, the resulting feature charging and an example of formed etch defects.

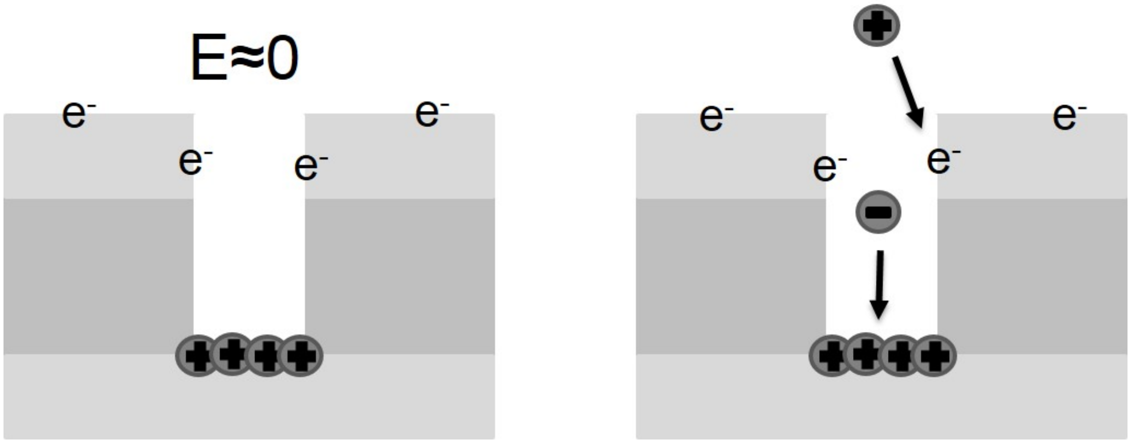

Figure 3.12. Feature charging after sheath collapse.

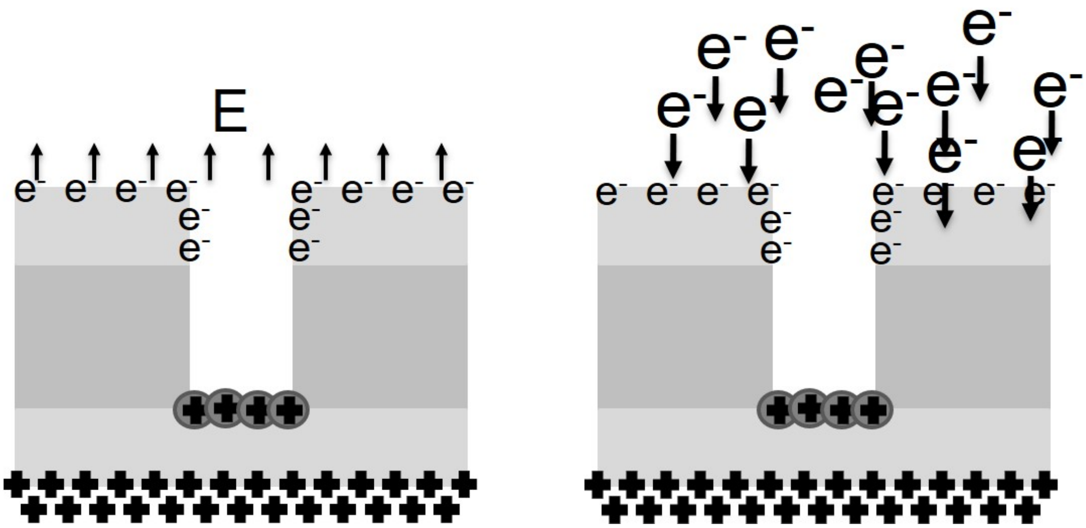

Figure 3.13. Electric field and electron velocity distribution during sheath reversal.

etch mask. This issue can be alleviated during the power off time of an electronegative pulsed plasma.

There are two commonly discussed surface neutralization mechanisms. When the power is turned off the electrons which have a higher mobility and close proximity to chamber surfaces will escape before negative ions which are primarily in the plasma center. If the off time is long enough, electron density becomes much less than negative ion density and an ion-ion plasma forms. Because the negative ions mass is the same order of magnitude as the positive ions mass, their mobilities are similar and a sheath is not necessary to ensure equal negative and positive charge flux to a surface. Then negative ions can diffuse to the surface, interact with the local etch feature electric field, accelerate towards positive space charge, and neutralize it (Overzet et al., 1989; Malyshev et al., 1999; Kanakasabapathy et al., 2001; Banna et al., 2012). A second method is low energy positive ions which are no longer accelerated by a large sheath can neutralize areas of local negative charge (Hwang and Giapis, 1998). Both of these neutralization methods are shown in Figure 3.12. However, for these mechanisms to work, the sheath must mostly or fully collapse. This includes the

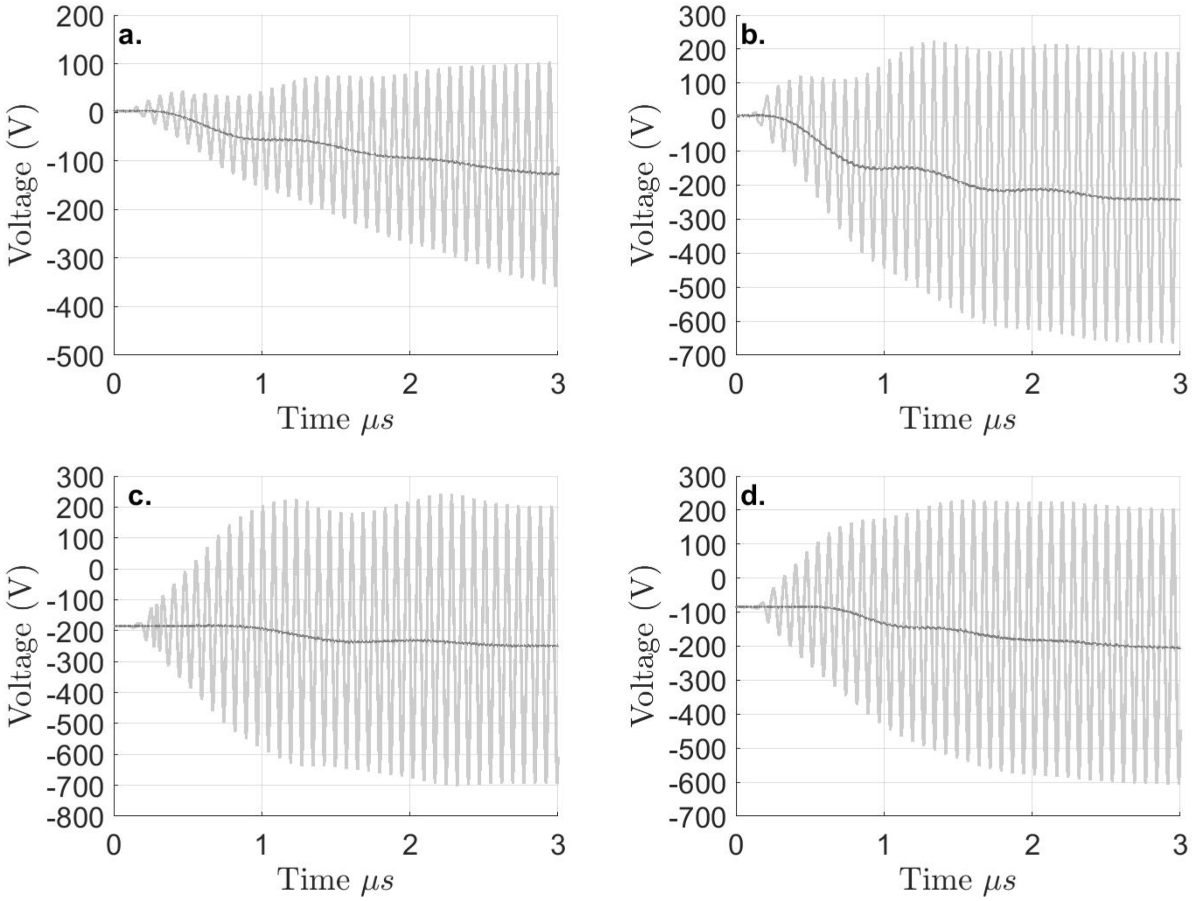

Figure 3.14. Measured total and DC bias voltage during first 3 μs. Part **a** Ar-$C_{DC} = 230\ pF$-Square Wave (from Figure 3.8 Part **a**). Part **b** Ar-$C_{DC} = 230\ pF$-Shaped Wave (from Figure 3.8 Part **b**). Part **c** Ar-$C_{DC} = 2160\ pF$-Shaped Wave (from Figure 3.8 Part **d**). Part **d** Ar CF4-$C_{DC} = 230\ pF$-Shaped Wave (from Figure 3.9 Part **f**). 75 mTorr, Ar or 50/50 Ar CF4, 10 kHz 50% duty cycle square wave pulsed plasma.

full decay of the DC bias which is circuit dependent, and an ion-ion plasma to form in the negative ion neutralization method, the timing of which is highly dependent on gas mixture (Overzet et al., 1997; Subramonium and Kushner, 2002; Banna et al., 2012).

A third charge neutralization method, which can operate in situations where the DC bias has not fully decayed, or a fully ion-ion plasma has not formed, can be achieved through sheath reversal. If the sheath electric field reverses, becoming electron attracting for a short period of time during the rf cycle, electrons will be accelerated towards the surface and have an angular distribution similar to that of the ions, as shown in the bottom of Figure 3.13. This would allow them to reach the etch feature bottoms and perform charge neutralization.

To reverse the sheath, the maximum positive rf voltage at the powered surface must be larger than the addition of the DC bias and V_p magnitudes. To rapidly raise the rf voltage while maintaining similar conditions once the plasma reaches steady state, the shaped amplitude modulation shown on the right side of Figures 3.8 and 3.9 can be used. The DC bias can be controlled passively through the DC bias capacitance value, or actively with a power supply. Finally the build up of V_p can be controlled through gas mixture, as the overall negative charge mobility decreases with increasing negative ion/electron density ratio.

Figure 3.14, shows the voltage build up in four different conditions. It is worth noting the voltage when the DC bias starts to charge, as this is the point when Γ_e becomes non-negligible and V_p begins to rise significantly. In Part **a** (first 3 μs of Figure 3.8 Part **a**, Ar, $C_{DC} = 230\ pF$, Square Wave) the DC bias starts to build up as soon as the maximum voltage becomes $\approx 34\ V$ positive. This is not much larger than the off time value of V_p ($24\ V$ measured by Langmuir probe). The high mobility of the electrons, and increase in T_e, allows V_p to rapidly rise 10 or more volts. Therefore the sheath is expected to remain electron repelling. In Part **b** (first 3 μs of Figure 3.8 Part **b**, Ar, $C_{DC} = 230\ pF$, Shaped Wave) the maximum voltage becomes $\approx 91\ V$ positive. The DC bias is also seen to rise rapidly compared to Part **a**. This requires an increase in electrons reaching the surface, indicating that the sheath thins or briefly inverts.

In Part **c** (first 3 μs of Figure 3.8 Part **d**, Ar, $C_{DC} = 2160\ pF$, Shaped Wave) the maximum voltage becomes $\approx 170\ V$ positive, while the DC bias is $\approx -185\ V$. Because of the large C_{DC} value, the DC bias does not rise as quickly as in Part b, however the current to the electrode is similar. Finally in Part **d** (Ar-CF4, $C_{DC} = 230\ pF$, Shaped Wave) the DC bias starts to build up when the maximum voltage becomes $\approx 132\ V$ positive, while the DC bias is $\approx -85\ V$. Once the DC bias starts to build up it is slower than in Part **b** indicating lower electron density and mobility as expected in an electronegative plasma. This is the most likely case for sheath inversion as the low electron mobility is more likely to allow local electric fields which accelerate electrons towards surfaces as seen in DA heating, and slower V_p rise. The combination of DC bias and rf voltage build up control, in conjunction with gas mixture allows process control to increase or decrease the amount and duration of any sheath inversion. Since in both Parts **c** and **d**, the DC bias does not decay to zero in the off time, the DC bias, rf voltage ratio $(\frac{DC}{rf})$ can be found at the point before the DC bias starts to change. In Part **c** the ratio is 0.50, while in Part **d** it is 0.39. Their steady state ratios are 0.73 and 0.68 respectively. A power sweep performed in 75 mTorr, Ar CW plasmas resulted in ratios between 0.62 and 0.77. The high rf voltage compared to DC bias at a point when the DC bias is not changing indicating low electron collection and little change in V_p gives strong indication that the powered electrode sheath inverts. As mentioned at the end of Section 3.4, active control of the DC bias can be used to ramp it up faster reducing the time to reach steady state. Active control of the DC bias could also be used in the opposite manner to increase the period over which the rf is larger than the addition of the DC bias and V_p, allowing more sheath reversals. This understanding of pulsed plasma power build up and control gives process engineers a powerful tool to find processing windows which can help reduce charging effects.

3.7 Conclusion

An understanding of the transient build up of the voltage across the plasma sheds light on two important plasma processing issues. First, by setting the matching network to be properly matched in the steady state and ramping up the rf voltage quickly, the unmatched period of a pulse cycle can be reduced. In our system, the reduction was from 4-5 μs to 1-3 μs, however with increased active control of the DC bias voltage and more powerful rf amplifiers, this could be reduced further. The reduction in matching time can become more important as the pulse frequency increases. At 100 kHz, the pulse cycle is only 10 μs long and a few μs is a large portion of the power on time. Second, an understanding of the voltage build up gives insight into a charge neutralization process window that can be exploited by process engineers. The value of these conclusions is further increased as they only require changes to the power delivery system, and not the chamber.

CHAPTER 4

LANGMUIR PROBE (LP) MEASUREMENTS IN PULSED POWER PLASMAS

4.1 Abstract

In transient plasmas, applied power can couple to the plasma differently than in continuous wave plasmas, causing changes in the electron temperature or energy distribution function. This has primarily been measured using Langmuir probes (LPs). However the LP measured current can be distorted by both displacement current and probe circuitry. These distortions, especially in the case of probe circuitry, can cause false measurement of temperature spikes, or overestimate their magnitude, as well as change the measured shape of the energy distribution function. Plasma density can also be incorrectly calculated under these circumstances. Therefore these effects must be understood when interpreting LP measurements taken in transient plasmas.

4.2 Introduction

Langmuir probes (LPs) are a cornerstone plasma diagnostic which is used to determine the plasma parameters; plasma potential (V_p), density (n), and electron temperature (T_e), or energy distribution function (EEDF). LPs have been used as a plasma diagnostic since the 1920s (Mott-Smith and Langmuir, 1926). At its most basic, an LP is a conductor placed into a plasma, connected to an external voltage source and current measurement system. They are operated by placing various bias voltages (V_b) on the conductor, and measuring the resulting current. The current-voltage (IV) curve generated in this way is then related to the plasma parameters. Note; as is tradition for LP data, current due to electron collection is plotted as positive values. All current plots in this Chapter are plotted in this manner, and a negative sign is added to equations with current in them, ensuring consistency. The

IV curve to plasma parameter relation depends on probe geometry and sheath collisionality. Three methods used for varying degrees of collisionality are; for highly collisional plasmas, Allen-Boyd-Reynolds Theory (Allen et al., 1957), for collisionless plasmas, Orbital Motion Limited Theory (Mott-Smith and Langmuir, 1926), and for partially collisional plasmas, a parameterization (Zakrzewski and Kopiczynski, 1974) of Bernstein-Rabinowitz-Laframboise Theory (Bernstein and Rabinowitz, 1959; Laframboise, 1966) can be used. All of these theories require that for a given V_b, the probe tip-plasma sheath ($V_s = V_b - V_p$) does not change in time.

More recently, LPs have been used to measure time-averaged plasma parameters in plasmas that are driven (oscillatory) at well-defined frequencies (Eser et al., 1978; Norström, 1979; Hopkins, 1995). For example, in radio frequency (rf) driven plasmas, V_p oscillates at the rf frequency and its harmonics, causing distortion to measured IV curves (Emeleus and Garscadden, 1962; Boschi and Magistrelli, 1963). The general method to account for V_p rf period oscillations, is to make hardware changes to the LP (Gagné and Cantin, 1972; Paranjpe et al., 1990; Godyak et al., 1992; Sudit and Chen, 1994). First, blocking filters (rf chokes) with high impedance at the rf frequency and some of its harmonics are added between the LP tip and current measurement point, reducing the displacement induced current (I_{dis}), at rf frequencies. Second, plasma-probe tip capacitive coupling is increased through the addition of a parallel capacitance, C_{rf}, to the tip capacitance C_p. These components are shown in Figure 4.1. The total capacitance at rf frequencies C_{probe} is given by

$$C_{probe\quad rf} = C_p + \frac{1}{\frac{1}{C_{rf}} + \frac{1}{C_f}}, \tag{4.1}$$

where C_f is the floating sheath capacitance that forms at electrically floating surfaces. This decreases the rf impedance between the plasma and the LP tip, allowing the potential on the LP tip to match the rf oscillations in V_p. Thus the probe tip-plasma sheath change in time is minimized and the theories mentioned above for DC plasmas can be used.

However, there is still no known method for accurately using LPs in transient plasmas. In such systems, transient fluctuations in Vp will induce I_{dis} which can distort calculated plasma parameters (Liu et al., 2014). Additionally,the interaction between the LP resistive-inductive-capacitive (RLC) components and the abrupt changes in conduction current can cause a large difference between the current collected at the LP tip, and at the current measurement point. This difference can cause large errors in calculated plasma parameters, especially T_e and the EEDF, and to the authors' knowledge has not been addressed in the literature.

When LPs are used in systems that are both transient and oscillatory, such as pulsed rf power plasmas, measurements become even more problematic. For example the hardware components necessary for LP use in rf driven plasmas, increase the capacitance, which increases I_{dis}. Further, the filters restrict the RLC LP circuit values and therefore the current measurement RLC time delay in transient plasmas. Additionally, the effective oscillations in V_p in transient plasmas are at frequencies far below the rf frequency, and the rf filters do not block this current. Adding filters for these frequencies would block the transient conduction current (effectively adding a large RLC time delay), and not allow the LP to function properly. Without the ability to eliminate either effect, experimenters using LPs in transient rf driven plasmas should have an understanding for how their results may be affected. This is the purpose of this chapter.

In section 4.3, the experimental setup of the vacuum chamber and LP are given. Section 4.4 demonstrates the method used to take time resolved LP measurements. Section 4.5 gives some discussion on calculating transient plasma induced I_{dis}. Section 4.6 shows the affect of LP RLC circuit components on IV curves when conduction current to the probe changes abruptly. The following subsection (4.6.1) shows how these effects cause errors in calculated EEDF and T_e. Finally section 4.7 gives some concluding remarks on the importance of understanding the interaction of LP circuitry and transient plasmas when interpreting results, with some discussion on LP design intended to minimize error in the measured IV curves.

4.3 Experimental Setup

The chamber is the mGEC described by Goeckner et al. (Goeckner et al., 2004), with a capacitively coupled source (Poulose et al., 2017). The top powered, and bottom grounded electrodes have diameters of 11.4 cm (4.5 inches) and 15 cm (5.9 inches) respectively. The electrode gap was 6.35 cm (2.5 inches). The Langmuir probe and control box are purchased from Impedans Ltd. Figure 4.2 shows the physical setup of the LP within the chamber. The LP tip is placed at the radial center of the electrodes, 2.54 cm (1 inch) above the grounded electrode, and 3.81 cm (1.5 inches) below the powered electrode. The components of the LP that are immersed in the plasma are shown in Figure 4.1. The rf capacitor is 20 mm long, has an inner radius of 8 mm, and an outer radius of 9.53 mm. The dielectric is Macor with a dielectric constant of ≈6. The LP tip length is 11.9 mm and radius is 0.25 mm. All experimental data was taken in an 13.33 MHz rf driven, 75 mTorr Ar plasma, with the rf power pulsed on and off at 10 kHz with a 50% duty cycle.

4.4 Time Resolved Measurements

The general method to acquire an IV curve using an LP, is to set a V_b, measure the resulting DC current and repeat for various V_b until the IV curve is resolved. For time resolved measurements the process is similar, except now a V_b is set, and the resulting time dependent current is measured over the period of interest. In this way, for a given V_b, the current over a plasma power pulse cycle can be found. To achieve a proper I-V_s relationship, the current measurement time resolution period must be short enough that V_p does not change appreciably during that period. If V_p does change appreciably there is no single value for V_s and the assumptions used in DC LP theory are not valid.

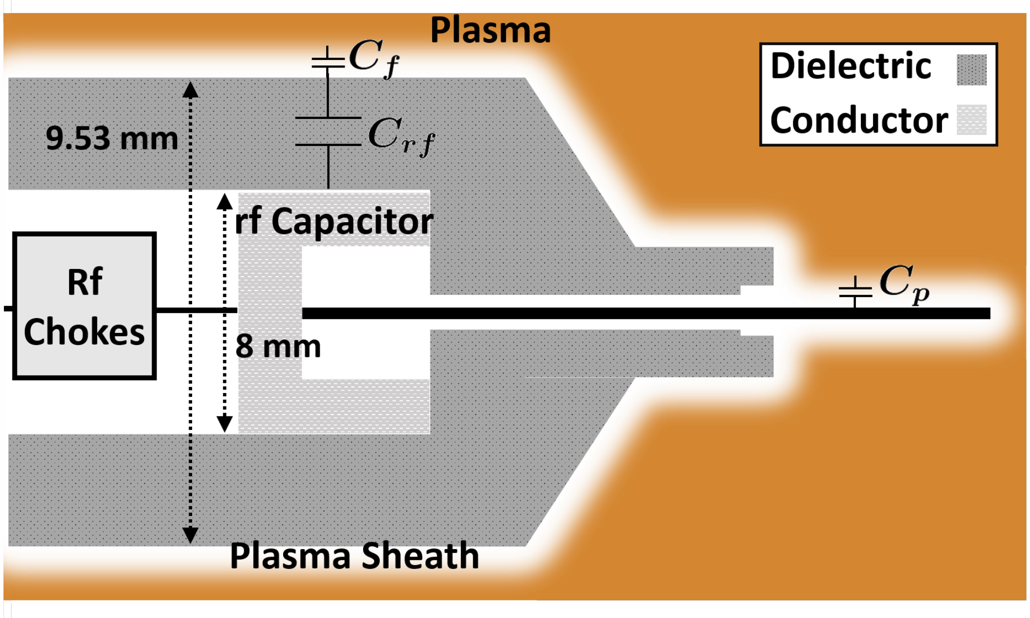

Figure 4.1. LP components (not to scale), with plasma sheath and rf capacitor capacitances.

While often similar to IV curves from continuous wave (CW) plasmas, IV curves from transient plasmas can show marked differences. Figure 4.3 Part **a** shows a non time resolved IV curve taken in a CW plasma with IV curve regions labeled. Part **b** shows time resolved measurements in an rf power pulsed plasma with the same regions labeled.

Noticeable distortion to the IV curve due to I_{dis} and RLC circuit effects are seen, especially after rf power is reapplied ($t = 0 - 20\ \mu s$). Several IV curves from this time period are shown in Part **c**. At $t = 0\ \mu s$, just before the rf power is reapplied, the IV curve is unperturbed. Focusing on the I_{sat} region, the current magnitude increases over three times from $t = 0$ to $t = 5.1\ \mu s$, before becoming positive at $t = 11.1\ \mu s$. These fluctuations are evidence of displacement current induced by fluctuations in V_p and are discussed in detail in Section 4.5. In the e_{col}/e_{sat} region the current goes from positive to negative before settling around the I_{sat} value. This is a result of an increase in V_p causing an abrupt change in current (the move from e_{col}/e_{sat} to I_{sat}) interacting with the LP RLC circuit. Section 4.6 will discuss this in more detail.

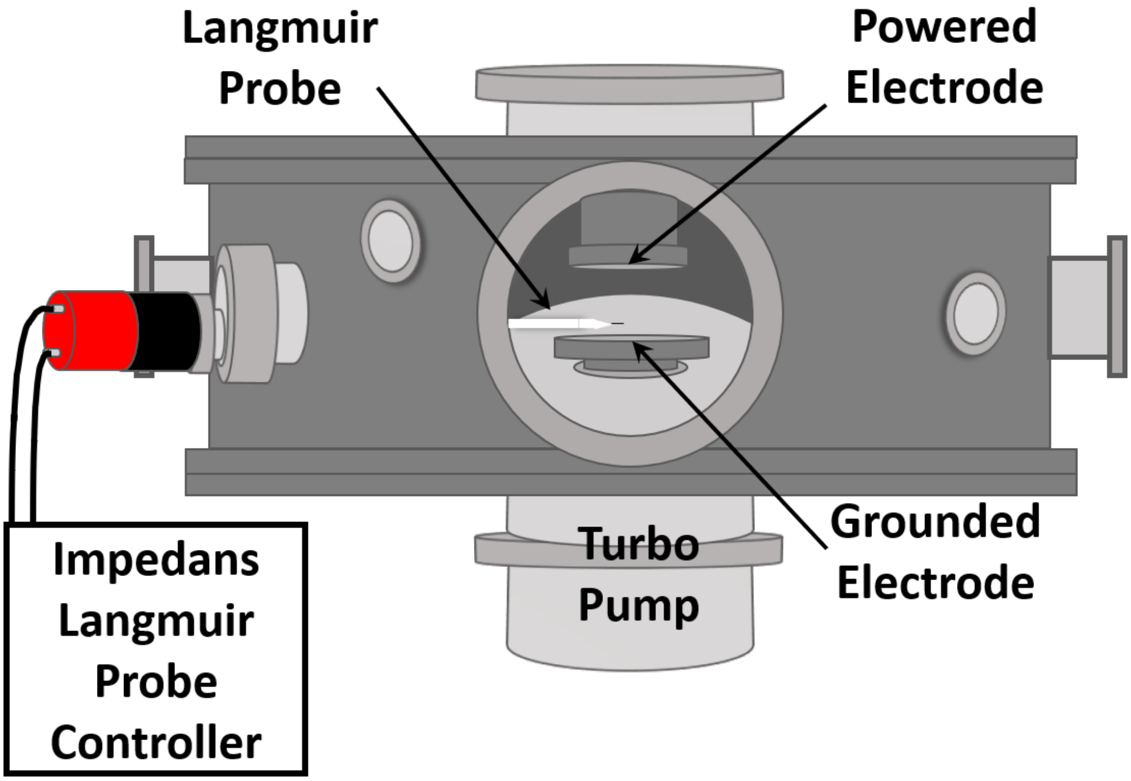

Figure 4.2. mGEC Chamber With Attached Langmuir Probe.

4.5 IV Curve Distortion due to Induced Displacement Current

As V_p fluctuates, displacement current flows through capacitive couplings between the plasma and the LP. The current through any capacitor can be found using;

$$-I_{dis} = \frac{dQ}{dt} = \frac{dCV}{dt} = C\frac{dV}{dt} + V\frac{dC}{dt}, \tag{4.2}$$

where Q is the charge, C is the capacitance, and V the voltage. The rf frequency capacitance of the rf compensated LP shown in Figure 4.1 is given by Equation 4.1; however, for the slower non-rf oscillations of V_p, the positive ions are able to react in time with the oscillations. The result is that the floating sheath no longer acts like a capacitor, and the LP-plasma capacitance is given by

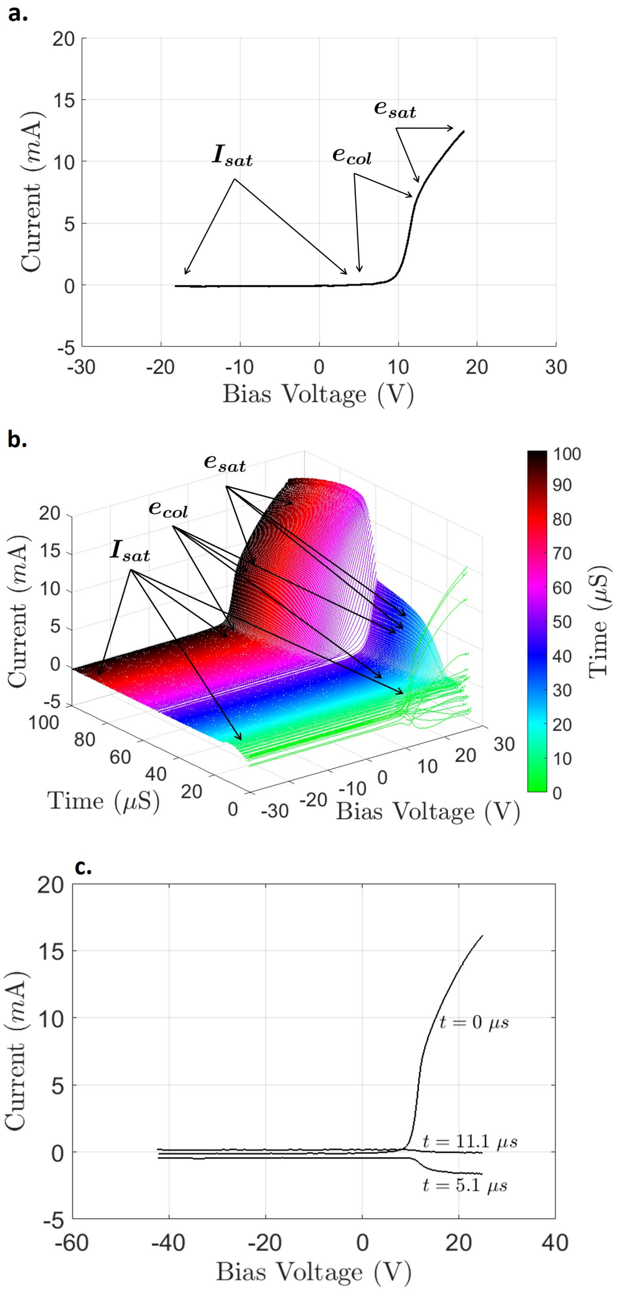

Figure 4.3. 75 mTorr CW argon plasma IV curve (Part **a**). Time resolved IV curves 75 mTorr, Ar, 10 kHz 50% duty cycle square wave pulsed plasma (Parts **b**). Selected time resolved IV curves demonstrating I_{dis} and RLC effects (**c**).

$$C_{LP} = C_p + C_{rf}, \tag{4.3}$$

Where C_p and C_{rf} are defined in Figure 4.1. To quantify I_{dis} to the probe for a given $\frac{dV}{dt}$ both C_p, and C_{rf} must be known. The capacitance of each can be estimated using the infinite cylinder capacitance approximation equation

$$C_{cyl} = \frac{2\pi L k \epsilon_0}{ln(\frac{r_2}{r_1})}, \tag{4.4}$$

where L is the cylinder length, k is the dielectric constant, ϵ_0 is the permittivity of free space, and r_1 and r_2 are the inner and outer radii respectively. Using this equation, C_{rf} is found to be $\approx 38\ pF$ for the system used here.

The outer radius for C_p is set by the sheath width and is therefore a function of the sheath voltage (V_s). The LP tip's sheath width (s_{wp}) dependence on V_s changes in the ion saturation, electron collection and electron saturation regions of the LP IV curve. Because the LP bias voltages in the ion saturation region perturb the power pulsed plasma the least, s_{wp} and C_p will be solved for in that region. In the ion saturation region, s_{wp} depends not only on V_s, but on n, T_e, and ion mobility as well (Rousseau et al., 2005). However s_{wp} can be found using an analytical fit given by David et al. (David et al., 1990), which was developed by Kopiczynki (Kopiczynski, 1977). The fit is given by

$$s_w = r_{she} - r_{sur} = \lambda_D \sqrt{m * (\chi_p + 3.5) - 4} \tag{4.5}$$

where the normalized sheath voltage (χ_p) is given by

$$\chi_p = \frac{qV_s}{k_B T_e}, \tag{4.6}$$

λ_D is the Debye length given by

$$\lambda_D = \sqrt{\frac{\epsilon_0 k_B T_e}{qn}}, \tag{4.7}$$

q is the elementary charge, m is a fit parameter given by

$$m = 0.59 + 1.86 D_{\lambda sur}^{0.47}, \tag{4.8}$$

and $D_{\lambda sur}$ is the Debye number at the surface, with the Debye number for a given radius defined as

$$D_\lambda = \frac{r}{\lambda_D}. \tag{4.9}$$

With expressions for each capacitance found, the theoretical displacement current due to a given V_p can be found using Equation 4.2. The displacement current for this system is then given by

$$-I_{dis} = C_{rf}\frac{dV_s}{dt} + C_p\frac{dV_s}{dt} + V_s\frac{dC_p}{dt}. \tag{4.10}$$

There is no current due to changing C_{rf} as that capacitance is fixed. Setting $\frac{k_b T_e}{q} = 1.5\ V$, and $n_0 = 1 \times 10^{16}\ m^{-3}$, while varying V_s in the same manner that V_p is varied in Figure 4.4 Part **a**, gives I_{dis} during the first 9 μs shown in Figure 4.4 Part **b**. Since the input voltage variation is symmetric, the opposite I_{dis} is found when the voltage is decreasing (50-60 μs), and $I_{dis} = 0$ when the voltage is not changing. C_{rf} is large compared to C_p and so the total displacement current is dominated by that term. The probe tip displacement current is mostly due to the $C\frac{dV}{dt}$ term, however the $V\frac{dC}{dt}$ term is only 3-4 times smaller in magnitude and therefore non negligible in systems where C_{rf} is not $\gg C_p$. As can be seen, the $V\frac{dC}{dt}$ term also works to reduce total displacement current as the dependency of C_p on V_s causes $\frac{dV_s}{dt}$ and $\frac{dC_p}{dt}$ to have opposing signs.

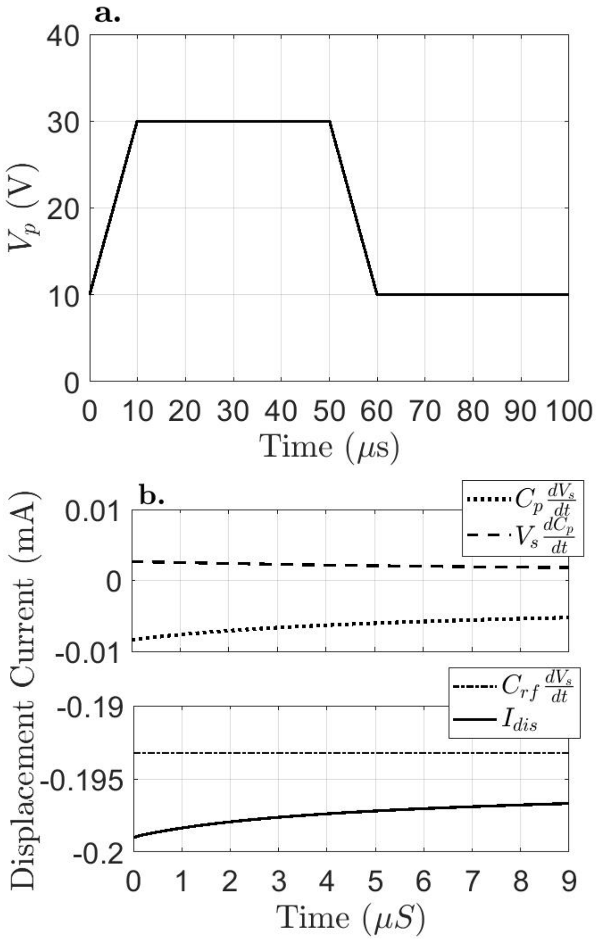

Figure 4.4. Part **a**; time resolved simulation V_p. Part **b**; Calculated LP displacement current from from 0-9 μs.

In comparison, the experimentally measured effects of displacement current on the time resolved IV curves are seen in Parts **b** and **c** of Figure 4.3. Taking only the current measured at $V_b = -20\ V$ results in the solid line shown in Figure 4.5. As can be seen at the beginning of the power pulse, I_{sat} becomes increasingly negative (positive ion collecting) before becoming positive (electron collecting) briefly and returning to its steady state negative value. This can not be explained from conduction current effects only, as in the I_{sat} region the LP collects negligible amounts of electrons, and therefore the current is never positive. However an increasing V_p can explain the negative current maximum, while a decreasing V_p can explain the positive maximums. The negative maximum happens when rf power is applied and V_p rises from its rf power off time value, overshooting its rf power on value. The first positive maximum is due to V_p falling from the maximum overshoot value, to its steady state power on value. Finally the second positive maximum comes when the rf power is turned off and V_p decreases from the steady state rf power on value, to its rf power off value. If V_p is measured over the pulse cycle, I_{dis} can be solved for and compared to measured I_{sat} allowing conduction and displacement current to be separated. To use this method in the e_{col}, and e_{sat} regions of the LP IV curve, solutions for the probe sheaths in those regions must be found. However, in cases where C_{rf} is expected to be $\gg C_p$, a quick estimate can be found using only C_{rf}. Further, the requirement that V_p is known is not always met. In the following subsection, the difficulties in measuring V_p through power transitions, and an estimate of V_p using displacement current will be discussed.

4.5.1 Finding V_p

It is preferable to measure V_p and use that value to calculate I_{dis}, however in many systems this may not be possible. It was found in the system used in this study that V_p could become very large during the power turn on, requiring very high positive voltages to be set on the probe to measure it. Since for time resolved measurements, the voltage is set for a full pulse cycle while the time dependent current is measured, the high V_b necessary to measure V_p during its maximum when rf power is first applied, will be larger than V_p during the rest of the rf power on time, and much larger during the rf power off time. In this condition the LP can collect large amounts of electron current during the rf power off time, changing the electron density and V_p at the start of a power pulse cycle. This change in initial conditions will change the plasma kinetics over the full pulse cycle. Therefore the plasma measured when V_b is set high enough to measure the maximum V_p will be different than the plasma being measured at lower V_b. This results in distorted IV curves that do not represent an unperturbed plasma.

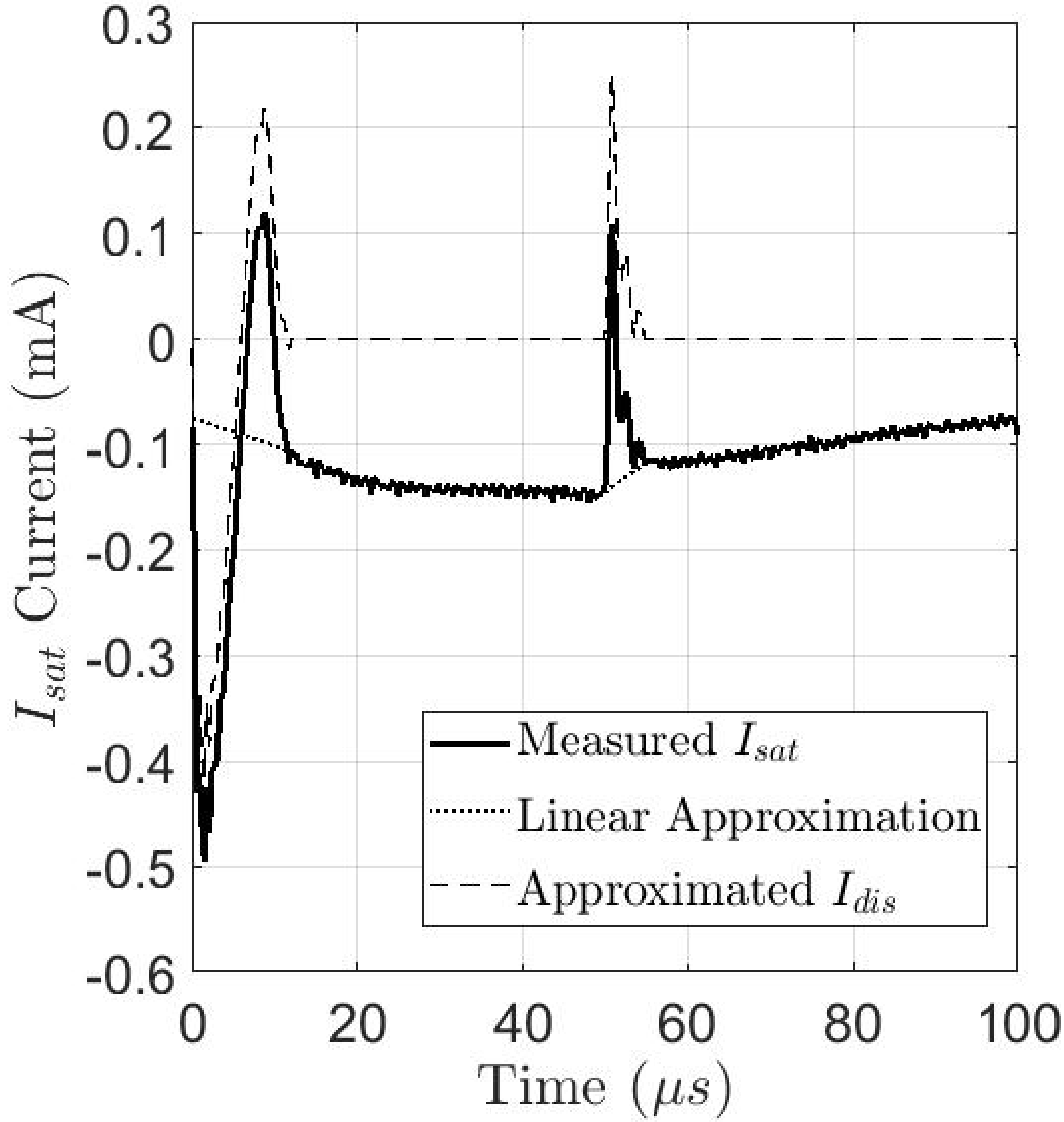

Figure 4.5. Time resolved measured I_{sat} ($V_b = -20\ V$), linear approximation during periods of large displacement current, and approximated displacement current (I_{dis}). 75 mTorr, Ar, 10 kHz 50% duty cycle square wave pulsed plasma.

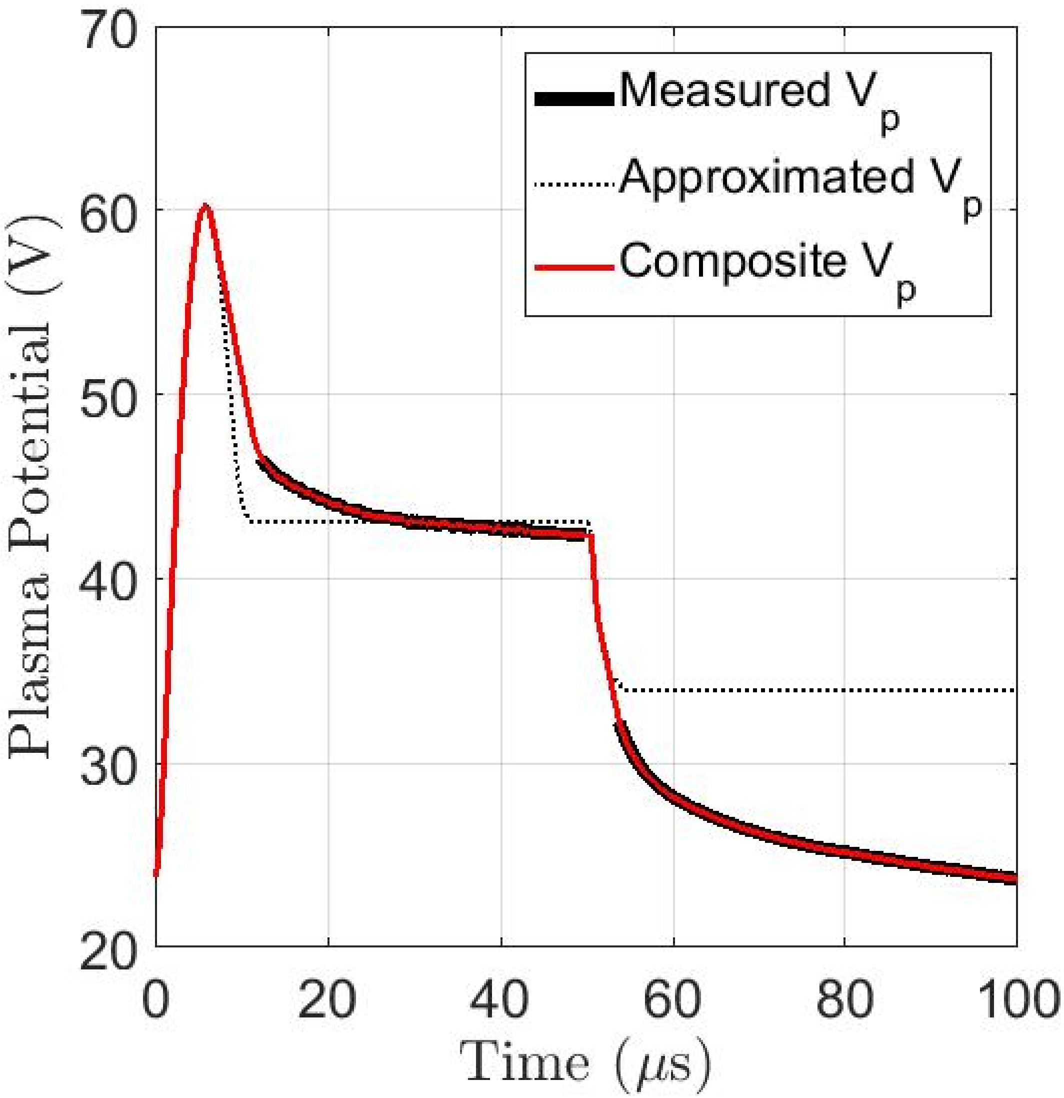

Figure 4.6. Time dependent V_p. 75 mTorr, Ar, 10 kHz 50% duty cycle square wave pulsed plasma.

To get an approximation of V_p during the rf power transitions, the displacement current can be used. The conduction current can be approximated as a line between I_{sat} at the beginning and end of large displacement current effects. The displacement current is then the difference between the measured current and linear approximation as shown in Figure 4.5. Using the approximated displacement current, Equation 4.10 can be rearranged and solved implicitly for V_s. Using this and the initial conditions for V_p just before the rf power turn on, results in the approximated value of V_p shown in Figure 4.6. Also shown are the LP measured values of V_p and a composite of the two. Since the linear approximation is only applied during periods of obvious displacement current, no displacement current is calculated when $\frac{dV_p}{dt}$ is small. However, this happens in the regions where V_p is correctly measured by the probe, and a composite of the two can give reasonable values over a full rf power cycle. The error in calculated V_p during the transition due to the linear assumption of conduction current can be large, as it compounds when the displacement current is integrated to solve Equation 4.10. Therefore the approximated value of V_p should only be seen as qualitative and be used in power transition regions where the displacement current is large compared to the conduction current.

4.6 IV Curve Distortion due to Conduction Current RLC Circuit Effects

In the transition regions of a pulsed power plasma, the IV curve can change quickly (Parts **b** and **c**, Figure 4.3). These changes were most abrupt during the power turn on, causing obvious underdamped RLC circuit oscillations in regions where the current changes from e_{col}/e_{sat} to I_{sat}. Similar effects can sometimes be seen during the rf power turn off, however generally $\frac{dV_p}{dt}$ is smaller during this period, causing the current change to be less abrupt. During the power turn on transition, V_p increases and some V_b values which were in the e_{col} or e_{sat} regions become part of the I_{sat} region until V_p decreases again. These transitions between regions are the cause for abrupt current changes and corresponding RLC circuit effects. The RLC circuit components cause the response to abrupt current changes to be over, under or critically damped, and have a set rise or fall time for the current to reach its unperturbed value.

The IV curves shown in Parts **b** and **c** of Figure 4.3, were the result of an underdamped circuit. To test the RLC effects in the system in other damped conditions, a variable resistor was placed in series, between the LP and measurement box. By increasing the resistance, the LP circuit could be changed from under, to critically, to overdamped. The results are seen in Figure 4.7, where the current in time is measured when $V_b = 25$ V. This value of V_b was chosen because the corresponding current oscillates between the e_{sat} region during the steady state rf power on and off periods, and the I_{sat} region during the rf power turn on transition, showing some RLC effects.

In the underdamped case, when the current change is abrupt enough as it is during the power turn on, the current will overshoot and oscillate at a frequency dependent on the LP RLC circuit. In the over and critically damped cases, the current does not overshoot and oscillate, rather it falls to its steady state value. In the critically damped case, the current reaches its steady state value in the shortest amount of time. There is some oscillation seen in both the over and critically damped cases, however this is attributable to displacement current which was discussed in Section 4.5.

4.6.1 RLC Circuit Effects on T_e and the EEDF Measurements

When the RLC circuit is underdamped, the measured current time resolution is high, and the RLC oscillations are large enough, the measured IV curves are obviously incorrect as indicated in Part **d.**, of Figure 4.3 during the first 10 μS. However, if the time resolution of the measured current is low enough that the oscillations are averaged, or the oscillations are small enough, or the RLC circuit is over or critically damped, the IV curve may not be obviously distorted, but will still cause incorrect calculations of T_e and the EEDF.

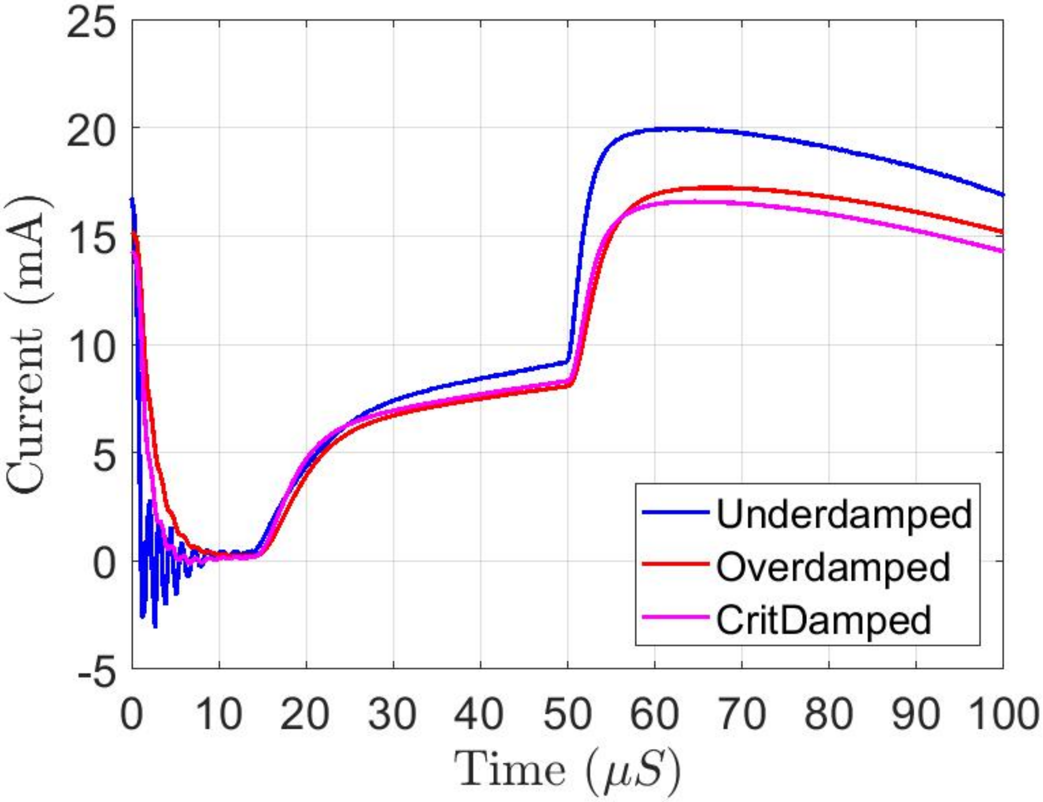

Figure 4.7. Measured time resolved over, under, and critically damped LP current response ($V_b = 25V$). 75 mTorr, Ar, 10 kHz 50% duty cycle square wave pulsed plasma.

To illustrate the issues when calculating the EEDF, it is easiest to look at the second derivative of the IV curve. This is because the second derivative is proportional to the EEDF, and V_p can easily be found visually. Figure 4.8 shows an IV curve and its first and second derivatives. V_p can be found using different methods with slightly different results. One method is to define the zero crossing of the second derivative as V_p. Because there is not a large difference between the methods, and it is easiest to see on the graph, this method is used here. The first derivative was included in the figure because when gaining intuition about the RLC effects, especially the splitting of V_p and its "remnant" (explained below),

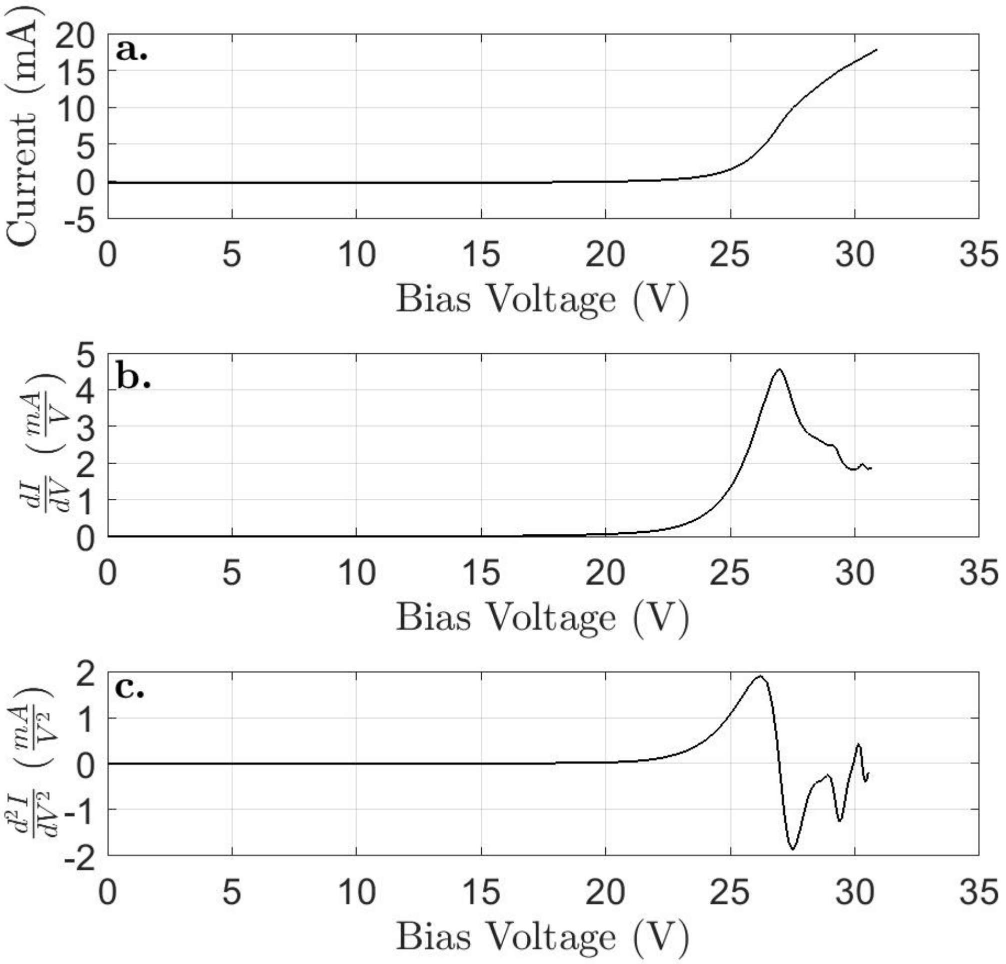

Figure 4.8. Measured IV Curve $t = 6.6$ μs (Part **a**), and its first (Part **b**) and second (Part **c**) derivatives. 75 mTorr, Ar, 10 kHz 50% duty cycle square wave pulsed plasma.

watching the movement and shape change of the peak of the first derivative was found to be very useful.

Figures 4.9 and 4.10 show the measured time evolution of the IV curve second derivative during the rf power turn on and turn off respectively, of an argon plasma rf power pulse cycle. In the figures, the time evolution of V_p is marked with an arrow, or in the case of the turn off, V_p quickly jumps and so two arrows are used. During the turn on when the RLC

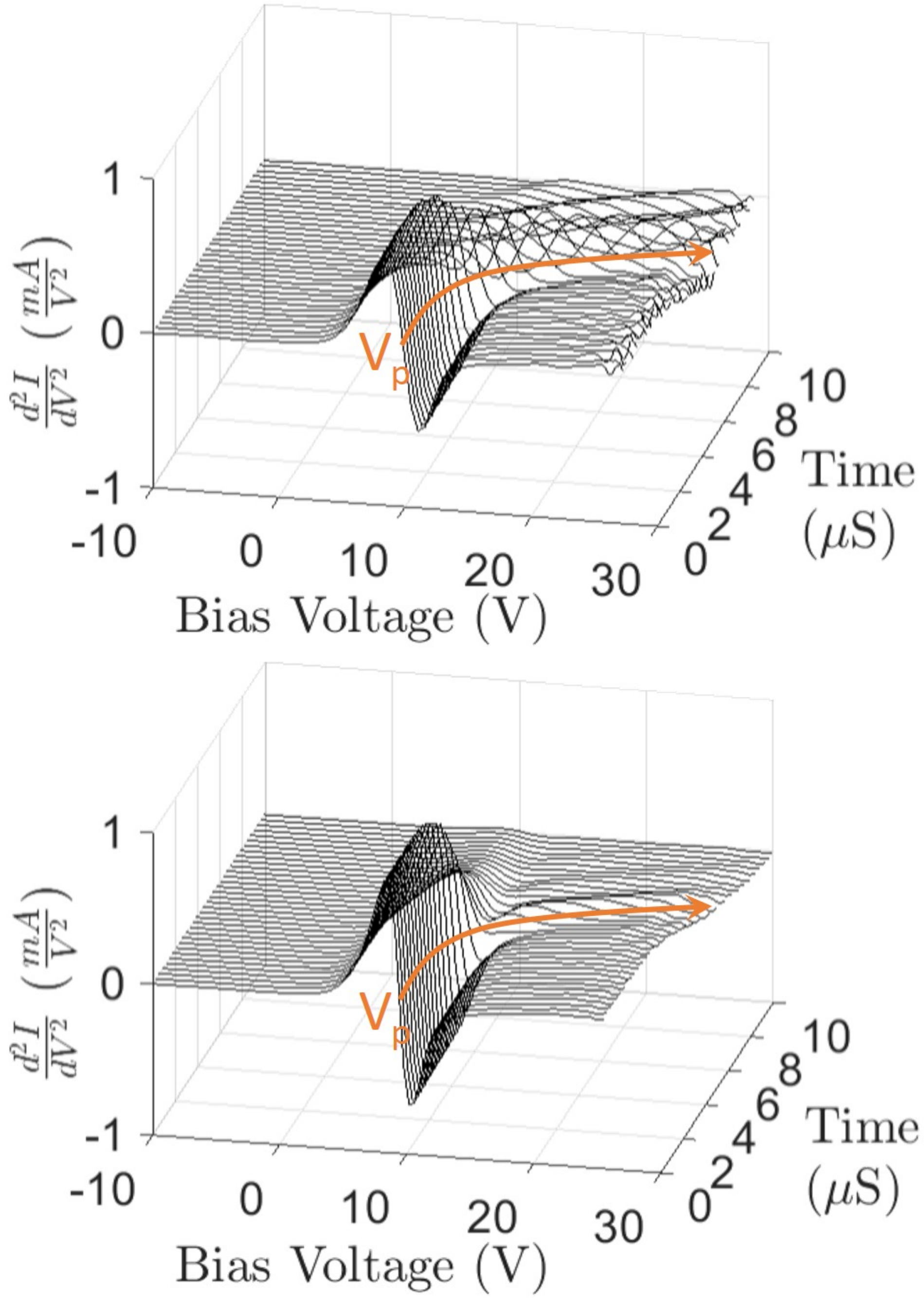

Figure 4.9. Measured IV curve second derivative during rf power turn on with the LP circuit (upper) underdamped, and (lower) overdamped. 75 mTorr, Ar, 10 kHz 50% duty cycle square wave pulsed plasma.

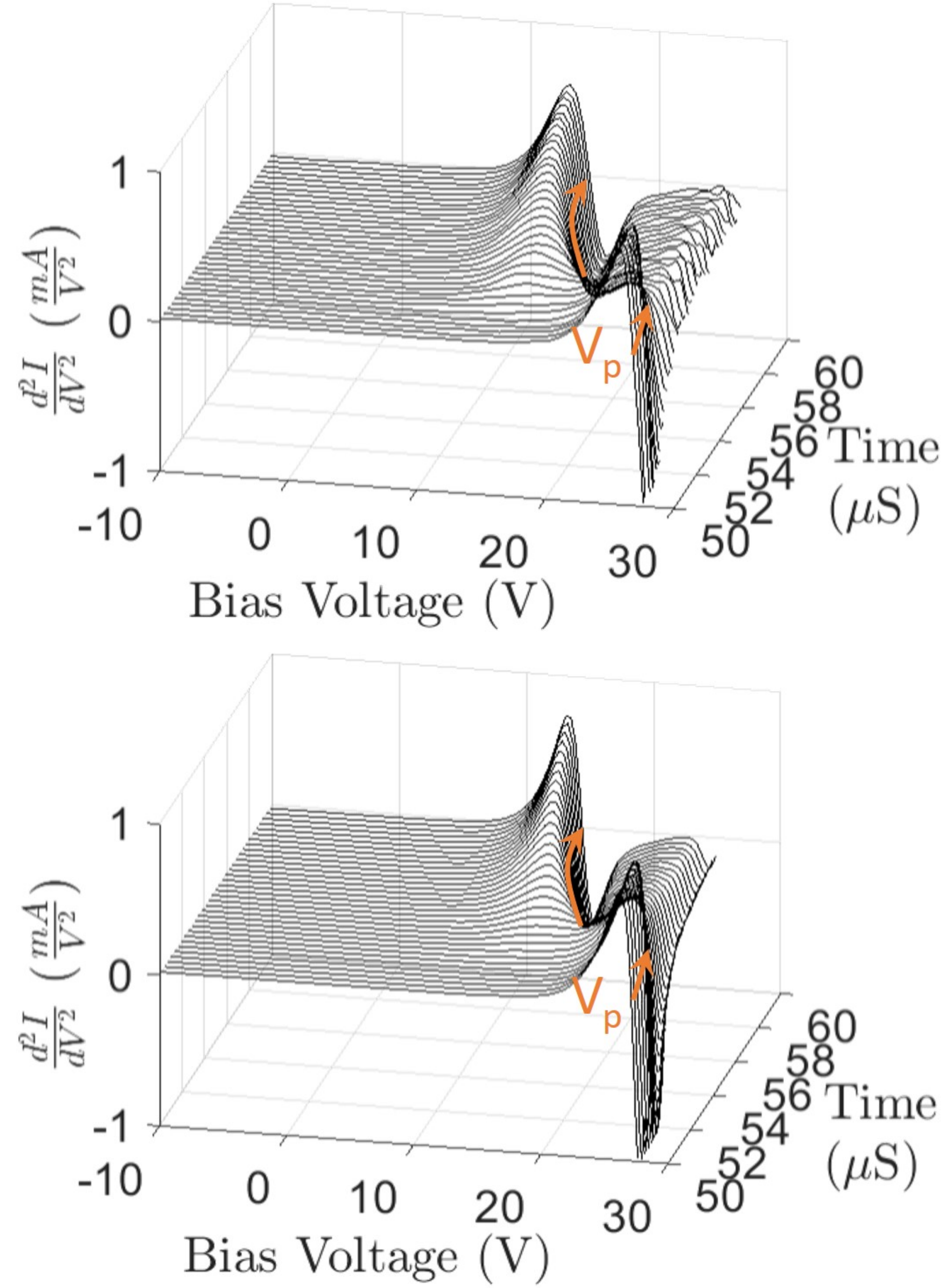

Figure 4.10. Measured IV curve second derivative during rf power turn off with the LP circuit (upper) underdamped, and (lower) overdamped. 75 mTorr, Ar, 10 kHz 50% duty cycle square wave pulsed plasma.

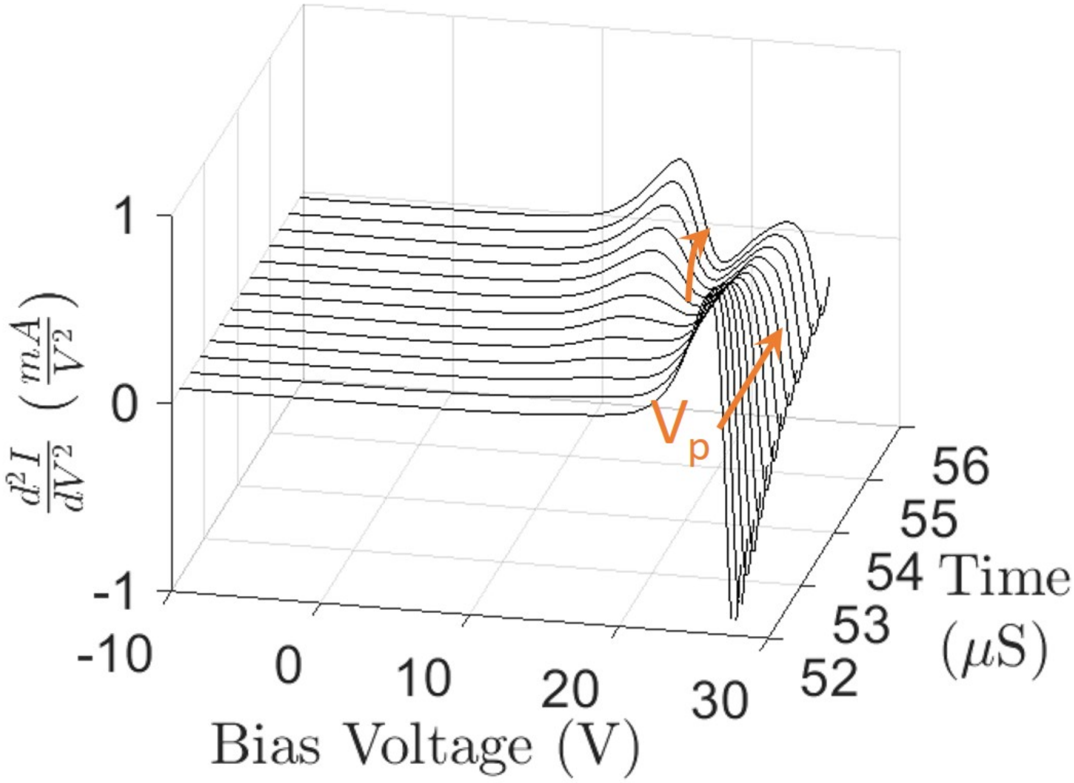

Figure 4.11. Zoomed in view of the measured IV curve second derivative during rf power turn off with the LP circuit overdamped. 75 mTorr, Ar, 10 kHz 50% duty cycle square wave pulsed plasma.

circuit is underdamped, V_p can be seen to increase, with oscillations in the second derivative in its wake. In the overdamped case, V_p moves in the same manner, however the oscillations are damped out. In both cases a "remnant" of the second derivative hump remains for a short period due to the decay time associated with RLC circuits. If V_p quickly jumps to a new value, as it does during the rf power turn off, this time delay in the build up is clearly seen.

During the rf power turn off, V_p quickly moves to a lower value and the build up at this new lower value is evident. As was the case during the turn on, the build up is slower in the overdamped case than in the underdamped case. Figure 4.11 shows a smaller time slice of the rf power turn off period with overdamped circuitry. Looking at the arrows marking V_p, the point at which V_p is measured to jump from one arrow to the next will depend on the method or algorithm used to detect V_p. If V_p is detected at the arrow corresponding to higher V_b, then the feature building up at the lower voltage will look like a population of high energy electrons. However, it is in fact the normal distribution of electrons starting to be detected in relation to the new value of V_p. If V_p is quickly detected at the arrow corresponding to lower V_b, then while the feature builds, the electron density (the integral under the curve), will be measured low. In the cases presented here V_p changes values dramatically and the issue becomes obvious, however in situations where V_p changes by one to a few $\frac{k_b T_e}{q}$, the shape may not be obviously distorted, causing the EEDF to be trusted as correct. With an understanding of the issues affecting EEDF, the calculation of T_e can be discussed.

To illustrate mismeasurement of T_e due to RLC circuit time delays and changing V_p a simple model was developed. The model considered four user set variables; V_p over the full pulse period, the RLC circuit delay constant τ, T_e, and the electron saturation current I_{esat}. I_{esat} is given by

$$I_{esat} = qnA_p\sqrt{\frac{k_b Te}{2\pi m}}, \tag{4.11}$$

where A_p is the effective surface area of the probe. Since I_{esat} is dependent on A_p, its value for the simulation is arbitrary, and was set to 2 mA. T_e was set to 2 eV, while both V_p and τ were varied. The electron current was then given by

$$I_e = I_{esat} e^{\frac{V_s}{k_B T_e}} \qquad V_s < 0, \tag{4.12}$$

and

$$I_e = I_{esat} \qquad V_s \geq 0. \tag{4.13}$$

Then for a given V_p (Part **a** of Figure 4.4), the instantaneous IV curves (Part **b** of Figure 4.12) are generated. These IV curves are unperturbed and straightforwardly relate to n and T_e. The RLC circuit delay is then taken into account.

First an initial IV curve $\big(IV(1)\big)$ is defined as the last IV curve in a pulse cycle (t=100 μs), as this IV curve is far enough away from changes in V_p that the RLC circuit effects have become negligible. The difference between this IV curve and the next in time $\big(IV(2)\big)$ is then found and multiplied by the delay factor using

$$I_{diff}(1) = \big(IV(1) - IV(2)\big)(1 - e^{\frac{-tRes}{\tau}}), \tag{4.14}$$

where $tRes$ is the time resolution, or time step between IV curves. This difference is then subtracted from $\big(IV(1)\big)$ to get the current at the measurement point in the probe circuit;

$$I_{meas}(1) = IV(1) - I_{diff}(1). \tag{4.15}$$

The rest of the measured IV curves $\big(I_{meas}(j)\big)$ are then found using

$$I_{meas}(j) = I_{meas}(j-1) - \big(I_{meas}(j-1) - IV(j)\big)(1 - e^{\frac{-tRes}{\tau}}). \tag{4.16}$$

This results in the LP measured curves shown in Part **c** of Figure 4.12. The final step is to average the IV curves over a time period equal to the probe resolution. Generally the simulation was run with $tRes = 1\ ns$ while the LP resolution was set to 100 ns and 100 IV curves were averaged to get the final LP IV curves. These curves have had their portions equal to I_{esat} and those less than 0.01 mA (where the ion current would dominate and the electron current could not be accurately resolved) removed. Finally the natural log of each curve is taken, and a linear fit is performed. The inverse of the slope of this fit is T_e.

The results of varying τ and using the V_p from Part **a** of Figure 4.4 are shown in Part **a** of Figure 4.13, while Part **b** shows the results using the composite V_p shown in Figure 4.6. Even

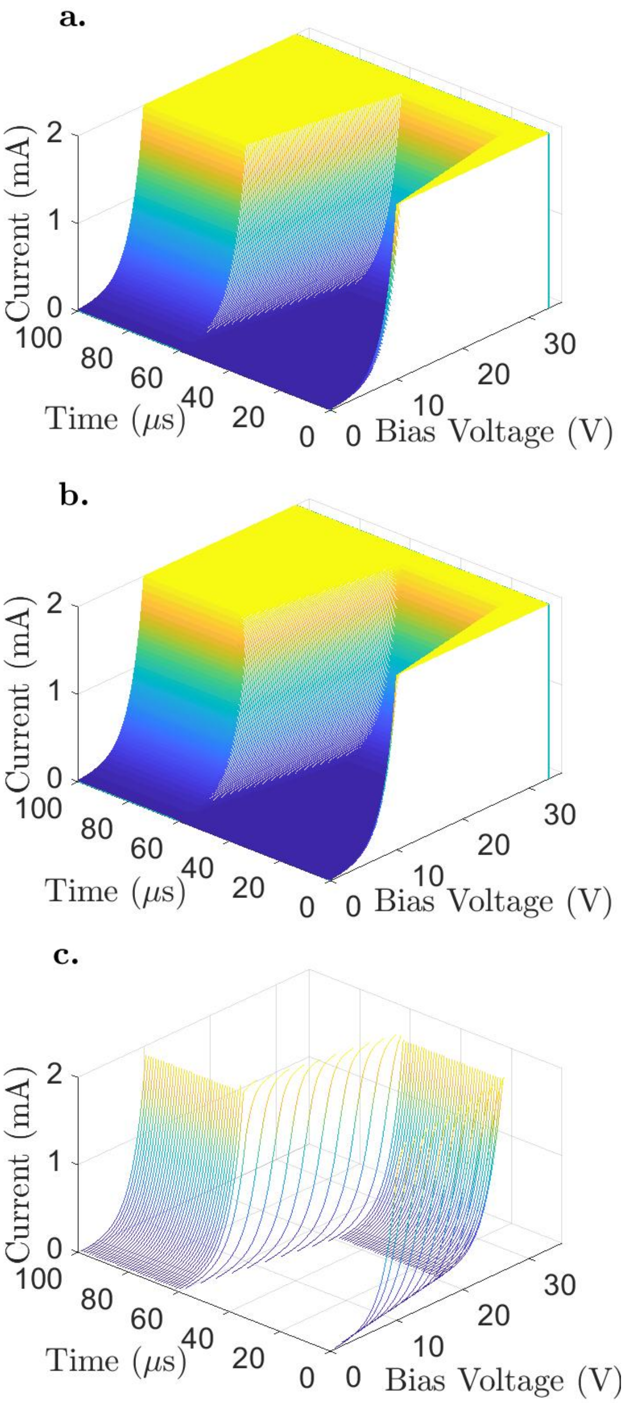

Figure 4.12. IV curve simulation instantaneous IV curves (Part **a**), IV curves with RLC time delay (Part **b**), LP time resolved IV curves (Part **c**).

though in the simulation T_e is forced to be equal to 2 eV, and only V_p is varied, the analysis of the IV curves finds "temperature spikes" in the regions where V_p is changing. One can see in Figure 4.13 that increasing τ results in increasing distortion to the IV curves, increasing the magnitude and length of the false T_e spikes. The error in T_e estimated from the IV curves can reach a factor of 3.5 times too large for nearly 15 μs in Figure 4.13 Part **a**, and a factor of 4 times too large for approximately 3 μs in Part **b**. The results plotted in Part **b** more accurately reflect the potential errors in real measurements. The time duration of the false spikes in Te are similar to or longer than the period of large $\frac{dV_p}{dt}$, with the smallest errors and shortest durations occurring when the RLC time constant for the probe is minimized. In fact, the time duration and magnitude of the false spikes corresponding to the V_p overshoot at the beginning of an rf pulse cycle (Figure 4.6) are consistent with the temperature spikes seen in prior experiments and modeling of pulsed plasmas.

4.7 Conclusion

V_p fluctuations in transient plasmas can cause incorrect calculations of both n and T_e or the EEDF. This is due to I_{dis} induced by the change in V_p, and RLC time delay causing mismeasurement of current during abrupt changes. Liu et. al. (Liu et al., 2014) have found solutions to compensate for I_{dis} and find n in the afterglow (rf power off period), however this needs to be extended to other portions of the rf power pulse cycle. RLC time delays can cause anomalous bumps in the EEDF which can be mistaken for high temperature electron populations, and change the measured IV curve slope, causing T_e to be overestimated. These overestimations can look like T_e spikes during V_p transition regions. This is not to say that T_e never spikes when rf power is applied, however spikes can be measured when they do not exist, and when they do, they will be measured to be larger than they are.

LPs designed for use in transient plasmas can reduce these effects. The RLC circuit effects can be reduced by using rf probe circuitry that is optimized for high impedance

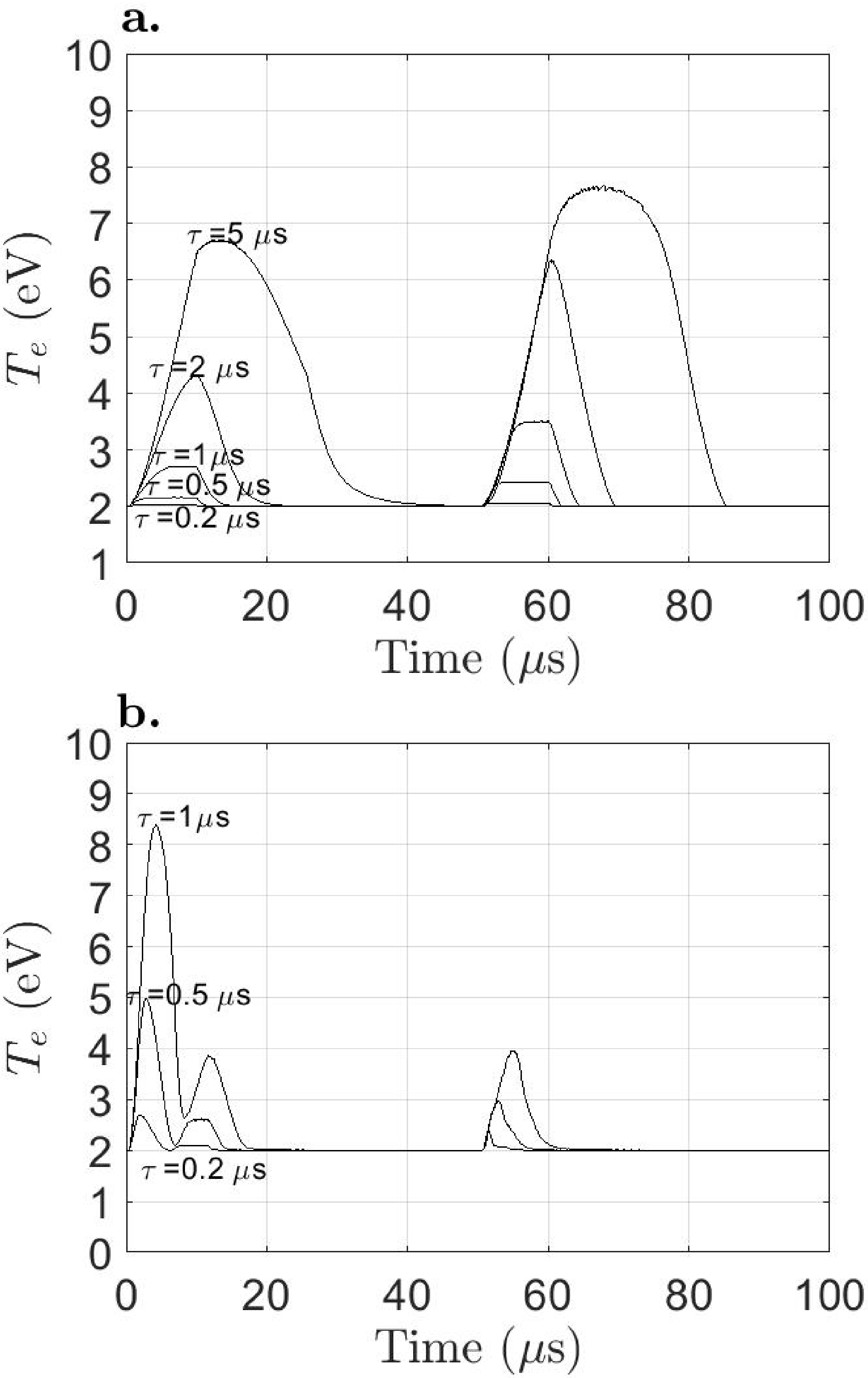

Figure 4.13. Simulated T_e spikes due to changing V_p, with various circuit delay constants. Part **a**; V_p taken from Part **a** of Figure 4.4. Part **b**; Composite V_p taken from Figure 4.6.

at rf frequencies as well as small time delay for induced transient current. The circuit components should also be well defined so that for a given measured current, the input current at the probe tip can be found using circuit theory. This must include the effects of the current measurement circuit and the bias voltage supply. Finally a method to measure the displacement current in situ is needed. This can be accomplished when the condition $C_{rf} \gg C_p$ is met using a switch which electrically disconnects the LP tip from the circuit. With the LP tip disconnected, no conduction current is measured, and the resulting current $\approx I_{dis}$ as C_{rf} is the dominant capacitance. This current can be subtracted from the current measured with the LP tip electrically connected, giving the conduction current. The combination of subtracting approximate I_{dis} and accounting for the RLC circuitry would give a better estimation of the IV curves, allowing standard DC LP theory to be used effectively.

APPENDIX A

POWER DELIVERY COMPONENTS POWERED ELECTRODE

To assist future users of the RFIV system, the physical components of the power delivery system are shown in Figures A.1 and A.2. Figure A.1 shows the full system from matching network to powered electrode, while Figure A.2 shows only the matching network and RFIV probes so that their connection can be seen clearly. When assembling this system it is important to always recalibrate the RFIV probes with the BNC cables connected to the oscilloscope that will be used in the final setup. Changing the cables after calibration will invalidate the calibration. Section 2.4 details the calibration process. Finally if any significant modification are made to this system or the mGEC chamber, the parasitic impedances and propagation delay will change. These changes must be accounted for by following the steps given in Chapter 2.

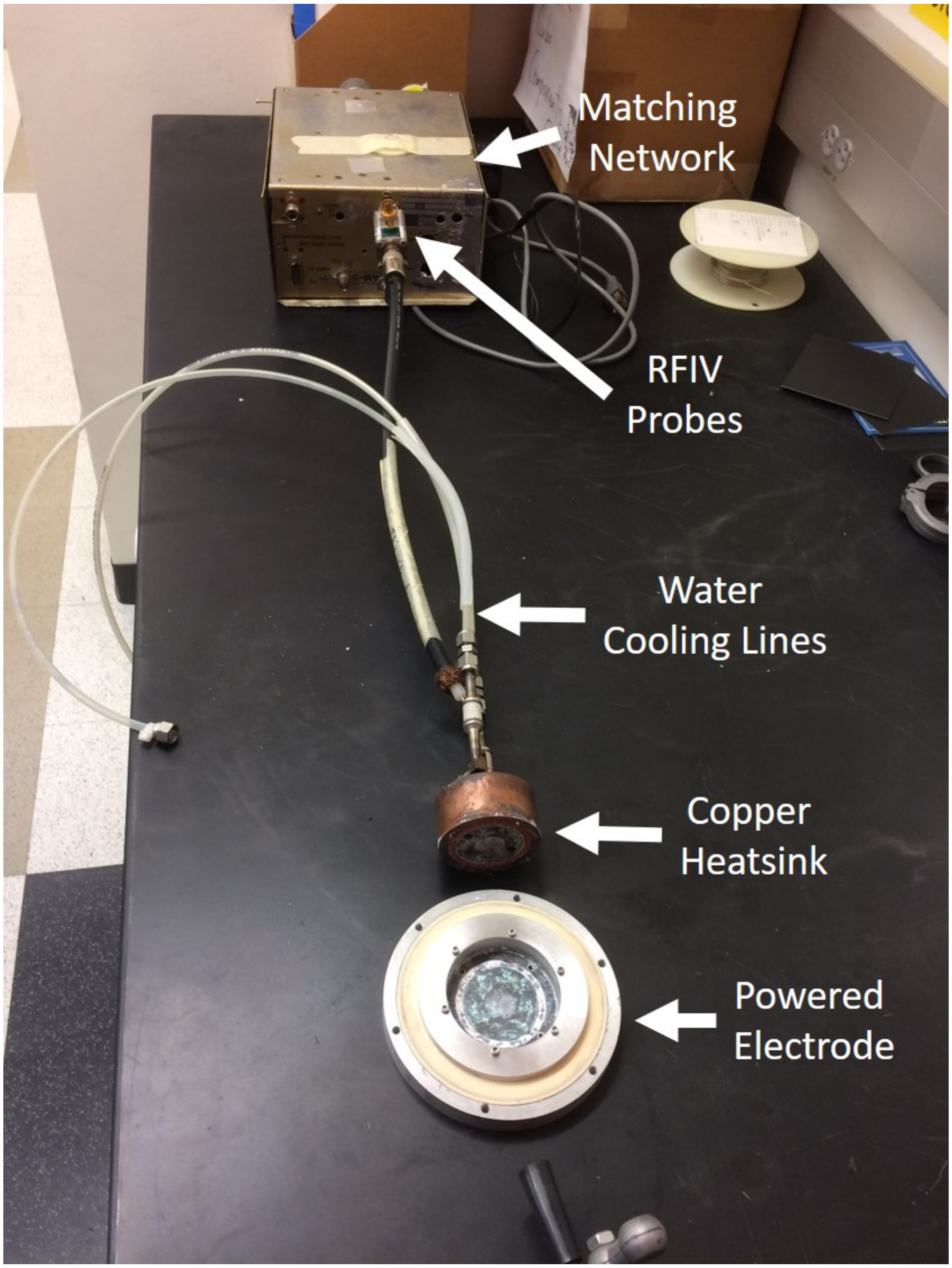

Figure A.1. Power delivery system components.

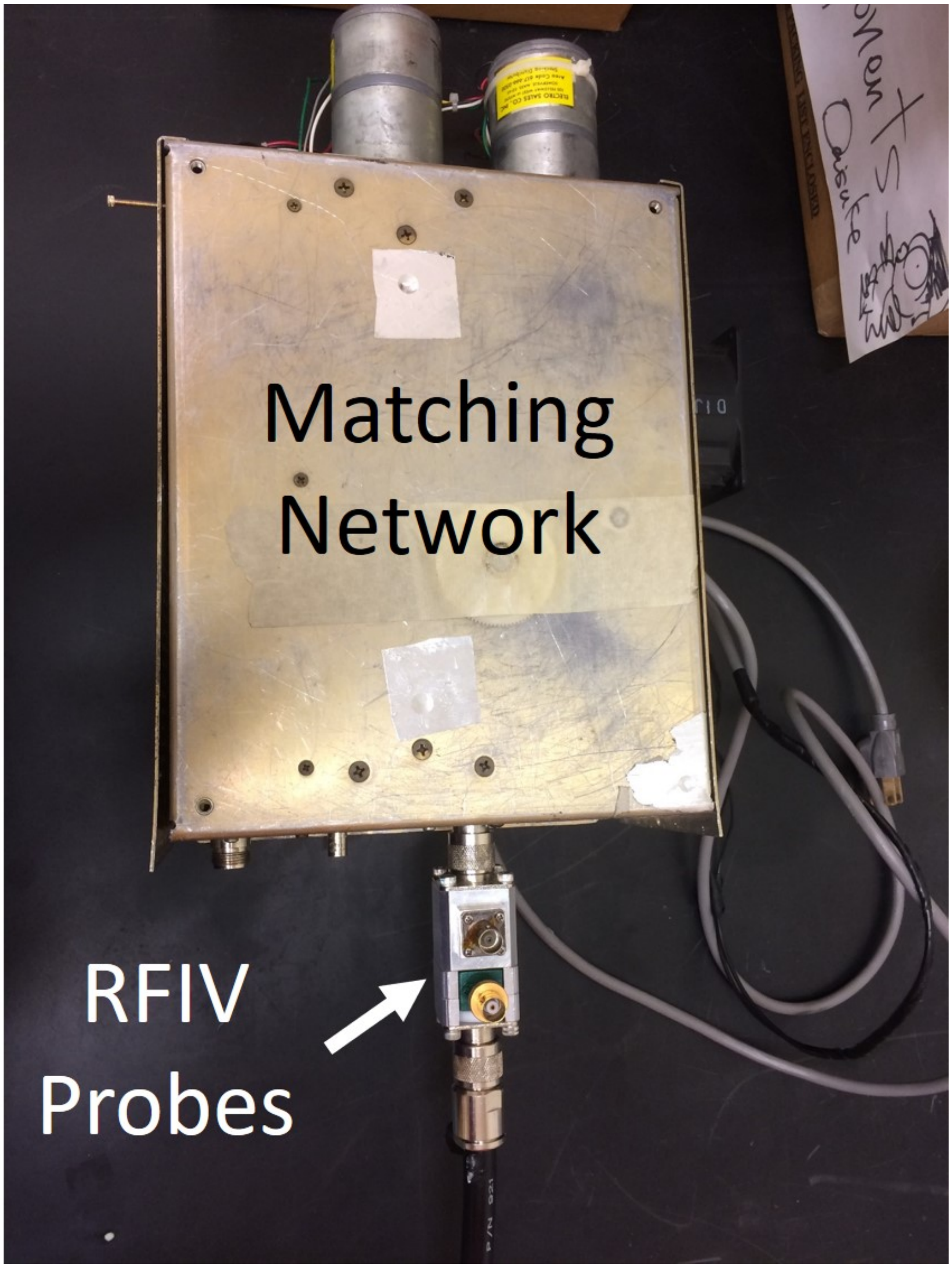

Figure A.2. Matching network and RFIV probes.

APPENDIX B

RFIV CODE

B.1 RFIV_Read_in_Data.m

Starting this code will prompt the user to select four data files; DC bias voltage, grounded electrode current, powered electrode current, and powered electrode voltage. These files will be read into the MATLAB workspace and fed to functions called by this script.

```
% This script takes in data from the Labview RFIV program exported in
% the .csv format and calls functions to calculate various parameters and
% to plot. Finally this program saves all the plots and the data file in a
% folder.
% Author Alex Press 5-1-2018

%This section clears all open Matlab figures, clears all variables from
%workspace and clears the command window. THIS MAY NOT BE DESIRED!
close all
%clear all
%clc

% Determine where your m-file's folder is.
folder = fileparts(which(mfilename));
% Add that folder plus all subfolders to the path so subfunctions can be
% found
addpath(genpath(folder));

%% fill this section out !!!!!!!!!!!
%This section is where the user can set default values for the script
DocumentFilePath='\\engfs.utdallas.edu\plasmalab\KeithAndAlexData\ArCF4\FullyPulsed\1kHz\C65\FullyPulsed';
DocumentFilePath=strcat(DocumentFilePath,'\.csv');
[data] = ConstantRepository();% initalizes constant values such as fundemental frequency

% plot settings
set(groot,'DefaultAxesFontSize',20)
set(groot,'defaultTextInterpreter','latex');
set(groot,'DefaultAxesXGrid','on');
set(groot,'DefaultAxesYGrid','on');
set(groot,'DefaultAxesZGrid','on');
set(groot, 'defaultLegendInterpreter','latex');
%set(groot,'defaultAxesColorOrder',[0 0 1]);
%set(groot,'defaultAxesLineStyleOrder','.-');
%set(groot,'defaultLineMarkerSize',12);

%% end fill out section

% First the data must be imported from the RFIV files. Since they
% are .csv this is done using [num,txt]=xlsread(filename) as this easily
```

```
% separates the text headers into the txt variable and the numeric data
% into the num variable. The filename is selected by the user.

%Selects RFIV DC data
[filenameRFIVDC,pathRFIVDC]=uigetfile(DocumentFilePath,'Select the RFIV DC DATA FILE');

%Reads RFIV DC data and sets text values into an array of strings
fileRFIVDC=strcat(pathRFIVDC,filenameRFIVDC);
[RFIVDCdatanum,RFIVDCdatatext]=xlsread(fileRFIVDC);
RFIVDCdatatext=string(RFIVDCdatatext)';

%Selects scope Grounded elctrode current data
[filenameScopeGNDI,pathScopeGNDI]=uigetfile(DocumentFilePath,'Select the Grounded Electrode Current DATA FILE');

%Reads scope Grounded elctrode current data and sets text values into an array of strings
fileGNDI=strcat(pathScopeGNDI,filenameScopeGNDI);
[GNDIdatanum,GNDIdatatext]=xlsread(fileGNDI);
GNDIdatatext=string(GNDIdatatext)';

%Selects scope Powered elctrode current data
[filenameScopePWRI,pathScopePWRI]=uigetfile(DocumentFilePath,'Select the Powered Electrode Current DATA FILE');

%Reads scope Powered elctrode current data and sets text values into an array of strings
filePWRI=strcat(pathScopePWRI,filenameScopePWRI);
[PWRIdatanum,PWRIdatatext]=xlsread(filePWRI);
PWRIdatatext=string(PWRIdatatext)';

%Selects scope Powered elctrode voltage data
[filenameScopePWRV,pathScopePWRV]=uigetfile(DocumentFilePath,'Select the Powered Electrode Voltage DATA FILE');

%Reads scope Powered elctrode voltage data and sets text values into an array of strings
filePWRV=strcat(pathScopePWRV,filenameScopePWRV);
[PWRVdatanum,PWRVdatatext]=xlsread(filePWRV);
PWRVdatatext=string(PWRVdatatext)';

%Selects scope Powered elctrode voltage data
[filenameScopeTime,pathScopeTime]=uigetfile(DocumentFilePath,'Select the Time DATA FILE');

%Reads scope Powered elctrode voltage data and sets text values into an array of strings
fileTime=strcat(pathScopeTime,filenameScopeTime);
[Timedatanum,Timedatatext]=xlsread(fileTime);
Timedatatext=string(Timedatatext)';

%Combines RFIV data into one structure which uses the structure
%organization i.e. data.datatext would call datatext in any function called
%in the script
data.Timedatatext=Timedatatext;
data.Timedatanum=Timedatanum;
data.DCdatatext=RFIVDCdatatext;
data.DCdatanum=RFIVDCdatanum;
data.GNDIdatatext=GNDIdatatext;
data.GNDIdatanum=GNDIdatanum;
data.PWRIdatatext=PWRIdatatext;
```

```
data.PWRIdatanum=PWRIdatanum;
data.PWRVdatatext=PWRVdatatext;
data.PWRVdatanum=PWRVdatanum;

% clears duplicate data from workspace (this data is all in the data.
% structure)

%% This section calls the calculation functions

[data] = DCbias_Vector_Builder(data);
[data] = Time_Vector_Builder(data);

% Powered current probe calcs
[data] = PWR_Current_Vector_Builder(data);
[data.ChoppedOutPWRI,data.ChoppedTime] = WaveformChopper(data,data.PWRIdatanum);
[data.PWRIFFT] = ChoppedWaveformFFT(data,data.ChoppedOutPWRI);
[data] = PWRICalibrator1333(data);
%[data] = PWRDCICalc(data); % there may be something interesting here

% Grounded current probe calcs
[data] = GND_Current_Vector_Builder(data);
[data.ChoppedOutGNDI,~] = WaveformChopper(data,data.GNDIdatanum);
[data.GNDIFFT] = ChoppedWaveformFFT(data,data.ChoppedOutGNDI);
[data] = GNDICalibrator1333(data);

% Powered voltage probe calcs
[data] = PWR_Voltage_Vector_Builder(data);
[data.ChoppedOutPWRV,~] = WaveformChopper(data,data.PWRVdatanum);
[data.PWRVFFT] = ChoppedWaveformFFT(data,data.ChoppedOutPWRV);
[data] = PWRVCalibrator1333(data);

% This section calculates impedances and compensates for parasitic
% impedances.

%[data] = ImpedanceCalc(data);
[data] = ImpedanceCalc(data);

%% This section makes a folder and saves the data structure in it
savetitlefull = strcat(pathRFIVDC,filenameRFIVDC);
data.savetitle = savetitlefull(1:end-14);
mkdir(data.savetitle);


%% This section creates plots and saves them in the data folder

RFIV_Waveform_Plotter(data);
RFIV_Plotter(data)

data.RFIVdatasavetitle = strcat(data.savetitle,'\aaa_RFIVdata');

RFIVdata=data;

clearvars -except RFIVdata
save(RFIVdata.RFIVdatasavetitle);
```

B.2 RFIV_Read_in_Data.m Subfunctions

B.2.1 ConstantRepository

This function is where constants such as driving frequency, probe calibration factors, and impedance calibration factors are stored. These factors are saved into the “data” array to be used by other functions.

```
function [data] = ConstantRepository()


data.Fund=13.33e6; % must put in plasma driving frequency
data.Omega=2.*pi.*data.Fund; % calculates fundemental angular frequency


%% calibration factors
% fund, 2nd, 3rd, 4th, 5th, 6th


data.VPWRmagCal=[165.5915251,86.04156475,58.71333465,43.4293026,34.373305,28.46631138];
data.IPWRmagCal=[1.023941,1.004863,0.8414697,0.9807789,1.246873,1.131618];
data.IGNDmagCal=[0.9757013,0.946155,0.9555239,1.030841,0.9970428,0.8513991];


data.VPWRphaseCal=[0.906734666,0.2471181,-0.340777708,-0.955014219,-1.598381358,4.058842954];
data.IPWRphaseCal=[5.475323,-1.591238,-2.467783,-3.505358,2.123329,1.652339];
data.IGNDphaseCal=[2.243623,-4.967319,0.3457509,-0.5466998,-1.345408,-2.293134];



%% parasitic impedance constants


% PWR electrode forward traveling wave circuit (fundemental)



L1=50.6e-9;
C1=51.7e-12;
%R1=0.1;


% calculates the cable to ground impedances for the forward traveling wave
data.impedance.ZC1fund=1./(1i.*data.Omega.*C1);
data.impedance.ZL1fund=1i.*data.Omega.*L1;
%data.impedance.ZR1fund=R1;


data.impedance.ZC12nd=1./(1i.*data.Omega.*2.*C1);
data.impedance.ZL12nd=1i.*data.Omega.*2.*L1;
%data.impedance.ZR12nd=R1;


data.impedance.ZC13rd=1./(1i.*data.Omega.*3.*C1);
data.impedance.ZL13rd=1i.*data.Omega.*3.*L1;
%data.impedance.ZR13rd=R1;


data.impedance.ZC14th=1./(1i.*data.Omega.*4.*C1);
data.impedance.ZL14th=1i.*data.Omega.*4.*L1;
%data.impedance.ZR14th=R1;


data.impedance.ZC15th=1./(1i.*data.Omega.*5.*C1);
data.impedance.ZL15th=1i.*data.Omega.*5.*L1;
```

```
%data.impedance.ZR15th=R1;

data.impedance.ZC16th=1./(1i.*data.Omega.*6.*C1);
data.impedance.ZL16th=1i.*data.Omega.*6.*L1;
%data.impedance.ZR16th=R1;

L2=377e-9;
C2=70.8e-12;
R2=0.726933367;

% calculates the cable to ground impedances for the forward traveling wave
data.impedance.ZC2fund=1./(1i.*data.Omega.*C2);
data.impedance.ZL2fund=1i.*data.Omega.*L2;
data.impedance.ZR2fund=R2;

data.impedance.ZC22nd=1./(1i.*data.Omega.*2.*C2);
data.impedance.ZL22nd=1i.*data.Omega.*2.*L2;
data.impedance.ZR22nd=R2;

data.impedance.ZC23rd=1./(1i.*data.Omega.*3.*C2);
data.impedance.ZL23rd=1i.*data.Omega.*3.*L2;
data.impedance.ZR23rd=R2;

data.impedance.ZC24th=1./(1i.*data.Omega.*4.*C2);
data.impedance.ZL24th=1i.*data.Omega.*4.*L2;
data.impedance.ZR24th=R2;

data.impedance.ZC25th=1./(1i.*data.Omega.*5.*C2);
data.impedance.ZL25th=1i.*data.Omega.*5.*L2;
data.impedance.ZR25th=R2;

data.impedance.ZC26th=1./(1i.*data.Omega.*6.*C2);
data.impedance.ZL26th=1i.*data.Omega.*6.*L2;
data.impedance.ZR26th=R2;




% GND electrode forward traveling wave circuit (all frequencies travel in this direction)

L1=140e-9;
C1=165e-12;
R1=1.132487857;

% calculates the gounded electrode impedances
data.impedance.ZC1gndfund=1./(1i.*data.Omega.*C1);
data.impedance.ZL1gndfund=1i.*data.Omega.*L1;
data.impedance.ZR1gndfund=R1;

data.impedance.ZC1gnd2nd=1./(1i.*data.Omega.*2.*C1);
data.impedance.ZL1gnd2nd=1i.*data.Omega.*2.*L1;
data.impedance.ZR1gnd2nd=R1;
```

```
data.impedance.ZC1gnd3rd=1./(1i.*data.Omega.*3.*C1);
data.impedance.ZL1gnd3rd=1i.*data.Omega.*3.*L1;
data.impedance.ZR1gnd3rd=R1;

data.impedance.ZC1gnd4th=1./(1i.*data.Omega.*4.*C1);
data.impedance.ZL1gnd4th=1i.*data.Omega.*4.*L1;
data.impedance.ZR1gnd4th=R1;

data.impedance.ZC1gnd5th=1./(1i.*data.Omega.*5.*C1);
data.impedance.ZL1gnd5th=1i.*data.Omega.*5.*L1;
data.impedance.ZR1gnd5th=R1;

data.impedance.ZC1gnd6th=1./(1i.*data.Omega.*6.*C1);
data.impedance.ZL1gnd6th=1i.*data.Omega.*6.*L1;
data.impedance.ZR1gnd6th=R1;
```

B.2.2 DCbias_Vector_Builder

If the DC bias is exported as one vector its length will cause the programs to crash. Therefore it is turned into a matrix by the LabView code. It is then turned back into a vector and saved in the “data” array by this function.

```
function [data] = DCbias_Vector_Builder(data)

%takes in DC bias data in matrix form and reforms it into a vector
data.DCdatanum = reshape(data.DCdatanum',[],1);
```

B.2.3 Time_Vector_Builder

This function finds the oscilloscope time vector data, creates a MATLAB time vector and saves it in the “data” array.

```
function [data] = Time_Vector_Builder(data)

%Finds starting point index
[Initial_X,~]=find(strcmp(data.Timedatatext,'Initial X'));

%Finds Time Increment
[Increment,~]=find(strcmp(data.Timedatatext,'Increment'));

%Finds Number of points
Num_Points=length(data.DCdatanum);

% Calculates endpoint value
End_X=data.Timedatanum(Initial_X)+data.Timedatanum(Increment).*Num_Points;

%takes in Time data in and creates a vector
Tvec= linspace(data.Timedatanum(Initial_X),End_X,Num_Points);
data.TimeLong = Tvec';
```

B.2.4 PWR_Current_Vector_Builder

This function acts similarly to DCbias_Vector_Builder by building the powered electrode current vector and saving it in the “data” array.

```
function [data] = PWR_Current_Vector_Builder(data)


%takes in Powered Electrode Current data in matrix form and reforms it into a vector

data.PWRIdatanum = reshape(data.PWRIdatanum’,[],1);
```

B.2.5 GND_Current_Vector_Builder

This function acts similarly to DCbias_Vector_Builder by building the grounded electrode current vector and saving it in the “data” array.

```
function [data] = GND_Current_Vector_Builder(data)


%takes in Grounded Electrode Current data in matrix form and reforms it into a vector

data.GNDIdatanum = reshape(data.GNDIdatanum’,[],1);
```

B.2.6 PWR_Voltage_Vector_Builder

This function acts similarly to DCbias_Vector_Builder by building the powered electrode voltage vector and saving it in the “data” array.

```
function [data] = PWR_Voltage_Vector_Builder(data)


%takes in Powered Electrode Voltage data in matrix form and reforms it into a vector

data.PWRVdatanum = reshape(data.PWRVdatanum’,[],1);
```

B.2.7 WaveformChopper

This function chops the rf waveforms into one period sections, and the linearly interpolates that section so that the number of data points is equal to the lowest power of two larger than the original data set and saves the chopped waveforms in the “data” array.

```
function [ChoppedOut,ChoppedTime] = WaveformChopper(data,Waveform)


% fundemental frequency

freq=data.Fund;



% ocilliscope sample rate

SamppleRate=1./data.Timedatanum(2);


% ocilliscope time step and fundemental frequency period

TimeStep=1./SamppleRate;

CyclePeriod=1./freq;


% how many samples are in one rf period. This will not be a whole number
```

```
Samples=CyclePeriod./TimeStep;

% Find the lowest n^2 value greater than the number of samples in a period

binarynumbers=[1,2,4,8,16,32,64,128,256,512,1024,2048,4096,8192,16384,32768];
binarynumbersgreaterthan=binarynumbers(binarynumbers>Samples);
N2Value=binarynumbersgreaterthan(1);

%%%%%%%%%%%%%%%%%%%%%%%%%%%%%%%%%%%%%%%%
%Waveform=data.PWRIdatanum;
Time=data.TimeLong;

%%%%%%%%%%%%%%%%%%%%%%%%%%%%%%%%%%%%%%%%%%%

% how many full cycles are there in a data cycle

TotalCycles=floor(Time(end)./CyclePeriod);

% initalize start point and stop point vectors. These vectors give the
% indacies where the cycles should be started and stopped. Note they are
% not whole numbers and so linear interplation is required



c=linspace(1,TotalCycles,TotalCycles);
startpoints=(c-1).*Samples+1;
stoppoints=(c).*Samples+1;

% creates start values

x0=floor((c-1)*Samples)+1;
x1=ceil((c-1)*Samples)+1;
x=(c-1).*Samples+1;
y0=Waveform(x0)';
y1=Waveform(x1)';

startpointValue=y0+(y1-y0).*(x-x0)./(x1-x0);

% if the values of x1 and x0 are the same i.e. x is a whole number then the
% equation gives a NaN value. In this case the value is set to the
% corisponding y0 value


startNaNindex=isnan(startpointValue);
startpointValue(startNaNindex)=y0(startNaNindex);

% create stop values

x0=floor((c)*Samples)+1;
x1=ceil((c)*Samples)+1;
x=(c).*Samples+1;
y0=Waveform(x0)';
y1=Waveform(x1)';
```

```
stoppointValue=y0+(y1-y0).*(x-x0)./(x1-x0);

% if the values of x1 and x0 are the same i.e. x is a whole number then the
% equation gives a NaN value. In this case the value is set to the
% corisponding y0 value.


stopNaNindex=isnan(stoppointValue);
stoppointValue(stopNaNindex)=y0(stopNaNindex);




% Chop up waveform and linear interprate to n^2 value.
ChoppedOut=zeros(TotalCycles,N2Value);
ChoppedTime=zeros(TotalCycles,1);

for loop=1:TotalCycles

n=floor(stoppoints(loop)-ceil(startpoints(loop)));
yvector=Waveform(ceil(startpoints(loop)):floor(stoppoints(loop)));
xvector=linspace(ceil(startpoints(loop)),floor(stoppoints(loop)),n+1);
yvalues=horzcat(startpointValue(loop),yvector',stoppointValue(loop));
xvalues=horzcat(startpoints(loop),xvector,stoppoints(loop));




if startNaNindex(loop)==1
xvalues=xvalues(2:end);
yvalues=yvalues(2:end);
else


end

if stopNaNindex(loop)==1
xvalues=xvalues(1:end-1);
yvalues=yvalues(1:end-1);
else


end

xq=linspace(startpoints(loop),stoppoints(loop),N2Value);
ChoppedOut(loop,:)=interp1(xvalues,yvalues,xq);
ChoppedTime(loop,1)=mean(xq.*TimeStep);
end
```

B.2.8 ChoppedWaveformFFT

This function performes an FFT on the chopped waveforms and saves the magnitude and phase data in the “data” array.

```
function [fftdata] = ChoppedWaveformFFT(data,waveform)


%what=fft(ChoppedWaveform');


[~,L]=size(waveform);


T=1./data.Fund;
fs=T./L;



fftdatadoubleside=fft(waveform');


% convert two sided fft to one sided
fftdatasingle=fftdatadoubleside(1:L/2+1,:);
fftdatasingle(2:end-1,:)=2*fftdatasingle(2:end-1,:);



phase=angle(fftdatasingle);
Mag=abs(fftdatasingle)./L;
f=data.Fund*(0:(L/2));
% output is a cell of phase in rads, magnitude and frequency vector
fftdata={phase,Mag,f};
```

B.2.9 PWRICalibrator1333

Performs the powered electrode current probe calibration. These factors will have to be found again and changed in the is the ConstantRepository function if the driving frequency or physical probe are changed.

```
function [data] = PWRICalibrator1333(data)


mag=data.IPWRmagCal;
phase=data.IPWRphaseCal;


calmag1=data.PWRIFFT{2}(2,:).*mag(1);
calmag2=data.PWRIFFT{2}(3,:).*mag(2);
calmag3=data.PWRIFFT{2}(4,:).*mag(3);
calmag4=data.PWRIFFT{2}(5,:).*mag(4);
calmag5=data.PWRIFFT{2}(6,:).*mag(5);
calmag6=data.PWRIFFT{2}(7,:).*mag(6);


data.PWRIcalMagFFT=vertcat(calmag1,calmag2,calmag3,calmag4,calmag5,calmag6);


calphase1=data.PWRIFFT{1}(2,:)-phase(1);
```

```
calphase2=data.PWRIFFT{1}(3,:)-phase(2);
calphase3=data.PWRIFFT{1}(4,:)-phase(3);
calphase4=data.PWRIFFT{1}(5,:)-phase(4);
calphase5=data.PWRIFFT{1}(6,:)-phase(5);
calphase6=data.PWRIFFT{1}(7,:)-phase(6);

data.PWRIcalPhaseFFT=vertcat(calphase1,calphase2,calphase3,calphase4,calphase5,calphase6);
```

B.2.10 GNDICalibrator1333

Performs the grounded electrode current probe calibration. These factors will have to be found again and changed in the is the ConstantRepository function if the driving frequency or physical probe are changed.

```
function [data] = GNDICalibrator1333(data)

mag=data.IGNDmagCal;
phase=data.IGNDphaseCal;

calmag1=data.GNDIFFT{2}(2,:).*mag(1);
calmag2=data.GNDIFFT{2}(3,:).*mag(2);
calmag3=data.GNDIFFT{2}(4,:).*mag(3);
calmag4=data.GNDIFFT{2}(5,:).*mag(4);
calmag5=data.GNDIFFT{2}(6,:).*mag(5);
calmag6=data.GNDIFFT{2}(7,:).*mag(6);

data.GNDIcalMagFFT=vertcat(calmag1,calmag2,calmag3,calmag4,calmag5,calmag6);

calphase1=data.GNDIFFT{1}(2,:)-phase(1);
calphase2=data.GNDIFFT{1}(3,:)-phase(2);
calphase3=data.GNDIFFT{1}(4,:)-phase(3);
calphase4=data.GNDIFFT{1}(5,:)-phase(4);
calphase5=data.GNDIFFT{1}(6,:)-phase(5);
calphase6=data.GNDIFFT{1}(7,:)-phase(6);

data.GNDIcalPhaseFFT=vertcat(calphase1,calphase2,calphase3,calphase4,calphase5,calphase6);
```

B.2.11 PWRVCalibrator1333

Performs the powered electrode voltage probe calibration. These factors will have to be found again and changed in the is the ConstantRepository function if the driving frequency or physical probe are changed.

```
function [data] = PWRVCalibrator1333(data)

mag=data.VPWRmagCal;
phase=data.VPWRphaseCal;

calmag1=data.PWRVFFT{2}(2,:).*mag(1);
calmag2=data.PWRVFFT{2}(3,:).*mag(2);
calmag3=data.PWRVFFT{2}(4,:).*mag(3);
```

```
calmag4=data.PWRVFFT{2}(5,:).*mag(4);
calmag5=data.PWRVFFT{2}(6,:).*mag(5);
calmag6=data.PWRVFFT{2}(7,:).*mag(6);

data.PWRVcalMagFFT=vertcat(calmag1,calmag2,calmag3,calmag4,calmag5,calmag6);

calphase1=data.PWRVFFT{1}(2,:)-phase(1);
calphase2=data.PWRVFFT{1}(3,:)-phase(2);
calphase3=data.PWRVFFT{1}(4,:)-phase(3);
calphase4=data.PWRVFFT{1}(5,:)-phase(4);
calphase5=data.PWRVFFT{1}(6,:)-phase(5);
calphase6=data.PWRVFFT{1}(7,:)-phase(6);

data.PWRVcalPhaseFFT=vertcat(calphase1,calphase2,calphase3,calphase4,calphase5,calphase6);
```

B.2.12 ImpedanceCalc

This function calculates the plasma impedance, and performs the chamber parasitic impedance corrections. This includes the propagation delay corrections.

```
function [data] = ImpedanceCalc(data)

%% first the impedances measured by the pwr electrode probes at the
% fundemental, second and third harmonics are found
% these values are in polar coordinates and must be changes to cartesian

[REAL,IMAG]=pol2cart(data.PWRIcalPhaseFFT(1,:),data.PWRIcalMagFFT(1,:));
complexI=REAL+1i*IMAG;
Iprobefund=complexI;
[REAL,IMAG]=pol2cart(data.PWRVcalPhaseFFT(1,:),data.PWRVcalMagFFT(1,:));
complexV=REAL+1i*IMAG;
Vprobefund=complexV;
data.impedance.Fund=complexV./complexI;


% for the second harmonic pi is added to the current phase as the waveform
% is traveling in the reverse direction from that of the probe calibration

[REAL,IMAG]=pol2cart(data.PWRIcalPhaseFFT(2,:)+pi,data.PWRIcalMagFFT(2,:));
complexI=REAL+1i*IMAG;
Iprobe2nd=complexI;
[REAL,IMAG]=pol2cart(data.PWRVcalPhaseFFT(2,:),data.PWRVcalMagFFT(2,:));
complexV=REAL+1i*IMAG;
Vprobe2nd=complexV;
data.impedance.har2ND=complexV./complexI;


% for the third harmonic pi is added to the current phase as the waveform
% is traveling in the reverse direction from that of the probe calibration

[REAL,IMAG]=pol2cart(data.PWRIcalPhaseFFT(3,:)+pi,data.PWRIcalMagFFT(3,:));
complexI=REAL+1i*IMAG;
```

```
Iprobe3rd=complexI;
[REAL,IMAG]=pol2cart(data.PWRVcalPhaseFFT(3,:),data.PWRVcalMagFFT(3,:));
complexV=REAL+1i*IMAG;
Vprobe3rd=complexV;
data.impedance.har3RD=complexV./complexI;

%% second the input impedance of the plasma is found

ZC1fund=data.impedance.ZC1fund;
ZL1fund=data.impedance.ZL1fund;
%ZR1fund=data.impedance.ZR1fund;

ZC2fund=data.impedance.ZC2fund;
ZL2fund=data.impedance.ZL2fund;
ZR2fund=data.impedance.ZR2fund;

small_block=1./(1./(data.impedance.Fund-ZL1fund)-1./(ZC1fund));
med_block=1./(small_block-ZL2fund-ZR2fund);
data.impedance.Zplasma=1./(med_block-1./ZC2fund);

%% funedmental frequnecy current and voltage waveforms
% Using the found plasma impedance, probe impedance, and impedances from
% the lump element equivelent circuit, fundemental frequnecy current and
% voltages at the plasma-electrode interface can be found.

% The input impedance at several nodes are found
Z3=1./(1./(ZC2fund)+1./(data.impedance.Zplasma));
Z2=1./(1./(ZC1fund)+1./(ZR2fund+ZL2fund+Z3));
Z1=ZL1fund+Z2; % this should be equal to the probe found input impedance

% an intermidiate voltage is found
V2=Vprobefund.*Z2./Z1;
I3=V2./(ZR2fund+ZL2fund+Z3);
% The fundemeantal voltage is corrected
PWRVFundCor=I3.*Z3;

I3_method2=Iprobefund-V2./ZC1fund;
% The fundemeantal voltage is corrected
PWRIFundCor=I3_method2-(I3_method2.*Z3)./ZC2fund;

%% the input impedance of the electrode circuit from the plasma is found

% The second harmonic powered electrode imput impedance (from the plasma to
% the elctrode) is found since the harmonics are generated in the plasma
% and travel in the reverse direction from the fundemental frequnecy waves

ZC12nd=data.impedance.ZC12nd;
ZL12nd=data.impedance.ZL12nd;
%ZR12nd=data.impedance.ZR12nd;

ZC22nd=data.impedance.ZC22nd;
ZL22nd=data.impedance.ZL22nd;
ZR22nd=data.impedance.ZR22nd;
```

```
data.impedance.ZPWRelectrode2nd=1./(1./(ZC22nd)+1./(ZL22nd+ZR22nd+1./(1./(ZC12nd)+1./(ZL12nd+data.impedance.har2ND))));

% The third harmonic powered electrode imput impedance (from the plasma to
% the elctrode) is found.

ZC13rd=data.impedance.ZC13rd;
ZL13rd=data.impedance.ZL13rd;
%ZR13rd=data.impedance.ZR13rd;

ZC23rd=data.impedance.ZC23rd;
ZL23rd=data.impedance.ZL23rd;
ZR23rd=data.impedance.ZR23rd;

data.impedance.ZPWRelectrode3rd=1./(1./(ZC23rd)+1./(ZL23rd+ZR23rd+1./(1./(ZC13rd)+1./(ZL13rd+data.impedance.har3RD))));

%% harmonic frequnecy current and voltage waveforms
% Using the found plasma electrode impedance, probe impedance, and
% impedances from the lump element equivelent circuit, harmonic frequnecy
% current and voltages at the plasma-electrode interface can be found.
Z1=data.impedance.har2ND;
Z2=1./(1./(ZC12nd)+1./(ZL12nd+Z1));
Z3=1./(1./(ZC22nd)+1./(ZL22nd+ZR22nd+Z2));

% The 2nd harmonic voltage is found
V2=Iprobe2nd.*(ZL12nd+data.impedance.har2ND);
V3=(V2./Z2).*(ZR22nd+ZL22nd+Z2);
PWRV2ndCor=V3;
% The 2nd harmonic current is found
I2=Iprobe2nd+V2./ZC12nd;
I3=I2+I2.*(ZR22nd+ZL22nd+Z2)./ZC22nd;
PWRI2ndCor=I3;

% 3rd harmonic
Z1=data.impedance.har3RD;
Z2=1./(1./(ZC13rd)+1./(ZL13rd+Z1));
Z3=1./(1./(ZC23rd)+1./(ZL23rd+ZR23rd+Z2));

% The 3rd harmonic voltage is found
V2=Iprobe3rd.*(ZL13rd+data.impedance.har3RD);
V3=(V2./Z2).*(ZR23rd+ZL23rd+Z2);
PWRV3rdCor=V3;
% The 2nd harmonic current is found
I2=Iprobe3rd+V2./ZC13rd;
I3=I2+I2.*(ZR23rd+ZL23rd+Z2)./ZC23rd;
PWRI3rdCor=I3;

%% The corrected waves are converted into polar coordinates

data.waveforms.PWRelecCurrentMag=zeros(3,length(PWRIFundCor));
data.waveforms.PWRelecCurrentPhase=zeros(3,length(PWRIFundCor));
data.waveforms.PWRelecVoltageMag=zeros(3,length(PWRVFundCor));
data.waveforms.PWRelecVoltagePhase=zeros(3,length(PWRVFundCor));
```

```
% the phases are modfied due to the propegation difference between the
% forward propegating fundemental frequnecy and the backwards propegating
% harmonics. This is set to work only for 13.33, 26.66 and 39.99 MHz

funddelay=14.99./2; % in nS
seconddelay=-11.78./2; % in nS
thirddelay=-9.57./2; % in nS



phasedelayfund=funddelay./75.*2.*pi;
phasedelay2nd=seconddelay./37.5.*2.*pi;
phasedelay3rd=thirddelay./25.*2.*pi;

% The fundemental current and voltage phase and magnitude are put into the
% data array

[data.waveforms.PWRelecCurrentPhase(1,:),data.waveforms.PWRelecCurrentMag(1,:)] = cart2pol(real(PWRIFundCor),imag(PWRIFundCor));
[data.waveforms.PWRelecVoltagePhase(1,:),data.waveforms.PWRelecVoltageMag(1,:)] = cart2pol(real(PWRVFundCor),imag(PWRVFundCor));
data.waveforms.PWRelecCurrentPhase(1,:)=data.waveforms.PWRelecCurrentPhase(1,:)+phasedelayfund;
data.waveforms.PWRelecVoltagePhase(1,:)=data.waveforms.PWRelecVoltagePhase(1,:)+phasedelayfund;
% The 2nd harmonic current and voltage phase and magnitude are put into the
% data array

[data.waveforms.PWRelecCurrentPhase(2,:),data.waveforms.PWRelecCurrentMag(2,:)] = cart2pol(real(PWRI2ndCor),imag(PWRI2ndCor));
[data.waveforms.PWRelecVoltagePhase(2,:),data.waveforms.PWRelecVoltageMag(2,:)] = cart2pol(real(PWRV2ndCor),imag(PWRV2ndCor));
% pi is subtracted from the phase so that current is defined in the same
% direction for the fundemental and harmonic frequnecies. (We added the pi
% in above to find the input impedance of the match network measured at the
% probes.
data.waveforms.PWRelecCurrentPhase(2,:)=data.waveforms.PWRelecCurrentPhase(2,:)-pi+phasedelay2nd;
data.waveforms.PWRelecVoltagePhase(2,:)=data.waveforms.PWRelecVoltagePhase(2,:)+phasedelay2nd;
% The 3rd harmonic current and voltage phase and magnitude are put into the
% data array

[data.waveforms.PWRelecCurrentPhase(3,:),data.waveforms.PWRelecCurrentMag(3,:)] = cart2pol(real(PWRI3rdCor),imag(PWRI3rdCor));
[data.waveforms.PWRelecVoltagePhase(3,:),data.waveforms.PWRelecVoltageMag(3,:)] = cart2pol(real(PWRV3rdCor),imag(PWRV3rdCor));
% pi is subtracted from the phase so that current is defined in the same
% direction for the fundemental and harmonic frequnecies. (We added the pi
% in above to find the input impedance of the match network measured at the
% probes.
data.waveforms.PWRelecCurrentPhase(3,:)=data.waveforms.PWRelecCurrentPhase(3,:)-pi+phasedelay3rd;
data.waveforms.PWRelecVoltagePhase(3,:)=data.waveforms.PWRelecVoltagePhase(3,:)+phasedelay3rd;

%% grounded electrode calulations are then made

%% the input impedance of the grounded electrode circuit from the plasma is found
% because there is no changing impedances as there were for the powered
% electrode circuit (the plasma for the fundemental frequnecy, and the
% match network impedance at the harmonics), the input impedance is
% calulated soly from the impedances found by the lump element circuit
% model. Also all frequnecys propagate in the same direction and the same
% impedance configuration can be used.
```

```
ZC1gndFund=data.impedance.ZC1gndfund;
ZL1gndFund=data.impedance.ZL1gndfund;
ZR1gndFund=data.impedance.ZR1gndfund;

ZC1gnd2nd=data.impedance.ZC1gnd2nd;
ZL1gnd2nd=data.impedance.ZL1gnd2nd;
ZR1gnd2nd=data.impedance.ZR1gnd2nd;

ZC1gnd3rd=data.impedance.ZC1gnd3rd;
ZL1gnd3rd=data.impedance.ZL1gnd3rd;
ZR1gnd3rd=data.impedance.ZR1gnd3rd;

% the grounded electrode input impedance is found at the fundemental
% frequnecy
data.impedance.ZGNDelectrodeFund=1./(1./(ZC1gndFund)+1./(ZL1gndFund+ZR1gndFund));

% the grounded electrode input impedance is found at the 2nd harmonic
data.impedance.ZGNDelectrode2nd=1./(1./(ZC1gnd2nd)+1./(ZL1gnd2nd+ZR1gnd2nd));

% the grounded electrode input impedance is found at the 3rd harmonic
data.impedance.ZGNDelectrode3rd=1./(1./(ZC1gnd3rd)+1./(ZL1gnd3rd+ZR1gnd3rd));

%% the grounded electrode probe current is

% the fundemental grounded electrode current is
[REAL,IMAG]=pol2cart(data.GNDIcalPhaseFFT(1,:)+pi,data.GNDIcalMagFFT(1,:));
complexI=REAL+1i*IMAG;
IGNDprobefund=complexI;
% where pi has been added as the current is moving in the opposite
% direction from the probe calibration. (All probes were calibrated so that
% positive current flowing into the plasma was positive)

% the 2nd grounded electrode current is
[REAL,IMAG]=pol2cart(data.GNDIcalPhaseFFT(2,:)+pi,data.GNDIcalMagFFT(2,:));
complexI=REAL+1i*IMAG;
IGNDprobe2nd=complexI;
% where pi has been added as the current is moving in the opposite
% direction from the probe calibration. (All probes were calibrated so that
% positive current flowing into the plasma was positive)

% the 3rd grounded electrode current is
[REAL,IMAG]=pol2cart(data.GNDIcalPhaseFFT(3,:)+pi,data.GNDIcalMagFFT(3,:));
complexI=REAL+1i*IMAG;
IGNDprobe3rd=complexI;
% where pi has been added as the current is moving in the opposite
% direction from the probe calibration. (All probes were calibrated so that
% positive current flowing into the plasma was positive)

%% the grounded electrode current measured at the probe is converted to
% the voltage at the plasma-electrode boundary

% for the fundemental frequnecy
```

```
GNDVFundCor=IGNDprobefund.*(ZL1gndFund+ZR1gndFund);

% for the 2nd harmonic frequnecy
GNDV2ndCor=IGNDprobe2nd.*(ZL1gnd2nd+ZR1gnd2nd);

% for the 3rd harmonic frequnecy
GNDV3rdCor=IGNDprobe3rd.*(ZL1gnd3rd+ZR1gnd3rd);

% the current is then

% for the fundemental frequnecy
GNDIFundCor=IGNDprobefund+GNDVFundCor./ZC1gndFund;

% for the 2nd harmonic frequnecy
GNDI2ndCor=IGNDprobe2nd+GNDV2ndCor./ZC1gnd2nd;

% for the 3rd harmonic frequnecy
GNDI3rdCor=IGNDprobe3rd+GNDV3rdCor./ZC1gnd3rd;

%% the grounded electrode current and voltage are saved into data

data.waveforms.GNDelecCurrentMag=zeros(3,length(GNDIFundCor));
data.waveforms.GNDelecCurrentPhase=zeros(3,length(GNDIFundCor));
data.waveforms.GNDelecVoltageMag=zeros(3,length(GNDVFundCor));
data.waveforms.GNDelecVoltagePhase=zeros(3,length(GNDVFundCor));

% the phases are modfied due to the propegation difference between the
% forward propegating fundemental frequnecy and the backwards propegating
% harmonics. This is set to work only for 13.33, 26.66 and 39.99 MHz

funddelay=-11.49./2; % in nS
seconddelay=-25.46./2; % in nS
thirddelay=-17.53./2; % in nS

phasedelayfundgnd=funddelay./75.*2.*pi;
phasedelay2ndgnd=seconddelay./37.5.*2.*pi;
phasedelay3rdgnd=thirddelay./25.*2.*pi;

% The fundemental current and voltage phase and magnitude are put into the
% data array

[data.waveforms.GNDelecCurrentPhase(1,:),data.waveforms.GNDelecCurrentMag(1,:)] = cart2pol(real(GNDIFundCor),imag(GNDIFundCor));
[data.waveforms.GNDelecVoltagePhase(1,:),data.waveforms.GNDelecVoltageMag(1,:)] = cart2pol(real(GNDVFundCor),imag(GNDVFundCor));
% pi is not subtracted from the phase so that current is defined as
%flowing in through the powered electrode and out through the grouded
%electrode

data.waveforms.GNDelecCurrentPhase(1,:)=data.waveforms.GNDelecCurrentPhase(1,:)+phasedelayfundgnd;

% The 2nd harmonic current and voltage phase and magnitude are put into the
% data array

[data.waveforms.GNDelecCurrentPhase(2,:),data.waveforms.GNDelecCurrentMag(2,:)] = cart2pol(real(GNDI2ndCor),imag(GNDI2ndCor));
```

```
[data.waveforms.GNDelecVoltagePhase(2,:),data.waveforms.GNDelecVoltageMag(2,:)] = cart2pol(real(GNDV2ndCor),imag(GNDV2ndCor));
% pi is not subtracted from the phase so that current is defined as
%flowing in through the powered electrode and out through the grouded
%electrode
data.waveforms.GNDelecCurrentPhase(2,:)=data.waveforms.GNDelecCurrentPhase(2,:)+phasedelay2ndgnd;

% The 3rd harmonic current and voltage phase and magnitude are put into the
% data array

[data.waveforms.GNDelecCurrentPhase(3,:),data.waveforms.GNDelecCurrentMag(3,:)] = cart2pol(real(GNDI3rdCor),imag(GNDI3rdCor));
[data.waveforms.GNDelecVoltagePhase(3,:),data.waveforms.GNDelecVoltageMag(3,:)] = cart2pol(real(GNDV3rdCor),imag(GNDV3rdCor));
% pi is not subtracted from the phase so that current is defined as
%flowing in through the powered electrode and out through the grouded
%electrode
data.waveforms.GNDelecCurrentPhase(3,:)=data.waveforms.GNDelecCurrentPhase(3,:)+phasedelay3rdgnd;

%% Subtracting the currnt through the grouded electrode from that through
% the power electrode gives the current through the chamber walls and
% electrode ground sheilds.

% REMEBER WE MUST USE THE CURRENT DEFINED AS FLOWWING INTO THE CHAMBER FROM
% THE POWERED ELECTRODE AND OUT THROUGH THE GOUNDED ELECTRODE AND CHAMBER
% WALLS

[PIfundreal,PIfundimag] = pol2cart(data.waveforms.PWRelecCurrentPhase(1,:),data.waveforms.PWRelecCurrentMag(1,:));
[PI2ndreal,PI2ndimag] = pol2cart(data.waveforms.PWRelecCurrentPhase(2,:),data.waveforms.PWRelecCurrentMag(2,:));
[PI3rdreal,PI3rdimag] = pol2cart(data.waveforms.PWRelecCurrentPhase(3,:),data.waveforms.PWRelecCurrentMag(3,:));

[GIfundreal,GIfundimag] = pol2cart(data.waveforms.GNDelecCurrentPhase(1,:),data.waveforms.GNDelecCurrentMag(1,:));
[GI2ndreal,GI2ndimag] = pol2cart(data.waveforms.GNDelecCurrentPhase(2,:),data.waveforms.GNDelecCurrentMag(2,:));
[GI3rdreal,GI3rdimag] = pol2cart(data.waveforms.GNDelecCurrentPhase(3,:),data.waveforms.GNDelecCurrentMag(3,:));

% The current is then calculated and saved into the data structure

wallIfundreal=PIfundreal-GIfundreal;
wallIfundimag=PIfundimag-GIfundimag;
wallI2ndreal=PI2ndreal-GI2ndreal;
wallI2ndimag=PI2ndimag-GI2ndimag;
wallI3rdreal=PI3rdreal-GI3rdreal;
wallI3rdimag=PI3rdimag-GI3rdimag;

[data.waveforms.WallelecCurrentPhase(1,:),data.waveforms.WallelecCurrentMag(1,:)] = cart2pol(wallIfundreal,wallIfundimag);
[data.waveforms.WallelecCurrentPhase(2,:),data.waveforms.WallelecCurrentMag(2,:)] = cart2pol(wallI2ndreal,wallI2ndimag);
[data.waveforms.WallelecCurrentPhase(3,:),data.waveforms.WallelecCurrentMag(3,:)] = cart2pol(wallI3rdreal,wallI3rdimag);

%% Finally power at each electrode and frequnecy is found

data.power.PWRelectrodeActive=zeros(3,length(PWRIFundCor));
data.power.PWRelectrodeReactive=zeros(3,length(PWRIFundCor));

% The powered electrode fundemental frequecy active power is
[IPhase,IMag] = cart2pol(real(PWRIFundCor),imag(PWRIFundCor));
[VPhase,VMag] = cart2pol(real(PWRVFundCor),imag(PWRVFundCor));
```

```
data.power.PWRelectrodeActive(1,:)=IMag.*VMag.*cos(VPhase-IPhase)./2;
% the reactive power is
data.power.PWRelectrodeReactive(1,:)=IMag.*VMag.*sin(VPhase-IPhase)./2;


% The powered electrode 2nd harmonic frequecy active power is
[IPhase,IMag] = cart2pol(real(PWRI2ndCor),imag(PWRI2ndCor));
[VPhase,VMag] = cart2pol(real(PWRV2ndCor),imag(PWRV2ndCor));
data.power.PWRelectrodeActive(2,:)=IMag.*VMag.*cos(VPhase-IPhase)./2;
% the reactive power is
data.power.PWRelectrodeReactive(2,:)=IMag.*VMag.*sin(VPhase-IPhase)./2;

% The powered electrode 3rd harmonic frequecy active power is
[IPhase,IMag] = cart2pol(real(PWRI3rdCor),imag(PWRI3rdCor));
[VPhase,VMag] = cart2pol(real(PWRV3rdCor),imag(PWRV3rdCor));
data.power.PWRelectrodeActive(3,:)=IMag.*VMag.*cos(VPhase-IPhase)./2;
% the reactive power is
data.power.PWRelectrodeReactive(3,:)=IMag.*VMag.*sin(VPhase-IPhase)./2;

% For the grounded electrode
data.power.GNDelectrodeActive=zeros(3,length(GNDIFundCor));
data.power.GNDelectrodeReactive=zeros(3,length(GNDIFundCor));

% The grounded electrode fundemental frequecy active power is
[IPhase,IMag] = cart2pol(real(GNDIFundCor),imag(GNDIFundCor));
[VPhase,VMag] = cart2pol(real(GNDVFundCor),imag(GNDVFundCor));
data.power.GNDelectrodeActive(1,:)=IMag.*VMag.*cos(VPhase-IPhase)./2;
% the reactive power is
data.power.GNDelectrodeReactive(1,:)=IMag.*VMag.*sin(VPhase-IPhase)./2;


% The grounded electrode 2nd harmonic frequecy active power is
[IPhase,IMag] = cart2pol(real(GNDI2ndCor),imag(GNDI2ndCor));
[VPhase,VMag] = cart2pol(real(GNDV2ndCor),imag(GNDV2ndCor));
data.power.GNDelectrodeActive(2,:)=IMag.*VMag.*cos(VPhase-IPhase)./2;
% the reactive power is
data.power.GNDelectrodeReactive(2,:)=IMag.*VMag.*sin(VPhase-IPhase)./2;

% The grounded electrode 3rd harmonic frequecy active power is
[IPhase,IMag] = cart2pol(real(GNDI3rdCor),imag(GNDI3rdCor));
[VPhase,VMag] = cart2pol(real(GNDV3rdCor),imag(GNDV3rdCor));
data.power.GNDelectrodeActive(3,:)=IMag.*VMag.*cos(VPhase-IPhase)./2;
% the reactive power is
data.power.GNDelectrodeReactive(3,:)=IMag.*VMag.*sin(VPhase-IPhase)./2;
```

B.2.13 RFIV_Waveform_Plotter

This function plots the powered and grounded electrode current and voltage waveforms and saves them in a folder created in the same folder where the .csv data files were located.

```
function [] = RFIV_Waveform_Plotter(data)

% This function plots the oscilliscope data waveform and then the waveform
% produced by each calculation step i.e. after the FFT or calibration
% correction. This is done for the PWR electrode I and V and the GND I. The
% GND electrode V is not measured as it is a small signal and so is not
% calculated until the parasitics impedances are taken into account and
% therefore only on GND V plot is made.

% The plotted waveforms are; Oscope data, FFT, probe calibration corrected,
% parasitic impedance corrected and finally propigation delay corrected.
set(groot,'DefaultAxesFontSize',20)
set(groot,'defaultTextInterpreter','latex');
set(groot,'DefaultAxesXGrid','on');
set(groot,'DefaultAxesYGrid','on');
set(groot,'DefaultAxesZGrid','on');

%% First PWR electrode current plots are made
Mag1=data.waveforms.PWRelecCurrentMag(1,:);
Mag2=data.waveforms.PWRelecCurrentMag(2,:);
Mag3=data.waveforms.PWRelecCurrentMag(3,:);

Phase1=data.waveforms.PWRelecCurrentPhase(1,:);
Phase2=data.waveforms.PWRelecCurrentPhase(2,:);
Phase3=data.waveforms.PWRelecCurrentPhase(3,:);

% The phases and magnitudes are linearly interprelated. This works well for
% smooth transitioning waveforms like those found after the matching
% network, but not well for quickly transition waveforms like those found
% after the amp with a 50 ohm load.

magint1=interp1(data.ChoppedTime,Mag1,data.TimeLong);
magint2=interp1(data.ChoppedTime,Mag2,data.TimeLong);
magint3=interp1(data.ChoppedTime,Mag3,data.TimeLong);

phaseint1=interp1(data.ChoppedTime,Phase1,data.TimeLong);
phaseint2=interp1(data.ChoppedTime,Phase2,data.TimeLong);
phaseint3=interp1(data.ChoppedTime,Phase3,data.TimeLong);

PWRIwave=magint1.*cos(data.Omega.*1.*data.TimeLong+phaseint1)+magint2.*cos(data.Omega.*2.*data.TimeLong+phaseint2)+...
magint3.*cos(data.Omega.*3.*data.TimeLong+phaseint3);
PWRIwave1=magint1.*cos(data.Omega.*1.*data.TimeLong+phaseint1);
PWRIwave2=magint2.*cos(data.Omega.*2.*data.TimeLong+phaseint2);
PWRIwave3=magint3.*cos(data.Omega.*3.*data.TimeLong+phaseint3);

figure
plot(data.TimeLong.*1000000,PWRIwave,data.TimeLong.*1000000,PWRIwave1,data.TimeLong.*1000000,PWRIwave2,data.TimeLong.*1000000,PWRIwave3)
title('Powered Electrode Current')
legend('Total','Fund','2nd','3rd')
xlabel('Time ($\mu$S)')
ylabel('Current (A)')
savetitlenew = strcat(data.savetitle,'\PWR I Waveform');
savefig(savetitlenew);
```

```
close all


%% Second PWR electrode voltage plots are made


Mag1=data.waveforms.PWRelecVoltageMag(1,:);
Mag2=data.waveforms.PWRelecVoltageMag(2,:);
Mag3=data.waveforms.PWRelecVoltageMag(3,:);

Phase1=data.waveforms.PWRelecVoltagePhase(1,:);
Phase2=data.waveforms.PWRelecVoltagePhase(2,:);
Phase3=data.waveforms.PWRelecVoltagePhase(3,:);

% The phases and magnitudes are linearly interprelated. This works well for
% smooth transitioning waveforms like those found after the matching
% network, but not well for quickly transition waveforms like those found
% after the amp with a 50 ohm load.

magint1=interp1(data.ChoppedTime,Mag1,data.TimeLong);
magint2=interp1(data.ChoppedTime,Mag2,data.TimeLong);
magint3=interp1(data.ChoppedTime,Mag3,data.TimeLong);

phaseint1=interp1(data.ChoppedTime,Phase1,data.TimeLong);
phaseint2=interp1(data.ChoppedTime,Phase2,data.TimeLong);
phaseint3=interp1(data.ChoppedTime,Phase3,data.TimeLong);


PWRVwave=magint1.*cos(data.Omega.*1.*data.TimeLong+phaseint1)+magint2.*cos(data.Omega.*2.*data.TimeLong+phaseint2)+...
magint3.*cos(data.Omega.*3.*data.TimeLong+phaseint3);
PWRVwave1=magint1.*cos(data.Omega.*1.*data.TimeLong+phaseint1);
PWRVwave2=magint2.*cos(data.Omega.*2.*data.TimeLong+phaseint2);
PWRVwave3=magint3.*cos(data.Omega.*3.*data.TimeLong+phaseint3);

figure
plot(data.TimeLong.*1000000,PWRVwave,data.TimeLong.*1000000,PWRVwave1,data.TimeLong.*1000000,PWRVwave2,data.TimeLong.*1000000,PWRVwave3)
title('Powered Electrode Voltage')
legend('Total','Fund','2nd','3rd')
xlabel('Time ($\mu$S)')
ylabel('Voltage (V)')
savetitlenew = strcat(data.savetitle,'\PWR V Waveform');
savefig(savetitlenew);

close all

% the DC and AC voltage waveforms are added together

figure
plot(data.TimeLong.*1000000,PWRVwave+data.DCdatanumsmooth)
title('Powered Electrode AC n DC Voltage')
%legend('Probe Cal','Parasitic Corected','Delay Corected')
xlabel('Time ($\mu$S)')
```

```
ylabel('Voltage (Volts)')
savetitlenew = strcat(data.savetitle,'\PWR V AC n DC Waveform');
savefig(savetitlenew);

close all



%% Third the GND electrode current plots are made


% next the paracitic impedance correction waveform is made

Mag1=data.waveforms.GNDelecCurrentMag(1,:);
Mag2=data.waveforms.GNDelecCurrentMag(2,:);
Mag3=data.waveforms.GNDelecCurrentMag(3,:);

Phase1=data.waveforms.GNDelecCurrentPhase(1,:);
Phase2=data.waveforms.GNDelecCurrentPhase(2,:);
Phase3=data.waveforms.GNDelecCurrentPhase(3,:);

% The phases and magnitudes are linearly interprelated. This works well for
% smooth transitioning waveforms like those found after the matching
% network, but not well for quickly transition waveforms like those found
% after the amp with a 50 ohm load.

magint1=interp1(data.ChoppedTime,Mag1,data.TimeLong);
magint2=interp1(data.ChoppedTime,Mag2,data.TimeLong);
magint3=interp1(data.ChoppedTime,Mag3,data.TimeLong);

phaseint1=interp1(data.ChoppedTime,Phase1,data.TimeLong);
phaseint2=interp1(data.ChoppedTime,Phase2,data.TimeLong);
phaseint3=interp1(data.ChoppedTime,Phase3,data.TimeLong);

GNDIwave=magint1.*cos(data.Omega.*1.*data.TimeLong+phaseint1)+magint2.*cos(data.Omega.*2.*data.TimeLong+phaseint2)+...
magint3.*cos(data.Omega.*3.*data.TimeLong+phaseint3);
GNDIwave1=magint1.*cos(data.Omega.*1.*data.TimeLong+phaseint1);
GNDIwave2=magint2.*cos(data.Omega.*2.*data.TimeLong+phaseint2);
GNDIwave3=magint3.*cos(data.Omega.*3.*data.TimeLong+phaseint3);

figure
plot(data.TimeLong.*1000000,GNDIwave,data.TimeLong.*1000000,GNDIwave1,data.TimeLong.*1000000,GNDIwave2,data.TimeLong.*1000000,GNDIwave3)
title('Grounded Electrode Current')
legend('Total','Fund','2nd','3rd')
xlabel('Time ($\mu$S)')
ylabel('Current (A)')

savetitlenew = strcat(data.savetitle,'\GND I Waveform');
savefig(savetitlenew);

close all

%%  the GND electrode voltage plot is made
```

```
% next the paracitic impedance correction waveform is made

Mag1=data.waveforms.GNDelecVoltageMag(1,:);
Mag2=data.waveforms.GNDelecVoltageMag(2,:);
Mag3=data.waveforms.GNDelecVoltageMag(3,:);

Phase1=data.waveforms.GNDelecVoltagePhase(1,:);
Phase2=data.waveforms.GNDelecVoltagePhase(2,:);
Phase3=data.waveforms.GNDelecVoltagePhase(3,:);

% The phases and magnitudes are linearly interprelated. This works well for
% smooth transitioning waveforms like those found after the matching
% network, but not well for quickly transition waveforms like those found
% after the amp with a 50 ohm load.

magint1=interp1(data.ChoppedTime,Mag1,data.TimeLong);
magint2=interp1(data.ChoppedTime,Mag2,data.TimeLong);
magint3=interp1(data.ChoppedTime,Mag3,data.TimeLong);

phaseint1=interp1(data.ChoppedTime,Phase1,data.TimeLong);
phaseint2=interp1(data.ChoppedTime,Phase2,data.TimeLong);
phaseint3=interp1(data.ChoppedTime,Phase3,data.TimeLong);

GNDVwave=magint1.*cos(data.Omega.*1.*data.TimeLong+phaseint1)+magint2.*cos(data.Omega.*2.*data.TimeLong+phaseint2)+...
magint3.*cos(data.Omega.*3.*data.TimeLong+phaseint3);
GNDVwave1=magint1.*cos(data.Omega.*1.*data.TimeLong+phaseint1);
GNDVwave2=magint2.*cos(data.Omega.*2.*data.TimeLong+phaseint2);
GNDVwave3=magint3.*cos(data.Omega.*3.*data.TimeLong+phaseint3);

figure
plot(data.TimeLong.*1000000,GNDVwave,data.TimeLong.*1000000,GNDVwave1,data.TimeLong.*1000000,GNDVwave2,data.TimeLong.*1000000,GNDVwave3)
title('Grounded Electrode Voltage')
legend('Total','Fund','2nd','3rd')
xlabel('Time ($\mu$S)')
ylabel('Voltage (V)')

savetitlenew = strcat(data.savetitle,'\GND V Waveform');
savefig(savetitlenew);

close all


%% The Chamber Wall current plots are made


% next the paracitic impedance correction waveform is made

Mag1=data.waveforms.WallelecCurrentMag(1,:);
Mag2=data.waveforms.WallelecCurrentMag(2,:);
Mag3=data.waveforms.WallelecCurrentMag(3,:);

Phase1=data.waveforms.WallelecCurrentPhase(1,:);
```

```
Phase2=data.waveforms.WallelecCurrentPhase(2,:);
Phase3=data.waveforms.WallelecCurrentPhase(3,:);

% The phases and magnitudes are linearly interprelated. This works well for
% smooth transitioning waveforms like those found after the matching
% network, but not well for quickly transition waveforms like those found
% after the amp with a 50 ohm load.

magint1=interp1(data.ChoppedTime,Mag1,data.TimeLong);
magint2=interp1(data.ChoppedTime,Mag2,data.TimeLong);
magint3=interp1(data.ChoppedTime,Mag3,data.TimeLong);

phaseint1=interp1(data.ChoppedTime,Phase1,data.TimeLong);
phaseint2=interp1(data.ChoppedTime,Phase2,data.TimeLong);
phaseint3=interp1(data.ChoppedTime,Phase3,data.TimeLong);


WallIwave=magint1.*cos(data.Omega.*1.*data.TimeLong+phaseint1)+magint2.*cos(data.Omega.*2.*data.TimeLong+phaseint2)+...
magint3.*cos(data.Omega.*3.*data.TimeLong+phaseint3);
WallIwave1=magint1.*cos(data.Omega.*1.*data.TimeLong+phaseint1);
WallIwave2=magint2.*cos(data.Omega.*2.*data.TimeLong+phaseint2);
WallIwave3=magint3.*cos(data.Omega.*3.*data.TimeLong+phaseint3);

figure
plot(data.TimeLong.*1000000,WallIwave,data.TimeLong.*1000000,WallIwave1,data.TimeLong.*1000000,WallIwave2,data.TimeLong.*1000000,WallIwave3)
title('Chamber Wall Current')
legend('Total','Fund','2nd','3rd')
xlabel('Time ($\mu$S)')
ylabel('Current (A)')

savetitlenew = strcat(data.savetitle,'\Wall I Waveform');
savefig(savetitlenew);


%% The DC bias is plotted

figure
plot(data.TimeLong.*1000000,data.DCdatanum)
title('DC Bias Voltage')
xlabel('Time ($\mu$S)')
ylabel('Voltage (Volts)')

savetitlenew = strcat(data.savetitle,'\DC Bias');
savefig(savetitlenew);

close all
```

B.2.14 RFIV_Plotter

This function plots all of the non waveform data and saves them in a folder created in the same folder where the .csv data files were located.

```
function [] = RFIV_Plotter(data)

% This function plots the FFT derived values and plasma impedance

%% First PWR electrode current plots are made

% The FFT derived magnitudes

FFTMag1=data.PWRIFFT{1, 2}(2,:);
FFTMag2=data.PWRIFFT{1, 2}(3,:);
FFTMag3=data.PWRIFFT{1, 2}(4,:);

% The probe calibration magnitudes

probeMag1=data.PWRIcalMagFFT(1,:);
probeMag2=data.PWRIcalMagFFT(2,:);
probeMag3=data.PWRIcalMagFFT(3,:);

% The parasitic corrected magnitudes

paraMag1=data.waveforms.PWRelecCurrentMag(1,:);
paraMag2=data.waveforms.PWRelecCurrentMag(2,:);
paraMag3=data.waveforms.PWRelecCurrentMag(3,:);

figure
plot(data.ChoppedTime.*1000000,FFTMag1,data.ChoppedTime.*1000000,probeMag1,data.ChoppedTime.*1000000,paraMag1)
title('Powered Electrode Fund Current Mag')
legend('FFT','Probe Cal','Parasitic Corrected')
xlabel('Time ($\mu$S)')
ylabel('Current (A)')
savetitlenew = strcat(data.savetitle,'\PWR I Fund Mag');
savefig(savetitlenew);

figure
plot(data.ChoppedTime.*1000000,FFTMag2,data.ChoppedTime.*1000000,probeMag2,data.ChoppedTime.*1000000,paraMag2)
title('Powered Electrode 2nd Har Current Mag')
legend('FFT','Probe Cal','Parasitic Corrected')
xlabel('Time ($\mu$S)')
ylabel('Current (A)')
savetitlenew = strcat(data.savetitle,'\PWR I 2nd Har Mag');
savefig(savetitlenew);

figure
plot(data.ChoppedTime.*1000000,FFTMag3,data.ChoppedTime.*1000000,probeMag3,data.ChoppedTime.*1000000,paraMag3)
title('Powered Electrode 3rd Har Current Mag')
legend('FFT','Probe Cal','Parasitic Corrected')
xlabel('Time ($\mu$S)')
ylabel('Current (A)')
savetitlenew = strcat(data.savetitle,'\PWR I 3rd Har Mag');
savefig(savetitlenew);

figure
plot(data.ChoppedTime.*1000000,paraMag1,data.ChoppedTime.*1000000,paraMag2,data.ChoppedTime.*1000000,paraMag3)
```

```
title('Powered Electrode Corrected Current Mag')
legend('Fund','2nd','3rd')
xlabel('Time ($\mu$S)')
ylabel('Current (A)')
savetitlenew = strcat(data.savetitle,'\PWR I Mags');
savefig(savetitlenew);

%% second PWR electrode voltage plots are made

% The FFT derived magnitudes

FFTMag1=data.PWRVFFT{1, 2}(2,:);
FFTMag2=data.PWRVFFT{1, 2}(3,:);
FFTMag3=data.PWRVFFT{1, 2}(4,:);

% The probe calibration magnitudes

probeMag1=data.PWRVcalMagFFT(1,:);
probeMag2=data.PWRVcalMagFFT(2,:);
probeMag3=data.PWRVcalMagFFT(3,:);

% The parasitic corrected magnitudes

paraMag1=data.waveforms.PWRelecVoltageMag(1,:);
paraMag2=data.waveforms.PWRelecVoltageMag(2,:);
paraMag3=data.waveforms.PWRelecVoltageMag(3,:);

figure
plot(data.ChoppedTime.*1000000,FFTMag1,data.ChoppedTime.*1000000,probeMag1,data.ChoppedTime.*1000000,paraMag1)
title('Powered Electrode Fund Voltage Mag')
legend('FFT','Probe Cal','Parasitic Corrected')
xlabel('Time ($\mu$S)')
ylabel('Voltage (Volts)')
savetitlenew = strcat(data.savetitle,'\PWR V Fund Mag');
savefig(savetitlenew);

figure
plot(data.ChoppedTime.*1000000,FFTMag2,data.ChoppedTime.*1000000,probeMag2,data.ChoppedTime.*1000000,paraMag2)
title('Powered Electrode 2nd Har Voltage Mag')
legend('FFT','Probe Cal','Parasitic Corrected')
xlabel('Time ($\mu$S)')
ylabel('Voltage (Volts)')
savetitlenew = strcat(data.savetitle,'\PWR V 2nd Har Mag');
savefig(savetitlenew);

figure
plot(data.ChoppedTime.*1000000,FFTMag3,data.ChoppedTime.*1000000,probeMag3,data.ChoppedTime.*1000000,paraMag3)
title('Powered Electrode 3rd Har Voltage Mag')
legend('FFT','Probe Cal','Parasitic Corrected')
xlabel('Time ($\mu$S)')
ylabel('Voltage (Volts)')
savetitlenew = strcat(data.savetitle,'\PWR V 3rd Har Mag');
savefig(savetitlenew);
```

```
figure
%plot(data.ChoppedTime,paraMag1,data.ChoppedTime,paraMag2,data.ChoppedTime,paraMag3)
plot(data.ChoppedTime.*1000000,paraMag1,data.ChoppedTime.*1000000,paraMag2,data.ChoppedTime.*1000000,paraMag3)
title('Powered Electrode Corrected Voltage Mag')
legend('Fund','2nd','3rd')
xlabel('Time ($\mu$S)')
ylabel('Voltage (Volts)')
savetitlenew = strcat(data.savetitle,'\PWR V Mags');
savefig(savetitlenew);

%% third GND electrode current plots are made

% The FFT derived magnitudes

FFTMag1=data.GNDIFFT{1, 2}(2,:);
FFTMag2=data.GNDIFFT{1, 2}(3,:);
FFTMag3=data.GNDIFFT{1, 2}(4,:);

% The probe calibration magnitudes

probeMag1=data.GNDIcalMagFFT(1,:);
probeMag2=data.GNDIcalMagFFT(2,:);
probeMag3=data.GNDIcalMagFFT(3,:);

% The parasitic corrected magnitudes

paraMag1=data.waveforms.GNDelecCurrentMag(1,:);
paraMag2=data.waveforms.GNDelecCurrentMag(2,:);
paraMag3=data.waveforms.GNDelecCurrentMag(3,:);

figure
plot(data.ChoppedTime.*1000000,FFTMag1,data.ChoppedTime.*1000000,probeMag1,data.ChoppedTime.*1000000,paraMag1)
title('Grounded Electrode Fund Current Mag')
legend('FFT','Probe Cal','Parasitic Corrected')
xlabel('Time ($\mu$S)')
ylabel('Current (A)')
savetitlenew = strcat(data.savetitle,'\GND I Fund Mag');
savefig(savetitlenew);

figure
plot(data.ChoppedTime.*1000000,FFTMag2,data.ChoppedTime.*1000000,probeMag2,data.ChoppedTime.*1000000,paraMag2)
title('Grounded Electrode 2nd Har Current Mag')
legend('FFT','Probe Cal','Parasitic Corrected')
xlabel('Time ($\mu$S)')
ylabel('Current (A)')
savetitlenew = strcat(data.savetitle,'\GND I 2nd Har Mag');
savefig(savetitlenew);

figure
plot(data.ChoppedTime.*1000000,FFTMag3,data.ChoppedTime.*1000000,probeMag3,data.ChoppedTime.*1000000,paraMag3)
title('Grounded Electrode 3rd Har Current Mag')
legend('FFT','Probe Cal','Parasitic Corrected')
```

```
xlabel('Time ($\mu$S)')
ylabel('Current (A)')
savetitlenew = strcat(data.savetitle,'\GND I 3rd Har Mag');
savefig(savetitlenew);

figure
plot(data.ChoppedTime.*1000000,paraMag1,data.ChoppedTime.*1000000,paraMag2,data.ChoppedTime.*1000000,paraMag3)
title('Grounded Electrode Corrected Current Mag')
legend('Fund','2nd','3rd')
xlabel('Time ($\mu$S)')
ylabel('Current (A)')
savetitlenew = strcat(data.savetitle,'\GND I Mags');
savefig(savetitlenew);

%% fourth GND electrode voltage plots are made

% The parasitic corrected magnitudes

paraMag1=data.waveforms.GNDelecVoltageMag(1,:);
paraMag2=data.waveforms.GNDelecVoltageMag(2,:);
paraMag3=data.waveforms.GNDelecVoltageMag(3,:);

figure
plot(data.ChoppedTime.*1000000,paraMag1,data.ChoppedTime.*1000000,paraMag2,data.ChoppedTime.*1000000,paraMag3)
title('Grounded Electrode Corrected Voltage Mag')
legend('Fund','2nd','3rd')
xlabel('Time ($\mu$S)')
ylabel('Voltage (Volts)')
savetitlenew = strcat(data.savetitle,'\GND V Mags');
savefig(savetitlenew);

%% Chamber wall currents are plotted

% The parasitic corrected magnitudes

paraMag1=data.waveforms.WallelecCurrentMag(1,:);
paraMag2=data.waveforms.WallelecCurrentMag(2,:);
paraMag3=data.waveforms.WallelecCurrentMag(3,:);

figure
plot(data.ChoppedTime.*1000000,paraMag1,data.ChoppedTime.*1000000,paraMag2...
,data.ChoppedTime.*1000000,paraMag3)
title('Chamber Wall Electrode Corrected Current Mag')
legend('Fund','2nd','3rd')
xlabel('Time ($\mu$S)')
ylabel('Current (A)')
savetitlenew = strcat(data.savetitle,'\Wall I Mags');
savefig(savetitlenew);

%% power at both electrodes for all three frequencies is ploted

%{
% plot  PWR electrode phase diff in degrees
```

```
figure
plot(data.ChoppedTime.*1000000,rad2deg(data.PhaseDiff1PrbCal),data.ChoppedTime.*1000000...
,rad2deg(data.PhaseDiff2PrbCal),data.ChoppedTime.*1000000,rad2deg(data.PhaseDiff3PrbCal))
title('Powered Electrode Phase Difference Probe Cal')
legend('Fund','2nd','3rd')
xlabel('Time ($\mu$S)')
ylabel('Phase (Degrees)')
savetitlenew = strcat(data.savetitle,'\PWR phase diffs Probe Cal');
savefig(savetitlenew);

% plot PWR electrode power

figure
plot(data.ChoppedTime.*1000000,data.PWRFPrbCal,data.ChoppedTime.*1000000...
,data.PWR2ndPrbCal,data.ChoppedTime.*1000000,data.PWR3rdPrbCal)
title('Powered Electrode Power Probe Cal')
legend('Fund','2nd','3rd')
xlabel('Time ($\mu$S)')
ylabel('Power (Watts)')
savetitlenew = strcat(data.savetitle,'\PWR powers Probe Cal');
savefig(savetitlenew);



% parasitic impedance corrected

figure
plot(data.ChoppedTime.*1000000,rad2deg(data.PhaseDiff1ParaCor)...
,data.ChoppedTime.*1000000,rad2deg(data.PhaseDiff2ParaCor)...
,data.ChoppedTime.*1000000,rad2deg(data.PhaseDiff3ParaCor))
title('Powered Electrode Phase Difference Parasitics Corrected')
legend('Fund','2nd','3rd')
xlabel('Time ($\mu$S)')
ylabel('Phase (Degrees)')
savetitlenew = strcat(data.savetitle,'\PWR phase diffs Para Cor');
savefig(savetitlenew);
%}

% plot PWR active electrode power

figure
plot(data.ChoppedTime.*1000000,data.power.PWRelectrodeActive(1,:)...
,data.ChoppedTime.*1000000,data.power.PWRelectrodeActive(2,:)...
,data.ChoppedTime.*1000000,data.power.PWRelectrodeActive(3,:))
title('Powered Electrode Active Power')
legend('Fund','2nd','3rd')
xlabel('Time ($\mu$S)')
ylabel('Power (Watts)')
savetitlenew = strcat(data.savetitle,'\Active Power PWR electrode');
savefig(savetitlenew);

% plot PWR reactive electrode power
```

```
figure
plot(data.ChoppedTime.*1000000,data.power.PWRelectrodeReactive(1,:)...
,data.ChoppedTime.*1000000,data.power.PWRelectrodeReactive(2,:)...
,data.ChoppedTime.*1000000,data.power.PWRelectrodeReactive(3,:))
title('Powered Electrode Reactive Power')
legend('Fund','2nd','3rd')
xlabel('Time ($\mu$S)')
ylabel('Power (Watts)')
savetitlenew = strcat(data.savetitle,'\Reactive Power PWR electrode');
savefig(savetitlenew);

% grounded electrode

% plot PWR electrode power
% plot PWR active electrode power

figure
plot(data.ChoppedTime.*1000000,data.power.GNDelectrodeActive(1,:)...
,data.ChoppedTime.*1000000,data.power.GNDelectrodeActive(2,:)...
,data.ChoppedTime.*1000000,data.power.GNDelectrodeActive(3,:))
title('Grounded Electrode Active Power')
legend('Fund','2nd','3rd')
xlabel('Time ($\mu$S)')
ylabel('Power (Watts)')
savetitlenew = strcat(data.savetitle,'\Active Power GND electrode');
savefig(savetitlenew);

% plot PWR reactive electrode power

figure
plot(data.ChoppedTime.*1000000,data.power.GNDelectrodeReactive(1,:)...
,data.ChoppedTime.*1000000,data.power.GNDelectrodeReactive(2,:)...
,data.ChoppedTime.*1000000,data.power.GNDelectrodeReactive(3,:))
title('Grounded Electrode Active Power')
legend('Fund','2nd','3rd')
xlabel('Time ($\mu$S)')
ylabel('Power (Watts)')
savetitlenew = strcat(data.savetitle,'\Reactive Power GND electrode');
savefig(savetitlenew);

%% plot impedance

figure
plot(data.ChoppedTime.*1000000,real(data.impedance.Zplasma))
title('Plasma Input Resistance')
xlabel('Time ($\mu$S)')
ylabel('Resistance ($\Omega$)')
savetitlenew = strcat(data.savetitle,'\Plasma Input Resistance');
savefig(savetitlenew);

figure
plot(data.ChoppedTime.*1000000,imag(data.impedance.Zplasma))
title('Plasma Input Reactance')
```

```
xlabel('Time ($\mu$S)')
ylabel('Reactance ($\Omega$)')
savetitlenew = strcat(data.savetitle,'\Plasma Input Reactance');
savefig(savetitlenew);

close all
```

B.3 SymVsAntisymWaveform_9_24_2019.m

This function requires that the RFIV data file which was created by RFIV_Read_in_Data.m is in the MATLAB workspace. This can be done by dragging the file over the workspace area. The user must select the time period in which they want to look at by setting T="time period" in nanoseconds. The program will then separate the sheath voltages from total voltage, and the even (conduction) and odd (displacement) current. Only works at steady stat and can have large errors in transition regions.

```
%close all


set(groot,'DefaultAxesFontSize',20)
set(groot,'DefaultAxesXGrid','on');
set(groot,'DefaultAxesYGrid','on');
set(groot,'DefaultAxesZGrid','on');
set(groot,'defaulttextinterpreter','latex');
set(groot, 'defaultAxesTickLabelInterpreter','latex');
set(groot, 'defaultLegendInterpreter','latex');

xlimstart=3.9;
xlimend=4.05;

%
xlimstart=-inf;
xlimend=inf;
%}

data=RFIVdata;

delaypointsPWR=85;
delayPointsWall=135;
delaypointsGND=0;

% selected time period in ns
T=1150;
T=30150;

rfperiod=75e-9;
```

```
% convert selected time into integer of an rf period
n=floor(T./75);
% number of points in the section
npoints=5.*1e4+1; %1e4 gives 7.5 ps resolution

%% Powered Electrode

% make current waveform

Mag1=data.waveforms.PWRelecCurrentMag(1,n);
Mag2=data.waveforms.PWRelecCurrentMag(2,n);
Mag3=data.waveforms.PWRelecCurrentMag(3,n);

Phase1=data.waveforms.PWRelecCurrentPhase(1,n)-2.*pi.*0.65./75.*0;
Phase2=data.waveforms.PWRelecCurrentPhase(2,n)-2.*pi.*0.65./37.5.*0;
Phase3=data.waveforms.PWRelecCurrentPhase(3,n)-2.*pi.*0.65./25.*0;

timestamp=data.ChoppedTime(n);

% build the current vector with 5 identical rf periods

timestart=data.ChoppedTime(n)-rfperiod.*2.5;
timeend=data.ChoppedTime(n)+rfperiod.*2.5;
timevector=linspace(timestart,timeend,npoints);

PWRIFund=Mag1.*cos(RFIVdata.Omega.*1.*timevector+Phase1);
PWRI2nd=Mag2.*cos(RFIVdata.Omega.*2.*timevector+Phase2);
PWRI3rd=Mag3.*cos(RFIVdata.Omega.*3.*timevector+Phase3);

PWRI=PWRIFund+PWRI2nd+PWRI3rd;

% make voltage waveform

Mag1=data.waveforms.PWRelecVoltageMag(1,n);
Mag2=data.waveforms.PWRelecVoltageMag(2,n);
Mag3=data.waveforms.PWRelecVoltageMag(3,n);

Phase1=data.waveforms.PWRelecVoltagePhase(1,n);
Phase2=data.waveforms.PWRelecVoltagePhase(2,n);
Phase3=data.waveforms.PWRelecVoltagePhase(3,n);

PWRVFund=Mag1.*cos(RFIVdata.Omega.*1.*timevector+Phase1);
PWRV2nd=Mag2.*cos(RFIVdata.Omega.*2.*timevector+Phase2);
PWRV3rd=Mag3.*cos(RFIVdata.Omega.*3.*timevector+Phase3);

PWRV=PWRVFund+PWRV2nd+PWRV3rd;

%% Grounded Electrode

% make current waveform

Mag1=data.waveforms.GNDelecCurrentMag(1,n);
Mag2=data.waveforms.GNDelecCurrentMag(2,n);
```

```
Mag3=data.waveforms.GNDelecCurrentMag(3,n);

Phase1=data.waveforms.GNDelecCurrentPhase(1,n);
Phase2=data.waveforms.GNDelecCurrentPhase(2,n);
Phase3=data.waveforms.GNDelecCurrentPhase(3,n);

% build the current vector with 5 identical rf periods

GNDIFund=Mag1.*cos(RFIVdata.Omega.*1.*timevector+Phase1);
GNDI2nd=Mag2.*cos(RFIVdata.Omega.*2.*timevector+Phase2);
GNDI3rd=Mag3.*cos(RFIVdata.Omega.*3.*timevector+Phase3);

GNDI=GNDIFund+GNDI2nd+GNDI3rd;

% make voltage waveform

Mag1=data.waveforms.GNDelecVoltageMag(1,n);
Mag2=data.waveforms.GNDelecVoltageMag(2,n);
Mag3=data.waveforms.GNDelecVoltageMag(3,n);

Phase1=data.waveforms.GNDelecVoltagePhase(1,n);
Phase2=data.waveforms.GNDelecVoltagePhase(2,n);
Phase3=data.waveforms.GNDelecVoltagePhase(3,n);

GNDVFund=Mag1.*cos(RFIVdata.Omega.*1.*timevector+Phase1);
GNDV2nd=Mag2.*cos(RFIVdata.Omega.*2.*timevector+Phase2);
GNDV3rd=Mag3.*cos(RFIVdata.Omega.*3.*timevector+Phase3);

GNDV=GNDVFund+GNDV2nd+GNDV3rd;

%% Chamber Wall

% make current waveform

Mag1=data.waveforms.WallelecCurrentMag(1,n);
Mag2=data.waveforms.WallelecCurrentMag(2,n);
Mag3=data.waveforms.WallelecCurrentMag(3,n);



Phase1=data.waveforms.WallelecCurrentPhase(1,n);
Phase2=data.waveforms.WallelecCurrentPhase(2,n);
Phase3=data.waveforms.WallelecCurrentPhase(3,n);

% build the current vector with 5 identical rf periods

WALLIFund=Mag1.*cos(RFIVdata.Omega.*1.*timevector+Phase1);
WALLI2nd=Mag2.*cos(RFIVdata.Omega.*2.*timevector+Phase2);
WALLI3rd=Mag3.*cos(RFIVdata.Omega.*3.*timevector+Phase3);

WALLI=WALLIFund+WALLI2nd+WALLI3rd;

%% Seperate Voltages
```

```
Vmax=max(PWRV-GNDV);
Vmin=min(PWRV-GNDV);

% find corisponding DC bias values during the rf period
DCtimestart=timestamp-rfperiod.*0.5;
DCtimeend=timestamp+rfperiod.*0.5;
DCtimestartIndex = find(data.TimeLong>=DCtimestart,1);
DCtimeendIndex = find(data.TimeLong>=DCtimeend,1);
DCinrfperiod=data.DCdatanum(DCtimestartIndex :DCtimeendIndex);
DCave=mean(DCinrfperiod);

% find the symetry parameter
Sym=-(Vmax+DCave)./(Vmin+DCave);


%Find the voltage to the chamber wall

% find the voltage max

maxfund=max(PWRVFund);
max2nd=max(PWRV2nd);
max3rd=max(PWRV3rd);
Utot=maxfund+max2nd+max3rd;

DCcalcnorm=DCave./Utot;
SystemV_Wall=PWRV;
SystemVnorm=SystemV_Wall./Utot;

qt=sqrt((Vmax-Vmin)./((1+Sym).*Utot));
qOFt=-Sym.*qt+sqrt(Sym.*qt.^2-(1-Sym).*(DCcalcnorm+SystemVnorm))./(1-Sym);

PWRsheath_Wall=-qOFt.^2.*Utot;
WALLsheath=Sym.*(qt-qOFt).^2.*Utot;
bulkV_Wall=SystemV_Wall-PWRsheath_Wall-WALLsheath+DCave;

pwrsurface_Wall=SystemV_Wall+DCave;
pwrsheath_bulk_Wall=pwrsurface_Wall-PWRsheath_Wall;
bulk_WALLsheath_Wall=pwrsheath_bulk_Wall-bulkV_Wall;
gndsurface_Wall=bulk_WALLsheath_Wall-WALLsheath;
bulkcenter_Wall=(pwrsheath_bulk_Wall+bulk_WALLsheath_Wall)./2;

% Find the voltage to the grounded electrode

maxfund=max(PWRVFund-GNDVFund);
max2nd=max(PWRV2nd-GNDV2nd);
max3rd=max(PWRV3rd-GNDV3rd);
Utot=maxfund+max2nd+max3rd;

DCcalcnorm=DCave./Utot;
SystemV_GNDe=PWRV-GNDV;
SystemVnorm=SystemV_GNDe./Utot;

qt=sqrt((Vmax-Vmin)./((1+Sym).*Utot));
```

```
qOFt=-Sym.*qt+sqrt(Sym.*qt.^2-(1-Sym).*(DCcalcnorm+SystemVnorm))./(1-Sym);

PWRsheath_GNDe=-qOFt.^2.*Utot;
GNDsheath=Sym.*(qt-qOFt).^2.*Utot;
bulkV_GNDe=SystemV_GNDe-PWRsheath_GNDe-GNDsheath+DCave;

pwrsurface_GNDe=PWRV+DCave;
pwrsheath_bulk_GNDe=pwrsurface_GNDe-PWRsheath_GNDe;
bulk_gndsheath_GNDe=pwrsheath_bulk_GNDe-bulkV_GNDe;
gndsurface_GNDe=bulk_gndsheath_GNDe-GNDsheath;
bulkcenter_GNDe=(pwrsheath_bulk_GNDe+bulk_gndsheath_GNDe)./2;

%% Powered Electrode Calculations

% find maximum voltage position of middle waveforms

[M,I]=findpeaks(PWRsheath_GNDe);
midpoint=I(3)-delaypointsPWR;

% take the three rf periods around the midpoint
Startpoint=midpoint-npoints.*0.3;
Endpoint=midpoint+npoints.*0.3;

timepartPWR=timevector(Startpoint:Endpoint);
PWRSHEATH=PWRsheath_GNDe(Startpoint:Endpoint);
PWRIreduc=PWRI(Startpoint:Endpoint);

FlippedPWRI=flip(PWRIreduc);
xePWRI=0.5*(FlippedPWRI+PWRIreduc);
xoPWRI=0.5*(PWRIreduc-FlippedPWRI);

%% Chamber Wall Calculations

% find minimum voltage position of middle waveform

[M,I]=findpeaks(-1.*PWRsheath_Wall);
midpoint=I(3)-delayPointsWall;

% take the three rf periods around the midpoint
Startpoint=midpoint-npoints.*0.3;
Endpoint=midpoint+npoints.*0.3;

timepartWALL=timevector(Startpoint:Endpoint);
wallSHEATH=WALLsheath(Startpoint:Endpoint);
WALLIreduc=WALLI(Startpoint:Endpoint);
FlippedWallI=flip(WALLIreduc);
xeWALLI=0.5*(FlippedWallI+WALLIreduc);
xoWALLI=0.5*(WALLIreduc-FlippedWallI);


%% Grounded Electrode Calculations

% find minimum voltage position of middle waveform
```

```
[M,I]=findpeaks(-1.*PWRsheath_Wall);
midpoint=I(3)-delaypointsGND;
% take the three rf periods around the midpoint
Startpoint=midpoint-npoints.*0.3;
Endpoint=midpoint+npoints.*0.3;

timepartGND=timevector(Startpoint:Endpoint);
gndsheath=GNDsheath(Startpoint:Endpoint);
GNDIreduc=GNDI(Startpoint:Endpoint);



FlippedGNDI=flip(GNDIreduc);
xeGNDI=0.5*(FlippedGNDI+GNDIreduc);
xoGNDI=0.5*(GNDIreduc-FlippedGNDI);

%{
% voltage figures powered electrode to chamber wall
figure
hold on
plot(timevector.*1e6,SystemV_Wall+DCave,'-k','LineWidth',1)
plot(timevector.*1e6,PWRsheath_Wall,'--k','LineWidth',1)
plot(timevector.*1e6,WALLsheath,'-.k','LineWidth',1)
plot(timevector.*1e6,bulkV_Wall,':k','LineWidth',1)
xlim([xlimstart xlimend])
legend('$V_{pp}$','$V_{pps}$','$V_{pws}$','$V_{b}$')
title('PWR Electrode to Chamber Wall')




figure
hold on
plot(timevector.*1e6,pwrsurface_Wall,'-k','LineWidth',1)
plot(timevector.*1e6,pwrsheath_bulk_Wall,'--k','LineWidth',1)
plot(timevector.*1e6,bulk_WALLsheath_Wall,'-.k','LineWidth',1)
plot(timevector.*1e6,bulkcenter_Wall,':k','LineWidth',1)
%plot(timevector.*1e6,gndsurface_Wall,'--k','LineWidth',1)
legend('$V_{pp}$','$V_{pps-b}$','$V_{b-pws}$','$V_{p}$')
title('PWR Electrode to Chamber Wall')
xlim([xlimstart xlimend])
%}

%
% plot PWR Electrode V and I
figure
hold on
plot(timepartPWR.*1e6,PWRSHEATH,'-k','LineWidth',2)
ylabel('Voltage (V)')
yyaxis left
yyaxis right
plot(timepartPWR.*1e6,xePWRI,'--k','LineWidth',1)
```

```
plot(timepartPWR.*1e6,xoPWRI,'-.k','LineWidth',1)
plot(timepartPWR.*1e6,PWRIreduc,':k','LineWidth',1)

ylabel('Current (A)')
xlabel('Time $(\mu S)$')
legend('$V_{pps}$','$I_{pp\ con}$','$I_{pp\ dis}$','$I_{pp}$')
title('Powered Electrode')
xlim([xlimstart xlimend])
%}


%{
% plot Chamber Wall V and I
figure
hold on
plot(timepartWALL.*1e6,wallSHEATH,'-k','LineWidth',2)
ylabel('Voltage (V)')
yyaxis left
yyaxis right
plot(timepartWALL.*1e6,xeWALLI,'--k','LineWidth',1)
plot(timepartWALL.*1e6,xoWALLI,'-.k','LineWidth',1)
plot(timepartWALL.*1e6,WALLIreduc,':k','LineWidth',1)

ylabel('Current (A)')
xlabel('Time $(\mu S)$')
legend('$V_{pws}$','$I_{pw\ con}$','$I_{pw\ dis}$','$I_{pw}$')
title('Chamber Wall')
xlim([xlimstart xlimend])
%}

%
% plot grounded electrode V and I
figure
hold on
plot(timepartGND.*1e6,gndsheath,'-k','LineWidth',2)
ylabel('Voltage (V)')
yyaxis left
yyaxis right
plot(timepartGND.*1e6,xeGNDI,'--k','LineWidth',1)
plot(timepartGND.*1e6,xoGNDI,'-.k','LineWidth',1)
plot(timepartGND.*1e6,GNDIreduc,':k','LineWidth',1)

ylabel('Current (A)')
xlabel('Time $(\mu S)$')
legend('$V_{pgs}$','$I_{pg\ con}$','$I_{pg\ dis}$','$I_{pg}$')
title('Grounded Electrode')
xlim([xlimstart xlimend])
%}

%{
% voltage figures powered electrode to grounded electrode
figure
plot(timevector.*1e6,SystemV_GNDe+DCave,timevector.*1e6,PWRsheath_GNDe,timevector.*1e6,GNDsheath,timevector.*1e6,bulkV_GNDe)
```

```
legend('total','PWR','GND','Bulk')
title('PWR Electrode to GND Electrode')
xlim([xlimstart xlimend])

figure
hold on
plot(timevector.*1e6,pwrsurface_GNDe)
plot(timevector.*1e6,pwrsheath_bulk_GNDe)
plot(timevector.*1e6,bulk_gndsheath_GNDe)
plot(timevector.*1e6,GNDV)
plot(timevector.*1e6,bulkcenter_GNDe)
legend('pwrsurface','pwrsheath bulk','bulk gndsheath','gndsurface','bulkcenter')
title('PWR Electrode to GND Electrode')
xlim([xlimstart xlimend])
%}
```

REFERENCES

Allen, J., R. Boyd, and P. Reynolds (1957). The collection of positive ions by a probe immersed in a plasma. *Proceedings of the Physical Society. Section B 70*(3), 297.

Ashida, S., C. Lee, and M. Lieberman (1995). Spatially averaged (global) model of time modulated high density argon plasmas. *Journal of Vacuum Science & Technology A: Vacuum, Surfaces, and Films 13*(5), 2498–2507.

Banna, S., A. Agarwal, G. Cunge, M. Darnon, E. Pargon, and O. Joubert (2012). Pulsed high-density plasmas for advanced dry etching processes. *Journal of Vacuum Science & Technology A: Vacuum, Surfaces, and Films 30*(4), 040801.

Banner, S., V. Todorow, and K. Ramaswamy (2012, September 11). Method and apparatus for pulsed plasma processing using a time resolved tuning scheme for rf power delivery. US Patent 8,264,154.

Beneking, C. (1990). Power dissipation in capacitively coupled rf discharges. *Journal of applied physics 68*(9), 4461–4473.

Bernstein, I. B. and I. N. Rabinowitz (1959). Theory of electrostatic probes in a low-density plasma. *The Physics of Fluids 2*(2), 112–121.

Bishara, W. and S. Banna (2014, December 18). Method for fast and repeatable plasma ignition and tuning in plasma chambers. US Patent App. 14/287,480.

Bletzinger, P. and M. J. Flemming (1987). Impedance characteristics of an rf parallel plate discharge and the validity of a simple circuit model. *Journal of applied physics 62*(12), 4688–4695.

Boffard, J. B., S. Wang, C. C. Lin, and A. Wendt (2015). Detection of fast electrons in pulsed argon inductively-coupled plasmas using the 420.1–419.8 nm emission line pair. *Plasma Sources Science and Technology 24*(6), 065005.

Bohm, D., E. H. S. Burhop, and H. Massey (1949). *The characteristics of electrical discharges in magnetic fields*, Volume 5. McGraw-Hill.

Booth, J., G. Cunge, N. Sadeghi, and R. Boswell (1997). The transition from symmetric to asymmetric discharges in pulsed 13.56 mhz capacitively coupled plasmas. *Journal of applied physics 82*(2), 552–560.

Boschi, A. and F. Magistrelli (1963). Effect of a rf, signal on the characteristic of a langmuir probe. *Il Nuovo Cimento (1955-1965) 29*(2), 487–499.

Brandt, S., B. Berger, E. Schüngel, I. Korolov, A. Derzsi, B. Bruneau, E. Johnson, T. Lafleur, D. O'Connell, M. Koepke, et al. (2016). Electron power absorption dynamics in capacitive radio frequency discharges driven by tailored voltage waveforms in cf4. *Plasma Sources Science and Technology 25*(4), 045015.

Bruneau, B., T. Lafleur, T. Gans, D. O'Connell, A. Greb, I. Korolov, A. Derzsi, Z. Donkó, S. Brandt, E. Schüngel, et al. (2015). Effect of gas properties on the dynamics of the electrical slope asymmetry effect in capacitive plasmas: comparison of ar, h2 and cf4. *Plasma Sources Science and Technology 25*(1), 01LT02.

Butterbaugh, J., L. Baston, and H. Sawin (1990). Measurement and analysis of radio frequency glow discharge electrical impedance and network power loss. *Journal of Vacuum Science & Technology A: Vacuum, Surfaces, and Films 8*(2), 916–923.

Chen, J.-Y., J. P. Holland, A. H. Sato, and V. N. Todorow (2002, October 29). Pulsed rf power delivery for plasma processing. US Patent 6,472,822.

Czarnetzki, U., J. Schulze, E. Schüngel, and Z. Donkó (2011, apr). The electrical asymmetry effect in capacitively coupled radio-frequency discharges. *Plasma Sources Science and Technology 20*(2), 024010.

David, P., M. Sicha, M. Tichy, T. Kopiczynski, and Z. Zakrzewski (1990). The use of langmuir probe methods for plasma diagnostic in middle pressure discharges. *Contributions to Plasma Physics 30*(2), 167–184.

Donkó, Z., J. Schulze, U. Czarnetzki, A. Derzsi, P. Hartmann, I. Korolov, and E. Schüngel (2012). Fundamental investigations of capacitive radio frequency plasmas: simulations and experiments. *Plasma Physics and Controlled Fusion 54*(12), 124003.

Economou, D. J. (2014). Pulsed plasma etching for semiconductor manufacturing. *Journal of Physics D: Applied Physics 47*(30), 303001.

Emeleus, K. and A. Garscadden (1962). Notes on plasma-electron oscillations. *Il Nuovo Cimento (1955-1965) 26*, 40–49.

Eser, E., R. Ogilvie, and K. Taylor (1978). Measurement of plasma discharge characteristics for sputtering applications. *Journal of Vacuum Science and Technology 15*(2), 199–202.

Gagné, R. and A. Cantin (1972). Investigation of an rf plasma with symmetrical and asymmetrical electrostatic probes. *Journal of Applied Physics 43*(6), 2639–2647.

Godyak, V. and R. Piejak (1990). In situ simultaneous radio frequency discharge power measurements. *Journal of Vacuum Science & Technology A: Vacuum, Surfaces, and Films 8*(5), 3833–3837.

Godyak, V., R. Piejak, and B. Alexandrovich (1992). Measurement of electron energy distribution in low-pressure rf discharges. *Plasma Sources Science and Technology 1*(1), 36.

Godyak, V. A., R. B. Piejak, and B. M. Alexandrovich (1991). Electrical characteristics of parallel-plate rf discharges in argon. *IEEE Transactions on plasma science 19*(4), 660–676.

Goeckner, M., J. Marquis, B. Markham, A. Jindal, E. Joseph, and B.-S. Zhou (2004). Modified gaseous electronics conference reference cell for the study of plasma-surface-gas interactions. *Review of scientific instruments 75*(4), 884–890.

Heil, B. G., U. Czarnetzki, R. P. Brinkmann, and T. Mussenbrock (2008). On the possibility of making a geometrically symmetric rf-ccp discharge electrically asymmetric. *Journal of Physics D: Applied Physics 41*(16), 165202.

Hopkins, M. (1995). Langmuir probe measurements in the gaseous electronics conference rf reference cell. *Journal of research of the National Institute of Standards and Technology 100*(4), 415.

Hwang, G. S. and K. P. Giapis (1998). Mechanism of charging reduction in pulsed plasma etching. *Japanese journal of applied physics 37*(4S), 2291.

Jiang, B., J. Zheng, S. Qiu, M. Wu, Q. Zhang, Z. Yan, and Q. Xue (2014). Review on electrical discharge plasma technology for wastewater remediation. *Chemical Engineering Journal 236*, 348–368.

Kanakasabapathy, S. K., L. J. Overzet, V. Midha, and D. Economou (2001). Alternating fluxes of positive and negative ions from an ion–ion plasma. *Applied Physics Letters 78*(1), 22–24.

Keller, J. H. and W. Pennebaker (1979). Electrical properties of rf sputtering systems. *IBM Journal of Research and Development 23*(1), 3–15.

Klick, M. (1996). Nonlinearity of the radio-frequency sheath. *Journal of applied physics 79*(7), 3445–3452.

Koenig, H. and L. Maissel (1970). Application of rf discharges to sputtering. *IBM Journal of research and development 14*(2), 168–171.

Köhler, K., J. Coburn, D. Horne, E. Kay, and J. Keller (1985). Plasma potentials of 13.56-mhz rf argon glow discharges in a planar system. *Journal of Applied Physics 57*(1), 59–66.

Kopiczynski, T. (1977). Ph. D. thesis, Institute of Fluid Flow Machines, Polish Academy of Sciences.

Kumar, N., J. H. Park, S. N. Jeon, B. S. Park, E. H. Choi, and P. Attri (2016). The action of microsecond-pulsed plasma-activated media on the inactivation of human lung cancer cells. *Journal of Physics D: Applied Physics 49*(11), 115401.

Laframboise, J. G. (1966). Theory of spherical and cylindrical langmuir probes in a collisionless, maxwellian plasma at rest. Technical report, Toronto University Downsview (Ontario) INST For Aerospace Studies.

Lee, C. G., K. J. Kanarik, and R. A. Gottscho (2014). The grand challenges of plasma etching: a manufacturing perspective. *Journal of Physics D: Applied Physics 47*(27), 273001.

Li, J., H. Guo, B. Wan, X. Gong, Y. Liang, G. Xu, K. Gan, J. Hu, H. Wang, L. Wang, et al. (2013). A long-pulse high-confinement plasma regime in the experimental advanced superconducting tokamak. *Nature physics 9*(12), 817.

Lieberman, M., A. Lichtenberg, E. Kawamura, T. Mussenbrock, and R. P. Brinkmann (2008). The effects of nonlinear series resonance on ohmic and stochastic heating in capacitive discharges. *Physics of Plasmas 15*(6), 063505.

Lieberman, M. A. and A. J. Lichtenberg (2005). *Principles of plasma discharges and materials processing.* John Wiley & Sons.

Liu, F.-X., Z.-B. Wang, and Y.-K. Pu (2014). The ac-coupling between a langmuir probe and a plasma and its effect on the plasma density measurement in the afterglow. *Journal of Physics D: Applied Physics 47*(7), 075201.

Malyshev, M., V. Donnelly, J. Colonell, and S. Samukawa (1999). Dynamics of pulsed-power chlorine plasmas. *Journal of applied physics 86*(9), 4813–4820.

Miranda, A. J. and C. J. Spanos (1996). Impedance modeling of a cl2/he plasma discharge for very large scale integrated circuit production monitoring. *Journal of Vacuum Science & Technology A: Vacuum, Surfaces, and Films 14*(3), 1888–1893.

Mishra, A., M. H. Jeon, K. N. Kim, and G. Y. Yeom (2012). An investigation of the temporal evolution of plasma potential in a 60 mhz/2 mhz pulsed dual-frequency capacitively coupled discharge. *Plasma Sources Science and Technology 21*(5), 055006.

Mott-Smith, H. M. and I. Langmuir (1926). The theory of collectors in gaseous discharges. *Physical Review 28*(4), 727.

Norström, H. (1979). Langmuir probe studies of the glow discharge in an rf sputtering system at various frequencies. *Vacuum 29*(11-12), 443–445.

Overzet, L. J., J. Beberman, and J. Verdeyen (1989). Enhancement of the negative ion flux to surfaces from radio-frequency processing discharges. *Journal of Applied Physics 66*(4), 1622–1631.

Overzet, L. J., D. Jung, M. Mandra, M. Goeckner, T. Dufour, R. Dussart, and P. Lefaucheux (2010). Rf impedance measurements of dc atmospheric micro-discharges. *The European Physical Journal D 60*(3), 449–454.

Overzet, L. J. and F. Y. Leong-Rousey (1995). Time-resolved power and impedance measurements of pulsed radiofrequency discharges. *Plasma Sources Science and Technology 4*(3), 432.

Overzet, L. J., B. A. Smith, J. Kleber, and S. K. Kanakasabapathy (1997). Negative ion extraction from pulsed discharges. *Japanese journal of applied physics 36*(4S), 2443.

Panagopoulos, T. and D. J. Economou (1999). Plasma sheath model and ion energy distribution for all radio frequencies. *Journal of applied physics 85*(7), 3435–3443.

Paranjpe, A. P., J. P. McVittie, and S. A. Self (1990). A tuned langmuir probe for measurements in rf glow discharges. *Journal of Applied Physics 67*(11), 6718–6727.

Polzin, K. A. (2011). Comprehensive review of planar pulsed inductive plasma thruster research and technology. *Journal of Propulsion and Power 27*(3), 513–531.

Poulose, J., M. Goeckner, S. Shannon, D. Coumou, and L. Overzet (2017). Driving frequency fluctuations in pulsed capacitively coupled plasmas. *The European Physical Journal D 71*(9), 242.

Press, A. F., M. J. Goeckner, and L. J. Overzet (2019). Sub-rf period electrical characterization of a pulsed capacitively coupled argon plasma. *Journal of Vacuum Science & Technology B, Nanotechnology and Microelectronics: Materials, Processing, Measurement, and Phenomena 37*(6), 062926.

Rauf, S. and M. J. Kushner (1998). The effect of radio frequency plasma processing reactor circuitry on plasma characteristics. *Journal of Applied Physics 83*(10), 5087–5094.

Rousseau, A., E. Teboul, and S. Béchu (2005). Comparison between langmuir probe and microwave autointerferometry measurements at intermediate pressure in an argon surface wave discharge. *Journal of applied physics 98*(8), 083306.

Schuengel, E., S. Mohr, J. Schulze, U. Czarnetzki, and M. J. Kushner (2013). Ion distribution functions at the electrodes of capacitively coupled high-pressure hydrogen discharges. *Plasma Sources Science and Technology 23*(1), 015001.

Schulze, J., B. Heil, D. Luggenhölscher, R. Brinkmann, and U. Czarnetzki (2008). Stochastic heating in asymmetric capacitively coupled rf discharges. *Journal of Physics D: Applied Physics 41*(19), 195212.

Schulze, J., E. Schüngel, and U. Czarnetzki (2009). The electrical asymmetry effect in capacitively coupled radio frequency discharges–measurements of dc self bias, ion energy and ion flux. *Journal of Physics D: Applied Physics 42*(9), 092005.

Sobolewski, M. A. (1992). Electrical characterization of radio-frequency discharges in the gaseous electronics conference reference cell. *Journal of Vacuum Science & Technology A: Vacuum, Surfaces, and Films 10*(6), 3550–3562.

Sobolewski, M. A. (1995). Electrical characteristics of argon radio frequency glow discharges in an asymmetric cell. *IEEE Transactions on Plasma Science 23*(6), 1006–1022.

Subramonium, P. and M. J. Kushner (2002). Two-dimensional modeling of long-term transients in inductively coupled plasmas using moderate computational parallelism. i. ar pulsed plasmas. *Journal of Vacuum Science & Technology A: Vacuum, Surfaces, and Films 20*(2), 313–324.

Sudit, I. D. and F. F. Chen (1994). Rf compensated probes for high-density discharges. *Plasma Sources Science and Technology 3*(2), 162.

Verdeyen, J. T. (1992). Measurements and analysis of the equivalent circuit of the gec rf reference cell.[gec (gaseous electronics conference); rf (radio-frequency)]. Technical report, Sandia National Labs., Albuquerque, NM (United States); Illinois Univ., Urbana, IL (United States). Dept. of Electrical and Computer Engineering.

Xue, C., D.-Q. Wen, W. Liu, Y.-R. Zhang, F. Gao, and Y.-N. Wang (2017). Experimental and numerical investigations on time-resolved characteristics of pulsed inductively coupled o2/ar plasmas. *Journal of Vacuum Science & Technology A: Vacuum, Surfaces, and Films 35*(2), 021301.

Zakrzewski, Z. and T. Kopiczynski (1974). Effect of collisions on positive ion collection by a cylindrical langmuir probe. *Plasma Physics 16*(12), 1195.

BIOGRAPHICAL SKETCH

After high school, Alex Press joined the United States Navy as an aviation electrician's mate. After four years in the navy, Alex attended Tidewater Community College before transferring to the University of Illinois, where in 2014 he earned a Bachelor of Science in Physics. During his time at the University of Illinois, Alex worked as an undergraduate researcher at the Center for Plasma-Material Interactions. His efforts there culminated in him being named the University of Illinois student worker of the year for 2014. At the start of 2015, Alex joined the Center for Advanced Materials Processing at The University of Texas at Dallas, where he worked as a graduate research assistant until December of 2019. During this period he earned both a Master of Science in Electrical Engineering in August of 2017, and a Doctor of Philosophy in May of 2020 from The University of Texas at Dallas.

CURRICULUM VITAE

Alex F. Press

Contact Information:

Department of Electrical Engineering
The University of Texas at Dallas
800 W. Campbell Rd.
Richardson, TX 75080-3021, U.S.A.

Email: `axp151230@utdallas.edu`

Educational History:

BS, Physics, University of Illinois, 2014
MS, Electrical Engineering, The University of Texas at Dallas, 2017
PhD, Electrical Engineering, The University of Texas at Dallas, 2020

Electrical Measurements of Capacitively Coupled Pulsed Power Plasmas
PhD Dissertation
Department of Electrical and Computer Engineering, The University of Texas at Dallas
Advisors: Dr. Lawrence Overzet and Dr. Matthew Goeckner

A Method to use a Cylindrical Langmuir Probe in Pulsed Plasma
MS Thesis
Department of Electrical and Computer Engineering, The University of Texas at Dallas
Advisors: Dr. Lawrence Overzet and Dr. Matthew Goeckner

Laboratory Experience:

Graduate Research Assistant, The University of Texas at Dallas, Center for Advanced Materials Processing, 2015-2019
Summer Intern, Lam Research, 2016
Undergraduate Research, University of Illinois, Center for Plasma-Material Interactions, 2012-2014

Professional Recognitions and Honors:

Student Employee of the Year, University of Illinois, 2014
Yellow Ribbon Scholarship, 2012
Give ‘em Hell Hero, Aviation Intermediate Maintenance Department, USS Harry S. Truman, 2008

Professional Memberships:

American Vacuum Society (AVS), 2015–present
American Physical Society (APS), 2019–present

Publications:

Press, A. F., Goeckner, M. J., & Overzet, L. J. (2019). Sub-rf period electrical characterization of a pulsed capacitively coupled argon plasma. *Journal of Vacuum Science & Technology B, Nanotechnology and Microelectronics: Materials, Processing, Measurement, and Phenomena*, 37(6), 062926.

Fiflis, P., Press, A., Xu, W., Andruczyk, D., Curreli, D., & Ruzic, D. N. (2014). Wetting properties of liquid lithium on select fusion relevant surfaces. *Fusion Engineering and Design*, 89(12), 2827-2832.